University of Southampton

Faculty of Physical Sciences and Engineering

Optoelectronics Research Centre

Nanomechanics with electron beam: detection and control of motion

by

Toji Thomas

ORCID ID 0009-0009-6849-280X

Thesis for the degree of Doctor of Philosophy

January 2026

University of Southampton

Abstract

Faculty of Engineering and Physical Sciences

Optoelectronics Research Centre

Doctor of Philosophy

Nanomechanics with electron beam: detection and control of motion

by

Toji Thomas

The study of nanomechanics using an electron beam has developed into an area of research, with recent works reporting on Brownian and ballistic motion detection[1, 2], dynamic backaction[3, 4],visualisation of sub-nm motion[5] and mass sensing[6]. It is important because the electron beam offers a platform for real-time observations of dynamics exhibited by nano- and microscale objects, with sub-nm scale displacement sensitivity and MHz bandwidth, as well as for controlling and characterising mechanical properties. In this study, I report the following yet unexplored aspects:

- I have introduced a new technique for detecting and mapping the periodic motion of nano/microscale objects via cathodoluminescence, with nanometric displacement sensitivity and spatial resolution, and MHz bandwidth implemented in a modified scanning electron microscope. Its capability is demonstrated by detecting and mapping driven motion of nanomechanical cantilevers. The technique offers a noise equivalent displacement amplitude spectral density of 1 nm/$\sqrt{\text{Hz}}$.

- I have observed the phenomenon of dependence of the frequency of oscillation of a cantilever on the presence of the electron beam. The repulsion between an electron beam and charge accumulated on a nanomechanical cantilever yields a stiffening that increases its resonance frequency, providing a mechanism for controlling resonators and sensing charge. For a cantilever of microscale length and nanoscale cross-section interacting with an electron beam, I observe a resonance shift on the order of 5% per nanocoulomb. The resonance frequency was expressed as a function of induced charge and electron beam parameters such as position, beam current and acceleration voltage. The model was tested experimentally by varying the current of an electron beam and its distance from the edge of grounded and isolated cantilevers.

- Driving oscillations of a nanomechanical beam can lead to a bistable response related to the nonlinearity of the mechanical restoring force. I have observed for the first time that the nonlinear response of a nanowire and the regime of bistability can be controlled by the electron beam impinging on the oscillator. A nanowire that is fixed at both ends and driven to the nonlinear regime of bistable resonant oscillation was switched between its bistable states by changing the distance between a 10 kV, 1.3 nA electron beam and the nanowire. The control mechanism has been explained as a consequence of electron-beam-induced heating, leading to thermal expansion that affects stress in the nanowire, which controls its resonance frequency. Therefore, the electron beam can shift the nanowire's bistable resonance relative to a fixed frequency of driven oscillation, enabling it to switch between the bistable states.

In summary this thesis reports on new ways for characterizing motion and controlling dynamics of nano- and microscale systems with electron beams.

Table of Contents

Table of Contents **4**

Table of Tables **7**

Table of Figures **8**

List of Accompanying Materials **11**

Research Thesis: Declaration of Authorship **12**

Acknowledgements **13**

Definitions and Abbreviations **15**

Chapter 1 Introduction **17**

1.1 Nanomechanics **18**

1.1.1 Nanomechanical structures in technology and science. 19

1.1.1.1 Nanomechanical sensors 19

1.1.1.2 Nanomechanical metamaterials 21

1.2 Nanomechanical motion detection techniques **24**

1.2.1 Secondary electron signals for nanomechanical motion detection 27

1.3 Thesis outlook **29**

Chapter 2 Background and establishing methodology **31**

2.1 Mechanical eigenfrequencies of nanomechanical structures **31**

2.2 Dynamics of nanomechanical structures **35**

2.2.1 Forced oscillator dynamics 36

2.3 Electron as a probe **40**

2.3.1 Electron beam-sample interaction 40

2.4 Electromagnetic field of an electron moving in a vacuum **43**

2.5 Cathodoluminescence **44**

2.5.1 Coherent and incoherent cathodoluminescence 45

2.6 Noise equivalent displacement at unitary SNR **48**

2.7 CL emission probability as a function of electron beam position and electron beam diameter **51**

2.8 Numerical simulations of cathodoluminescence 53

2.9 Cathodoluminescence measurements on gold nanostructures 58

2.10 Choosing the cathodoluminescence material 64

2.10.1 Brighter material deposition 68

2.11 Summary 69

Chapter 3 Nanomechanical motion detection and visualisation through cathodoluminescence 71

3.1 Experimental schematics for nanomechanical motion detection and imaging using CL 72

3.2 Detecting nanomechanical motion using cathodoluminescence 73

3.2.1 Mechanical displacement amplitude and quality factor 75

3.3 Nanomechanical motion imaging using cathodoluminescence 76

3.3.1 Calibrating cantilever displacement to driving voltages 76

3.3.2 Mode mapping of driven motion using cathodoluminescence 78

3.4 Possibility of detecting thermal motion 81

3.5 Summary 82

Chapter 4 Electrostatic control of nanomechanical resonances by an electron beam 83

4.1 Experiment 84

4.2 Analytical model 87

4.3 Evaluating the charge on a cantilever 90

4.4 The effect of electron beam current on a cantilever's resonance 91

4.5 Summary 93

Chapter 5 Electron-beam-controlled volatile nanomechanical bistability 94

5.1 Non-linearity and bistabilty in a nanowire 96

5.2 Observation of bistability using an electron beam 98

5.3 Effect of the electron beam on the bistable resonance 100

5.4 Electron-beam-controlled switching between bistable states 103

5.5 Summary 108

Chapter 6 Conclusion 109

6.1 Summary 109

6.2 Outlook 110

Appendix A Experimental Setup 113

Appendix B Publications 114

Bibliography 115

Table of Tables

Table 2.1: ***Values of the mode-dependent parameter Λn for cantilever and bridge*** 33

Table 2.2: ***Quantifying the signal-to-noise ratio for nanomechanics*** 67

*Table 5.1****: Materials used for making the nanomechanical resonators and their mechanical and thermal properties.*** 102

Table of Figures

Figure 1.1: ***Examples of nanomechanical sensors***. 21

Figure 1.2: ***Reconfigurable nanomechanical photonic metamaterials.*** 23

Figure 1.3: ***Selected existing nanomechanical motion detection and imaging techniques***.. 26

Figure 1.4: ***Thermomechanical motion visualisation of a cantilever using secondary electron signal.*** 28

Figure 2.1: ***Simulated mode shapes and corresponding in-plane eigen frequencies of a stress-free silicon nitride nanoresonator with length*** *L* = 25 µm***, thickness*** *h* = 50 nm***, and width*** *W* = 200 nm**.** 34

Figure 2.2: ***Fundamental in-plane resonance frequency as a function of stress of a silicon nitride nanowire***. 35

Figure 2.3: ***Mechanical motion amplitude*** *(a)* ***and phase*** *(b)* ***of mechanical oscillators as a function of driving frequency for different dissipation factors*** *(γm)*. 38

Figure 2.4: ***Difference between an optical probe and an electron probe.*** 40

Figure 2.5: ***Electron beam-specimen interaction***. 41

Figure 2.6: ***Evanescent character of the electromagnetic field produced by a fast electron***. 44

Figure 2.7: ***Coherent and incoherent CL emission patterns for a normal incidence of an electron beam***. 46

*Figure 2.8****: Expected photon yield as a function of electron beam impact position near the edge of a metallic structure kept in a vacuum.*** 48

*Figure 2.9****: Illustration of the concept of detecting nanomotion by the detection of electron-induced photon emission.*** 49

Figure 2.10: ***Electron beam near an arbitrary edge***. 51

*Figure 2.11****: CL emission probability per electron as a function of impact position.*** 54

Figure 2.12: ***CL photon emission probability per electron as a function of impact position for different electron beam diameters*** 55

Figure 2.13: ***Estimating noise equivalent displacement.*** 56

*Figure 2.14**: Noise equivalent displacement at unitary SNR for different acceleration voltages.*** 57

Figure 2.15: ***Illustration of the initial experimental setup.*** 58

Figure 2.16: ***CL emission spectrum from a flat gold surface for an incident*** 10 kV,18 nA ***electron beam***. 59

Figure 2.17: ***CL emission yield during line scan across a gold edge***. 61

Figure 2.18: ***Experimental results for estimating the noise equivalent displacement at unitary SNR.*** 63

Figure 2.19: ***CL emission spectra of Au in comparison with brighter materials.*** 66

Figure 2.20: ***Total CL photon emission rate from different material combinations.*** 69

Figure 3.1: ***Schematics for nanomotion visualisation using cathodoluminescence.*** 72

Figure 3.2: ***Nanomechanical motion detection using cathodoluminescence***. 74

Figure 3.3: ***Mechanical displacement amplitude and quality factor***. 75

Figure 3.4: ***Calibration curve for displacement as a function of driving voltage***. 78

Figure 3.5: ***Mechanical mode mapping using cathodoluminescence.*** 79

Figure 3.6: ***Detecting sub-nm motion:*** 82

Figure 4.1: ***Illustration of the concept of charging affecting a nanomechanical resonance***. 84

*Figure 4.2**: Mechanical resonances detected at different electron beam injection points for isolated and grounded cantilevers.*** 86

Figure 4.3: ***A simple model for understand how electron-beam-induced charging affects nanomechanics***. 88

Figure 4.4: ***Relative frequency shift and charge estimation.*** 91

Figure 4.5: ***Beam current dependence of the resonance of an isolated cantilever simultaneously observed using the SE and CL signal.*** 92

Figure 5.1: ***A free-standing nanowire is driven to its bistable regime of in-plane mechanical oscillation***. 95

Figure 5.2: ***Schematic illustration of a displaced double clamped beam***. 96

Figure 5.3: ***The nanowire and its transition from linear to non-linear oscillation.*** 99

Figure 5.4: ***Effect of the electron beam position on the nanowire's bistable resonance***. ... 102

Figure 5.5: ***Experimental procedure to detect and characterize the bistability response.*** . 104

Figure 5.6: ***Switching between bistable states using an electron beam***. 105

Figure 5.7: ***Mechanism of electron beam control of nanomechanical bistability***. 106

Figure 5.8: ***Effect of the electron beam currant on the nanowire's bistable resonance***. 108

List of Accompanying Materials

The research data presented in this thesis can be found as:

Dataset for “Electrostatic control of nanomechanical resonances by an electron beam”:

DOI https://doi.org/10.5258/SOTON/D3698

Dataset for “Electron-beam-controlled volatile nanomechanical bistability”:

DOI https://doi.org/10.5258/SOTON/D3701

Research Thesis: Declaration of Authorship

Print name: Toji Thomas

Title of thesis: Nanomechanics with electron beam: detection and control of motion

I declare that this thesis and the work presented in it are my own and has been generated by me as the result of my own original research.

I confirm that:

1. This work was done wholly or mainly while in candidature for a research degree at this University;
2. Where any part of this thesis has previously been submitted for a degree or any other qualification at this University or any other institution, this has been clearly stated;
3. Where I have consulted the published work of others, this is always clearly attributed;
4. Where I have quoted from the work of others, the source is always given. With the exception of such quotations, this thesis is entirely my own work;
5. I have acknowledged all main sources of help;
6. Where the thesis is based on work done by myself jointly with others, I have made clear exactly what was done by others and what I have contributed myself;
7. Parts of this work have been published as ArXiv papers and conference contributions listed in Appendix B.

Signature: ..... Date: 13/01/2026

Acknowledgements

I express my sincere gratitude for allowing me to work in the Nanophotonic and Metamaterials group led by Prof. Nikolay I. Zheludev at the Optoelectronics Research Centre, University of Southampton. I acknowledge all the support and guidance from my supervisors, Dr. Eric Plum, Prof. Kevin F. MacDonald, and Prof. Nikolay I. Zheludev. Dr. Eric Plum has constantly guided me and provided me with unique and logical insights on approaching the experimental and analytical problems. I can't thank him enough for his patience and support during my PhD. Prof. Kevin F. MacDonald consistently asked insightful questions and offered valuable guidance that helped me steer through my projects. I thank Prof. Nikolay I. Zheludev, a person with vast and extraordinary knowledge and experience in physics, for his inputs and guidance on my project.

I thank Dr. Jun-Yu (Bruce) Ou for teaching me how to operate the Scanning Electron Microscope and arranging periodic beer meetings to ease my mind from the research tensions. To Prof. Austin Taranta, for offering me a research assistant position in Hollow Core Fibre group post my PhD funding period. I want to thank the SEM engineers, Torquil Wells and Roger Hamblin, for their timely services and instructions on maintaining the SEM. I am grateful to Dr. Oleksandr Buchnev for the focused ion beam milling machine training, Neil Session for training on clean room facilities, Jonathan Kerly and Mike Bartlett for their help with collecting liquid nitrogen and other technical help. I thank Sue Nash, Davina Macnally, Samantha Howlett, Keri Jenkins, and Lola Jerrard for their help in booking tickets, accommodations and arranging documents for conferences.

I would like to thank all the people of the Nanophotonics and Metamaterials group for their help during my studies. Words will not describe how grateful I am to my friends in the Optoelectronics Research Centre and Physics especially, Luka Vignjevic, Eleanor Osborne, Robin Elliott, Rosemary Clark, Henry Thompson, Ben Stedman, Elizaveta Elistratova, Baurzhan Salimzhan, Venugopal Raskatla, Dr. Tanchao Pu, Abhishek Vijayakumar, Kalen Barnfather, Dr. Nicholas Klokkou, Jack Homans, Thomas Grant and George Ong. They all made this four-year journey more memorable by regularly arranging sports events and other fun activities. I thank all the members of OPSoc committee where I had a privilege to be an Ethnicity, Diversity and Inclusion representative. I thank my friends outside ORC, Sepehr Nem, Edmar Alino, Mark James Fisher, Dr. Fabien Hannauer and Ola Kulesza. I thank the members of the Killick sailing club especially Dr. Colin Mitchell for teaching me how to sail. Some people are worth special mentioning, especially Dr. Resmi Ravi Kumar, her husband Dr. Tamilarasan Sabapathi, their daughter Ila, Dr. Sergei Kurdiumov, Dr. Aneesh Vincent Veluthandath, and Dr. Rhea Sam for their support and affection for me like a family. I would like to mention "1413 km" and "75p", two numbers from

two different incidence of my PhD journey that will remain with me as a constant reminder on how much this PhD is worth to me.

To my papa K. T. Thomas and my Mama Molly Thomas, I cannot thank you enough for raising me with values and supporting me throughout my life. I am grateful to my brothers, Tony Thomas and Alex Thomas, for supporting and looking after the family when I am away. To Akhil Paul, my friend, thank you for investing in me. To Catherine, dear, dearest, I owe you a lot for your love, tolerance, and constant encouragement in times of depression, and for pushing me to move forward. Above all, to God, whom I pray for peace, strength, wisdom, and knowledge I thank you.

Definitions and Abbreviations

AE ..... Auger Electrons

AFM ..... Atomic Force Microscope

BEM ..... Boundary Element Method

BSE ..... Back Scattered Electrons

CL ..... Cathodoluminescence

CNT ..... Carbon Nano Tube

CR ..... Cherenkov Radiation

DAQ ..... Data Acquisition Module

DNA ..... Deoxyribonucleic Acid

EDX ..... Energy-Dispersive X-ray

EELS ..... Electron Energy Loss Spectrum

EM ..... Electromagnetic

FEM ..... Finite Element Method

FIB ..... Focused Ion Beam

FWHM ..... Full Width Half Maximum

HCF ..... Hollow Core Fiber

HMV ..... Hyperspectral Motion Visualisation

LDOS ..... Local Density of Optical States

LDV ..... Laser Doppler Vibrometry

MEMS ..... Microelectromechanical System

MLG ..... Multi-Layer Graphene

MNPBEM ..... Metallic Nanoparticle Boundary Element Method

MOCVD ..... Metal-Organic Chemical Vapour Deposition

NED ..... Noise Equivalent Displacement

NEMS ..... Nanoelectromechanical System

NV ..... Nitrogen Vacancy

RGT ..... Resonant Gate Transistor

SE ..... Secondary Electron

SEM ..... Scanning Electron Microscope

SCCM ..... Standard Cubic Centimetres per Minute

SMF ..... Single Mode Fiber

SNR ..... Signal-to-Noise Ratio

SPM ..... Scanning Probe Microscopy

SPP ..... Surface plasmon Polariton

STM ..... Scanning Tunnelling Microscope

TCSPC ..... Time-Correlated Single Photon Counting

TEM ..... Transmission Electron Microscope

TR ..... Transition Radiation

UHFLI ..... Ultra-High-Frequency dual channel Lock-In amplifier

UTEM ..... Ultrafast Transmission Electron Microscopy

WDX ..... Wavelength-Dispersive X-ray

Chapter 1 Introduction

Anything that moves piques human curiosity. Such movements can be faster, slower, visible, or invisible to our naked eyes. Planetary motion, cosmological events[7], chemical reaction processes[8], atomic and molecular motion[9], electron transport[10], molecular vibration, rotational motion[11], phonon transport in crystals and 2D materials[12], protein folding[13], osmosis[14], radiative recombination[15], etc, are a few among them. Observing, questioning, understanding, and sometimes replicating such events are crucial for technological and scientific progress.

When it comes to the research community, a special interest is shown for the dynamics of nanomechanical structures/systems, as they find application across different scientific disciplines[16]. The constant improvement in nanofabrication techniques has helped in building small-sized artificial structures such as nanotubes[17], nanoparticles[18], thin-film membranes [19], micro- and nanomechanical structures (nanowires, cantilevers, double clamped bridges, etc.) that can serve as components of micro-and nanoelectromechanical systems (MEMS and NEMS)[20-23]. These developments had a significant influence on the growth of research fields such as plasmonics[24], nano-optomechanics[25], metamaterials[26], and the recent field of photonic metamaterial time crystals[27].

In comparison to larger structures, nanomechanical structures have low mass (pg or less) and exhibit faster thermomechanical movements (kHz-GHz range) with nm to sub-nm motion amplitude at room temperature[26]. Having a small mass implies such structures can respond quickly to external stimuli, which could perturb their natural dynamics. This has been exploited for designing sensors for detecting mass, pressure, temperature, charge, and force. At the same time, detecting such fast dynamics implies that events happening at correspondingly small-time scales can also be visualised.

Nanomechanical systems can be externally driven to achieve nano-picometer scale displacements with the help of piezoelectric driving, acoustic driving, capacitive actuation, optical excitation, electromagnetic influence, thermal force, etc[28-30]. The mechanical behaviour of such a driven systems (including thermomechanical systems) can then be tuned or controlled by a light or electron beam probe.

Functionalities of nanomechanical systems are underpinned by their fast mechanical motion. Therefore, understanding the driven and thermo-mechanical oscillations of such systems is vital.

Many techniques are used in detecting and imaging such motions, but each has its advantages and disadvantages. Recently, a hyperspectral imaging metrology was introduced[5], which utilises the secondary electron gradient in the displacement direction of a nanostructure and the nanometric spatial resolution of a scanning electron microscope (SEM) to visualise and understand such nanomechanical motions with picometre displacement resolution.

Using electron-induced secondary emissions for nanomechanical motion studies raised a few questions. Can other electron-induced emissions, such as light in the form of cathodoluminescence (CL), be used for nanomotion visualisation? How charging and heating by the electron beam influence nanomechanics, and how can such effects be utilised rather than avoiding them. The objective of this thesis is to address these questions.

1.1 Nanomechanics

The possibilities and potentials of constructing machines and devices by arranging atoms one by one were one of the thought-provoking topics put forward by Richard Feynman when he gave his famous 1959 lecture, "*There is plenty of room at the bottom*"[31]. His lecture later inspired the field of 'nanotechnology'. The term 'nanotechnology' was first used by Norio Taniguchi in his 1974 paper[32] as a term for the process of separating, consolidating, and deforming materials at the atomic or molecular level. The name got public attention through K. Eric Drexler's book *'Engines of Creation: The Coming Era of Nanotechnology*' in 1986[33]. Microelectromechanical systems (MEMS) gained popularity in the 1960s-1980s with the invention of the resonant gate transistor (RGT)[34] and later with the advancement of silicon microfabrication, which led to the development of integrated MEMS devices, such as pressure sensors, accelerometers, and micromechanical resonators[35]. The era of atomic-scale manipulation started with the invention of the scanning tunnelling microscope (STM) in 1981[36]. It made the visualisation of atoms and bonds possible. The discovery was awarded the Nobel Prize in Physics in 1986. The STM was followed by the invention of the atomic force microscope (AFM) in 1989[37]. AFMs use a flexible cantilever with a sharp probe that deflects under the forces between the tip of the probe and the surface atoms. The probe can respond to extremely small forces of about 10^{-18} N. Combining it with STM setup it enabled surface profiling with 3 nm lateral resolution and 0.1 nm vertical resolution[37]. This formed the foundation to nanomechanics.

In 1991, carbon nanotubes (CNTs) were discovered[38], which was inspired by the C_{60} or Buckminsterfullerene discovered in 1985[39]. The CNTs are of 2 to 30 nm in diameter and up to 1 μm in length. They are considered to be the first nanomechanical structure. By 1996 fabrication of silicon nanocantilevers and resonators gained momentum due to the advancements in top-down lithography[40]. They had dimensions below 100 nm with MHz-GHz resonance frequencies.

By combining nanomechanical structures with electronics for sensing, signal processing and biological detection, the early 2000s marked the bloom of nanoelectromechanical systems (NEMS).

1.1.1 Nanomechanical structures in technology and science.

As the physical dimension of objects decrease, the influence of electromagnetic, thermal, optical and quantum fluctuation forces become stronger and they can compete with the elastic force of the nanomechanical structures[26]. The small size improves sensitivity as minute interactions can translate into noticeable changes in mechanical responses such as change in resonance frequency, amplitude of motion or bending[41, 42].

1.1.1.1 Nanomechanical sensors

The fundamental mechanical resonance frequency of a resonator is given by, $f_o = \frac{1}{2\pi}\sqrt{k/m_{eff}}$, where k is the spring constant and m_{eff} is the effective mass (explained in Chapter 2). This tells that if mass increases the resonance frequency will shift (Δf) and the change in mass (Δm_{eff}) is then, $\Delta m_{eff} = -2m_{eff}\Delta f/f_o$ if the relative mass change is small. This implies that the resonance frequency decreases for mass added to the resonator (most common geometries are cantilever or bridge beam). This concept has been adopted to make nanomechanical mass sensors. Mass sensing with zepto-yoctogram scale ($10^{-21} - 10^{-24}$ g) is reported in [6, 43] (Figure1.1a). With additional features such as an adsorbent layer or use of multiple mechanical oscillation modes, nanomechanical resonators find huge applications for real-time and label-free detection of biomolecules, chemicals, pathogens, antigens, DNA, monitoring growth process of molecules in chemistry, biology and nanotechnology[44].

Pressure sensors mostly involve suspended nanomechanical structures (e.g. membranes) that will deflect under different pressure. This change in pressure makes the membrane stretch or compress and this changes the tension and results in resonance frequency shift. A nano-optomechanical gold-graphene-based pressure sensor is reported in [45]. The authors attach a suspend reflective gold-graphene membrane to one end of a hollow-core fiber (HCF) with the other end of the HCF acting acts as another mirror forming a Fabry-Perot cavity. Based on the pressure difference inside and outside the cavity the membrane tension changes and using an optomechanical readout, the shift in resonance frequency is detected (Figure 1.1c). This sensor claims to detect pressure differences of $\sim 1 \times 10^{-7}$mbar across a wide range of pressure (7×10^{-6} mbar $- 1000$ mbar). The pressure sensitivity reported was up to 1.38×10^{6} kHz/mbar.

Thermal expansion or contraction in response to temperature change will alter the stress and stiffness of nanomechanical structures. This in turn affects their resonance frequencies[46].

Resonance frequency as a function of stress for ideal double clamped bridges with rectangular geometry is discussed in Chapter 2. The smallest detectable temperature variation is limited depending on the detection instrument and measurement noise. A room temperature silicon nitride membrane resonator with 15 μK thermometry resolution is reported in [47] (Figure 1.1b). Temperature sensors find applications in health monitoring based on temperature variations of wearable devices, improving performance and longevity of electronic device (e.g. mobile phones, laptops etc.) by thermal monitoring, energy harvesting, studying heat transport in nanoscale materials etc.

The electrostatic force exerted by charges near a nanomechanical resonator can affect its mechanical resonance frequency and quality factor. These are often due to capacitive coupling. In[48], a charge-detecting nanomechanical resonator that can detect changes in charge down to a single electron is presented. The authors use a gold-silicon beam (width 80 nm and varying length) suspended between two gate contacts. The gate contacts couple capacitively with the resonator. The resonator is actuated into a nonlinear regime by passing a radiofrequency (RF) current through the gates in the presence of an in-plane static magnetic field. By varying the electrostatic potential of another nearby gate electrode, a change in resonator hysteresis response is detected. The charge sensitivity reported was about $0.1e/\sqrt{\text{Hz}}$ which is equivalent to $1e/\sqrt{100\ \text{Hz}}$.

The capability of a nanomechanical resonator for detecting electric potential is demonstrated in[49] using an optically levitated dielectric nanosphere suspended inside a vacuum cell. The nanosphere is charged using UV/photoemission or corona discharge. Having a net charge q, an applied external electric field (E_{ext}) exerts a force ($F = qE_{ext}$) on the particle and it caused measurable shifts in its mechanical response and position. These tiny fluctuations are detected using forward or back scattered light. The detection sensitivity of around 800 $\mu\text{V}/\sqrt{\text{Hz}}$ was reported. Similarly, nanomechanical resonator mechanics can change in response to magnetic field (B) through Lorentz force ($F = I.L \times B$) if the resonator is carrying any electrical current (I). It can also be due to magneto strictive effect that will change the stiffness of the resonator by magnetically-induced deformation[50] (Figure 1.1d).

An ultrasensitive force sensor with force sensitivity at the $40 \times 10^{-21}\text{N}/\sqrt{\text{Hz}}$ is presented in[51]. It consists of a suspended silicon carbide nanowire acting as a mechanical probe and optical readout is performed at extremely low temperatures (down to 32 ± 2 mK). Low temperature reduces thermal noise and mechanical damping. This enhances the force sensitivity. The change in local magnetic or electric fields, or temperature affect the sensor tip. The optomechanical readout quantifies these feeble forces. Such ultra-low force detection finds application in

fundamental physics at very low temperatures like single quantum spin detection and quantum vacuum fluctuations.

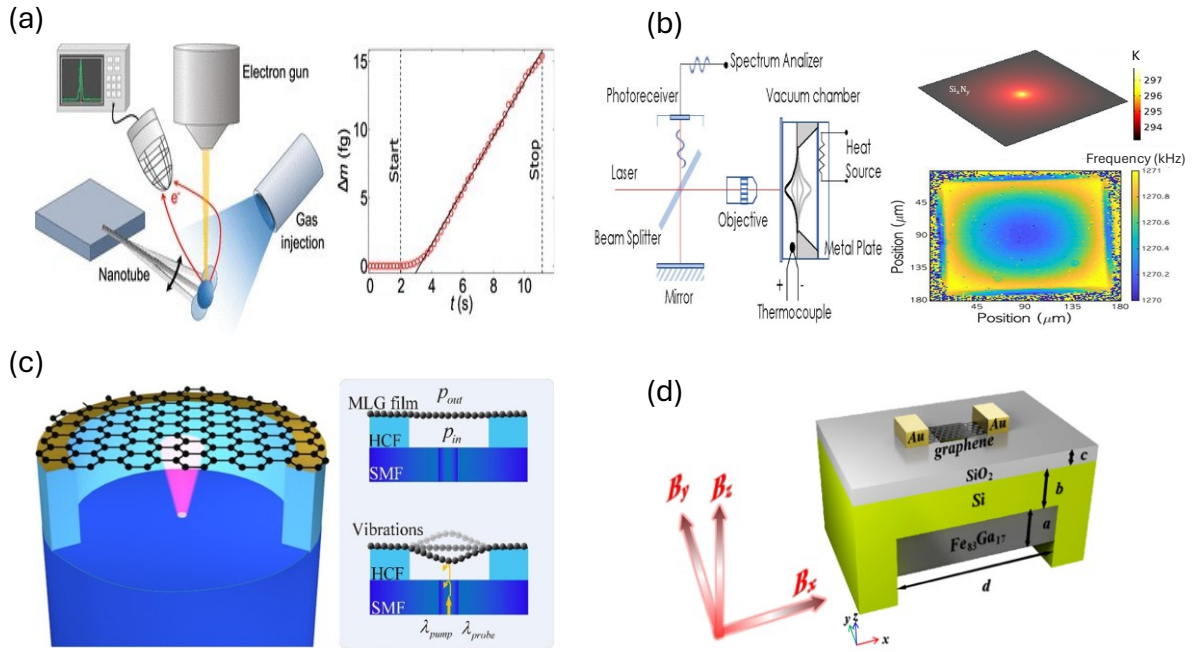

Figure 1.1: ***Examples of nanomechanical sensors****.(a) Schematics of a mass sensor: A gas injection system sprays the precursor gas, and a focused electron beam induces deposition of nanoparticles on a carbon nanotube. The variations in secondary electron signals are monitored using a spectrum analyser over the deposition period and the observed frequency shift is corelated to the deposited mass[6]. (b) Schematics of a temperature sensor; The thermoelastic effect shifts the mechanical resonance of a silicon nitride membrane which is mapped at different points along the membrane using the optical readout system[47]. (c) Illustration of a pressure sensor; The multilayer graphene (MLG)/gold membrane and the single mode fiber (SMF) end facet separated by a hollow core fiber (HCF) forms a Fabry-Perot cavity. Therefore, the pressure difference between the outside (P_{out}) and the inside (P_{in}) of the cavity affects the tension of the membrane and hence modify the resonance frequency. The variation is studied using optical pump and probe method [45]. (d) Schematics of a magnetic sensor chip: A doubly clamped graphene beam was suspended on the surface of a cavity. The magnetostrictive effect of $Fe_{83}Ga_{17}$ to an applied magnetic field (B_x, B_y, B_z) deforms the substrate, causing the two constrained edges of the graphene to generate tensile stresses in opposite directions. This changes the resonance frequency of the graphene beam. The change in frequency can be detected and correlated to the applied magnetic field[50].*

1.1.1.2 Nanomechanical metamaterials

Photonic metamaterials are artificially engineered electromagnetic media that are structured on the sub-wavelength scale whose properties arise from the design of their metaatoms or metamolecules[52]. Some of them rely on resonance excitations such as localised plasmonic modes for engineering the electromagnetic response. With the precise arrangements of

metamolecules, the effective electromagnetic properties of such metamaterial or metasurfaces can be controlled. Having a control over the effective electric permittivity, effective magnetic permeability, wavefront shaping of both reflected and transmitted light in terms of amplitude, phase, polarisation, wavevector and total angular momentum, metamaterials started to be used as miniaturised optical and photonic devices[53, 54].

Independently controlling individual metamolecules spatially and temporally at any instant opens ups possibilities such as phase and intensity modulation of light, active wavefront control, controlling near field electromagnetic radiation etc[26]. Spatially reconfigurable nanomembrane metamaterial addresses this challenge by taking advantage of the changing balance of forces at nanoscale to rearrange metamolecules supported by a flexible structure such as a membrane. Spatially reconfigurable nanomembrane metamaterials will respond to electromagnetic forces (Ampere, Lorentz, and Coulomb) (Figure 1.2a and b), optical signals and thermal stimulation to dynamically alter their optical properties[26]. For example, when the electromagnetic forces compete with the elastic forces this can alter the mutual arrangements of metamolecules or change the shape of individual metamolecules which will affect the optical properties. Photonic devices made of reconfigurable metamaterials achieve giant thermal (Figure 1.2c)-/electro-/magneto-/acousto-optical[55-60], phase change[61], electro-chiral[58] (Figure 1.2h) and nonlinear optical responses[62]. Devices and applications that have been demonstrated on this basis include dynamic wave plate[63] (Figure 1.2f), dynamic colour filtering and displays[64] (Figure 1.2e) and dynamic beam focusing[65, 66] (Figure 1.2d) etc.

When a system (an ensemble of nanowire oscillators alternatingly decorated with dissimilar plasmonic nanoparticles) is kept in the presence of an electromagnetic field, nonreciprocal interaction forces can emerge between dissimilar objects. This happens due to the difference in the radiation pressure induced by fields incident on and scattered from the dissimilar plasmonic nanoparticles on each other[67, 68]. When such systems interact with light intensity above a certain threshold level, a spontaneous transition in the nanowire ensemble is observed. It changes from a state of unsynchronised stochastic thermal motion (demobilised state) to a synchronised, high amplitude periodic oscillation (mobilised state). This is reported as a photonic metamaterial analogue of a continuous time-crystal [27] (Figure 1.2g).

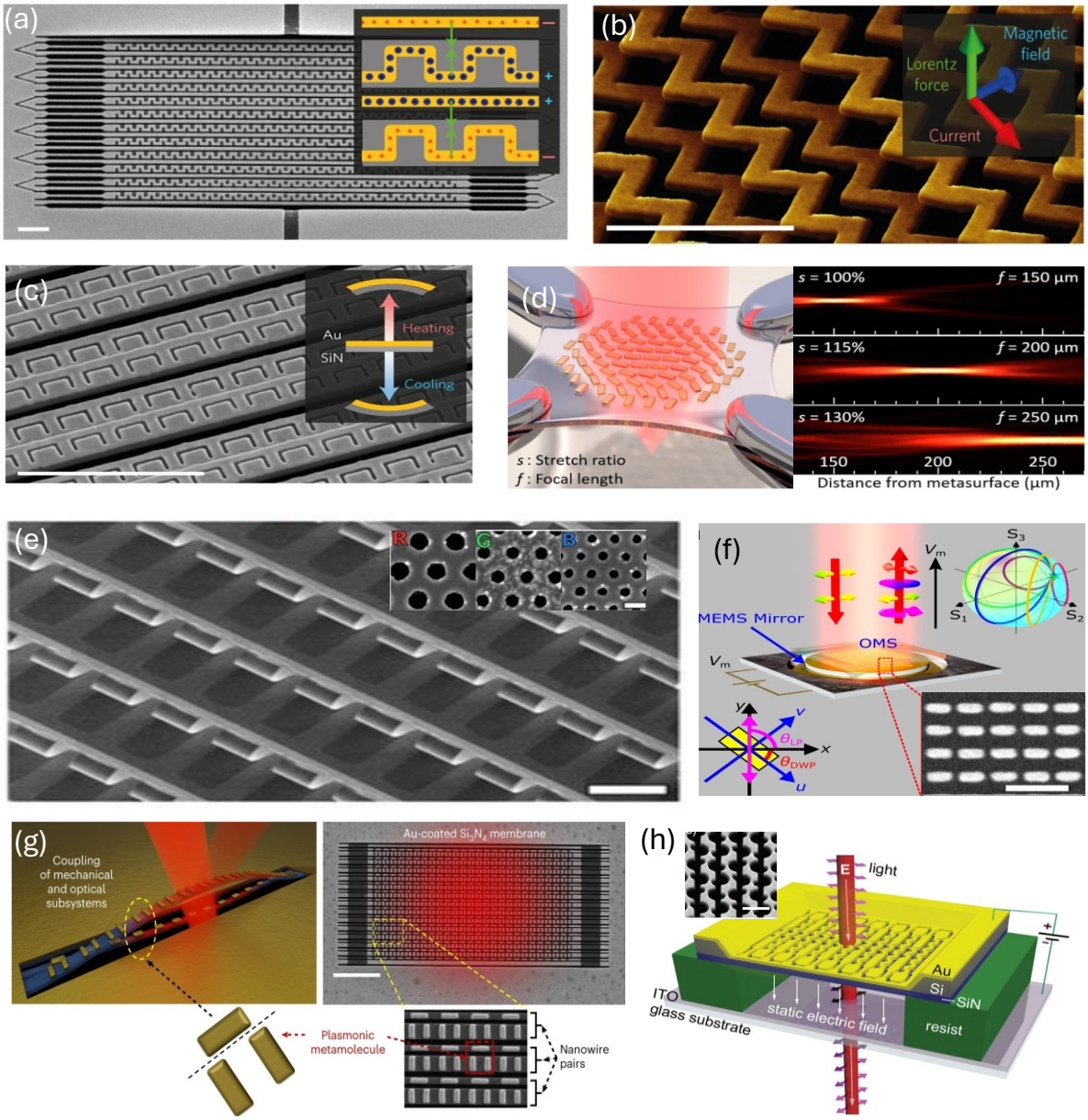

Figure 1.2: ***Reconfigurable nanomechanical photonic metamaterials.*** *(a) An electrostatic force driven meta electro-optic modulator[69]. (b) Plasmonic nanomechanical metamaterial actuated by the Lorentz force[70]. (c) Thermally reconfigurable nanomechanical metamaterial. The difference in thermal expansion coefficients of gold and silicon nitride layers makes the structure bend in different directions depending on heating or cooling[55]. (d) Illustration of a tuneable plasmonic metasurface with gold nanoparticles oriented at different angles. Longitudinal profile of transmitted beam for unstretched structure (stretch ratio, s =100%) and stretched cases (s= 115% and 130%) are shown. The focal length, f is indicated[66]. (e) MEMS- cantilever controlled plasmonic colours for optical displays. The different plasmonic nanohole arrays for red (R), green (G) and blue (B) are shown as inset[64]. (f) MEMS dynamic waveplate[63]. (g) Photonic metamaterial analogue of a continuous time-crystal. The nanowire pairs have π-shaped plasmonic metamolecules[27]. (h) Electrogyratory metamaterial suspended above an ITO-coated glass back-plane. Static electric field actuates the nanomechanical material, changing its chirality and optical activity[58]. Scale bars in a-c, h is* 2 μm*; e,* 50 μm *(inset 250* nm*); f,* 500 nm *and g,* 5 μm *long.*

All the above-mentioned nanomechanical structures are of micrometre length and nanoscopic cross-section. Their mechanical resonance frequency increases from MHz to GHz as the physical dimension reduces to the sub-micron scale. Such structures have an average thermal motion amplitude of 100s of picometers. For reference, a silicon atom has a van der Waals diameter of $\sim$220 pm. These vibrations often get lost in the noise floor of measurements and cannot be imaged directly using conventional frame-rate-limited and diffraction-limited cameras. To study and fully understand the functionalities of such nanomechanical structures and devices, their motion must be accurately detected and visualised. For example, accurate detection of thermomechanical motion is a key factor in metrology, as it can provide a reference for calibration of displacement sensitivity[5].

1.2 Nanomechanical motion detection techniques

Different optical/electrical/scanning probe-based techniques are employed to detect and image nanomechanical motion. A few of them are summarized below.

Optical nanomechanical motion detection techniques mainly use lasers to study the dynamics. Laser interferometry is a leading technique that comes under this. It works by splitting and recombining the coherent laser beams to generate interference patterns which are sensitive to tiny optical path changes that result from the displacement of nanomechanical structures[71]. It offers extreme displacement sensitivity ($\sim$1.2 fm/$\sqrt{\text{Hz}}$ [72]) enabling measurements down to the quantum limit in nanoscale devices. There are several interferometric modalities discussed in [71], like a simple two-path interferometer that uses modulation in the relative path length via nanomechanical motion to measure displacement (Figure 1.3a.1). Cavity-enhanced laser interferometry that uses either optical microcavities (Figure 1.3a.3) or whispering-gallery modes (Figure 1.3a.2) to enhance sensitivity. Laser Doppler vibrometry (LDV) is another technique that employs a laser for the detection and imaging of nanomechanical motion. It measures the Doppler frequency shift of the laser light reflected from a vibrating surface. This frequency shift is proportional to the velocity component of the oscillating surface, which is along the laser beam direction. A reference beam is frequency shifted and mixed with the Doppler-shifted scattered light. Using a heterodyne detection scheme, this signal is demodulated to extract the instantaneous velocity of the oscillating surface[73]. Both schemes have high sensitivity to optical path length change and are employed in nanomechanical imaging by raster scanning; however, the lateral spatial resolutions are diffraction-limited.

Scanning probe microscopy (SPM), such as atomic force microscopy (AFM), and scanning tunnelling microscopy (STM), utilises scanning probe near-field methods in the local detection of mechanical vibrations of individual nanostructures[74]. A nanoscale sharp physical probe is

scanned across the surface, and the interaction between the surface and the sample is monitored to map the topography, mechanical, magnetic, electronic, and chemical properties at the atomic or molecular scale. In [74], an SPM-based near field method that offers displacement sensitivity of 0.45 pm/$\sqrt{\text{Hz}}$ is presented (Figure 1.3b). A plasmonic probe tip of an AFM cantilever is placed in proximity of an externally driven double clamped nanomechanical beam resonator. The tip has line gratings on it, which act as a local source when a laser is shone on it. The generated localised surface plasmons are focused on the apex of the tip, creating a confined near-field spot. The localised plasmons are scattered into the far field due to the interaction between the tip and the moving surface and are detected using a photodetector. The variation in the detected intensity carries information about the mechanical oscillation. However, as scanning probe techniques rely on a probe, which typically has substantial mass compared to the nanomechanical object being studied, the observed dynamics may be perturbed by the presence of the probe. Furthermore, stiction can happen when raster scanning the mechanical probe due to van der Waals or electrostatic interaction.

Capacitive detection[75] is another nanomechanical motion detection technique (Figure 1.3c) that utilises electronics in displacement detection in MEMS and NEMS. Here, a change in capacitance between a mechanical resonator and a fixed electrostatic gate is measured to detect small motions. They offer sub-nanometre displacement sensitivity, but parasitic capacitance from wiring and other electrons often affects the sensitivity, hence requiring careful impedance matching and shielding. It senses motion along one axis and has spatial resolution limited by electrode size and configuration. This makes detailed mode shape mapping challenging without complex designs[76].

Electron microscopy offers superior spatial and temporal resolution (as discussed in Chapter 2) compared to conventional optical microscopy. It has been used for nanomotion characterisation through a pump-probe scheme in ultrafast transmission electron microscopy (UTEM), also known as 4D electron microscopy[77]. A femtosecond laser pulse (pump) excites the specimen, triggering ultrafast processes and electron pulses generated by photoemission from the cathode act as probes. The time delay between pump and probe pulses is scanned using optical delay lines, allowing observation of sample dynamics over time. Electron pulses in short intervals contain a smaller number of electrons, resulting in a lower signal-to-noise ratio. To compensate for this, the same event must be observed multiple times with varying delays between the trigger (pump) and probe (stroboscopic methods). This limits it to observation of repeatable motion and prevents continuous, real-time observation, i.e., observation of random (e.g., thermal) motion. It requires additional optics to initiate a laser pulse (clocking) and a precisely timed packet of electrons for imaging. Figure1.3d shows how the spatial location of a freestanding copper (Cu)

crystal cantilever has changed relative to the reference image ($t_{ref} = -10$ ns) as a function of the time delay using 4D electron microscopy[78].

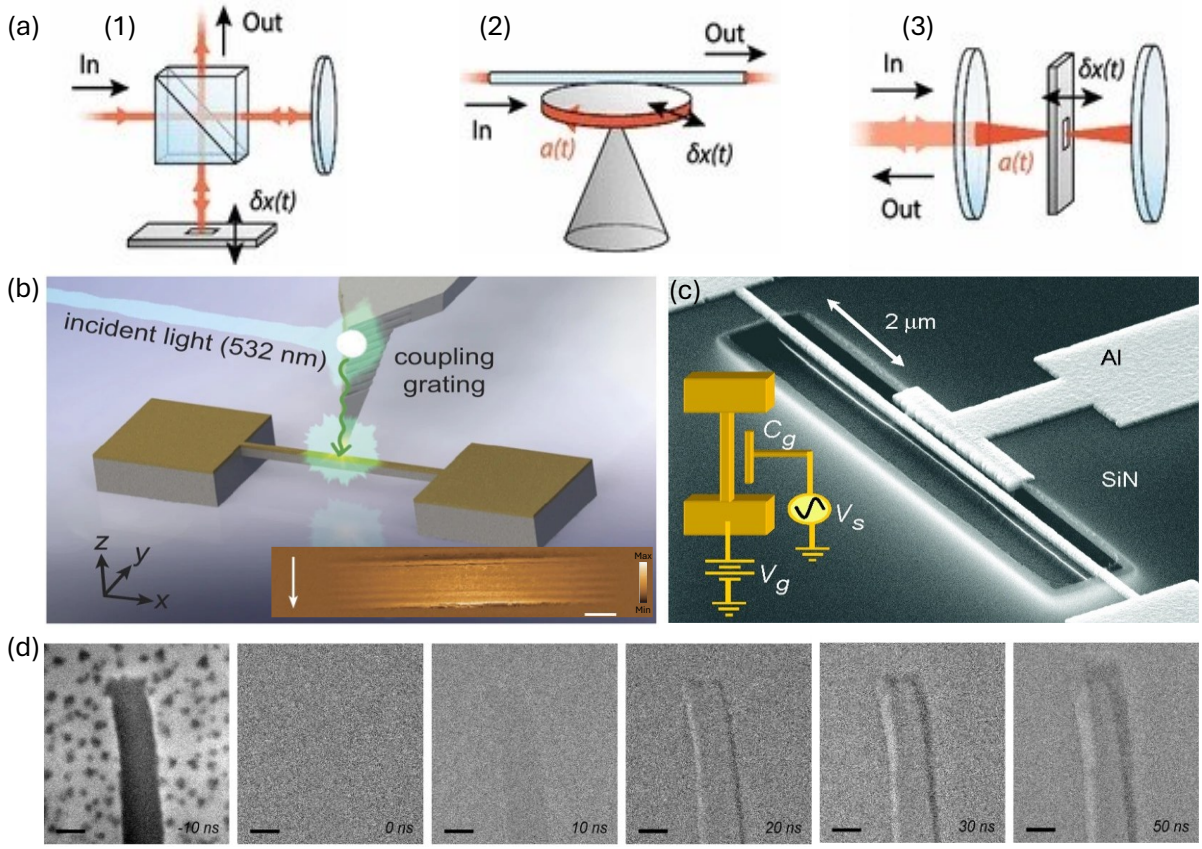

Figure 1.3: ***Selected existing nanomechanical motion detection and imaging techniques****. (a) Different laser interferometry configurations:(1) Simple two-path interferometer, involving reflection off the displacing ($\delta x(t)$) mechanical device. (2) Cavity-enhanced measurement, time-dependent amplitude (a(t)) of the optical field within the resonator (the intensity or energy stored in the optical cavity changes over time as a function of the mechanical displacement) interferes with the light through a closely placed fiber. (3) Using a Fabry–Perot configuration. Figures taken from[71]. (b) A scanning probe microscopy technique: An atomic force microscopy (AFM) cantilever that supports the plasmonic nano focusing probe. The inset shows a near-field optical image of the fundamental vertical bending mode shape of the nanomechanical resonator. Scale bar is* 2 μm *long[74]. (c) Capacitive readout: An SEM image of a nanomechanical doubly clamped beam resonator made of aluminium on a silicon nitride membrane kept close to an aluminium gate. The inset shows typical device biasing. The gap varies based on the motion of the nanowire, which changes the capacitance and, consequently, the resonance readout[75]. (d) 4D electron micrographs of a nanoscale cantilever: Reference image is taken before ($t_{ref} = -10$ ns) the arrival of clocking pulses. Subsequent images show the spatial location of the Cu crystal that changed relative to the reference image as a function of the time delay. The black spots are intentionally added to the substrate of the reference image to make sure that any sample drift can be distinguished from cantilever motion. The scale bar is* 200 nm *long[78].*

1.2.1 Secondary electron signals for nanomechanical motion detection

Avoiding all the complexity and expenses of a UTEM, subatomic motion detection and visualisation using an SEM is presented in[5, 79]. The method utilises the variation in secondary electron flux arising from the displacement of a nanomechanical structure (such as a cantilever shown in Figure 1.4a) relative to the electron beam position. This method is built on the fact that an electron beam kept at the edge of a sample will generate relatively more secondary electrons (SEs) than on the surface of the same, and no SEs are generated if the electron beam does not hit the sample. So, if the electron beam is to be placed at the edge of an oscillating structure, small motions can translate to significant changes in the secondary electron (SE) detector output signal amplitude. These changes are proportional to the displacement and the SE signal gradient in the displacement direction at the position of the electron beam impact (Figure 1.4b).

Conventional imaging techniques create motion blur when imaging moving objects if the displacement time scales are shorter than the frame rate. To avoid this, the time-dependent SE current is recorded at each point on the sample rather than integrating the signal over a fixed dwell time. This removes the coupling between object motion and frame rate, but there are still trade-offs: the signal is still sampled in discrete time steps, which constrains temporal resolution and the detectable frequency range. This can be further utilised for raster-scan imaging by detecting the SE signals on selected frequencies or by computing the Fourier spectrum at each point (Figure 1.4c). This way, a complete hyperspectral image can be created. Images constructed in this manner carry spatially resolved information on the mechanical motion phase and displacement amplitude within the detected frequency range. This hyperspectral motion visualisation (HMV) technique utilises the SEM's nanometric spatial resolution for imaging.

A major advantage of using electron beam instead of photons as a probe for motion detection is the high spatial resolution, i.e. along with detecting the motion of the object, the moving object can also be imaged with few nm of spatial resolution. If the requirement is only to detect motion and not give an importance to imaging at high spatial resolution, then it can be achieved optically if the motion modulates the measured observable, such as total intensity[80], phase, polarization, speckle pattern statistics[81] or refractive-index readout[82] in time. In that case, the dynamic information is carried by the temporal dependence of the light signal detected with sufficient bandwidth and signal-to-noise in the time domain.

The thermomechanical displacement power spectral density of an oscillator according to Wiener-Khinchin theorem is given by[83], $S(f_r) = k_B T f_o / 2\pi^3 m_{eff} \mathrm{Q} \left[(f_o^2 - f_r^2)^2 + \left(\frac{f_r f_o}{\mathrm{Q}} \right)^2 \right]$. Where k_B, T, f_o, and Q are Boltzmann constant, temperature, natural frequency, and

quality factor. The thermal motion amplitude x_{th} is given by $x_{th} = \sqrt{\int_0^\infty S(f_r)df_r}$. This technique offered a minimum detectable displacement with unitary signal-to-noise ratio of about 1pm for an integration time of 1 second, which is orders of magnitude better than the static imaging resolution of an SEM (a few nm).

This technique has been used in mass sensing[6], ballistic motion detection[1], study of Casimir effect[84], thermal imaging[85], etc. Chapters 4 and 5 rely on this nanomotion detection technique.

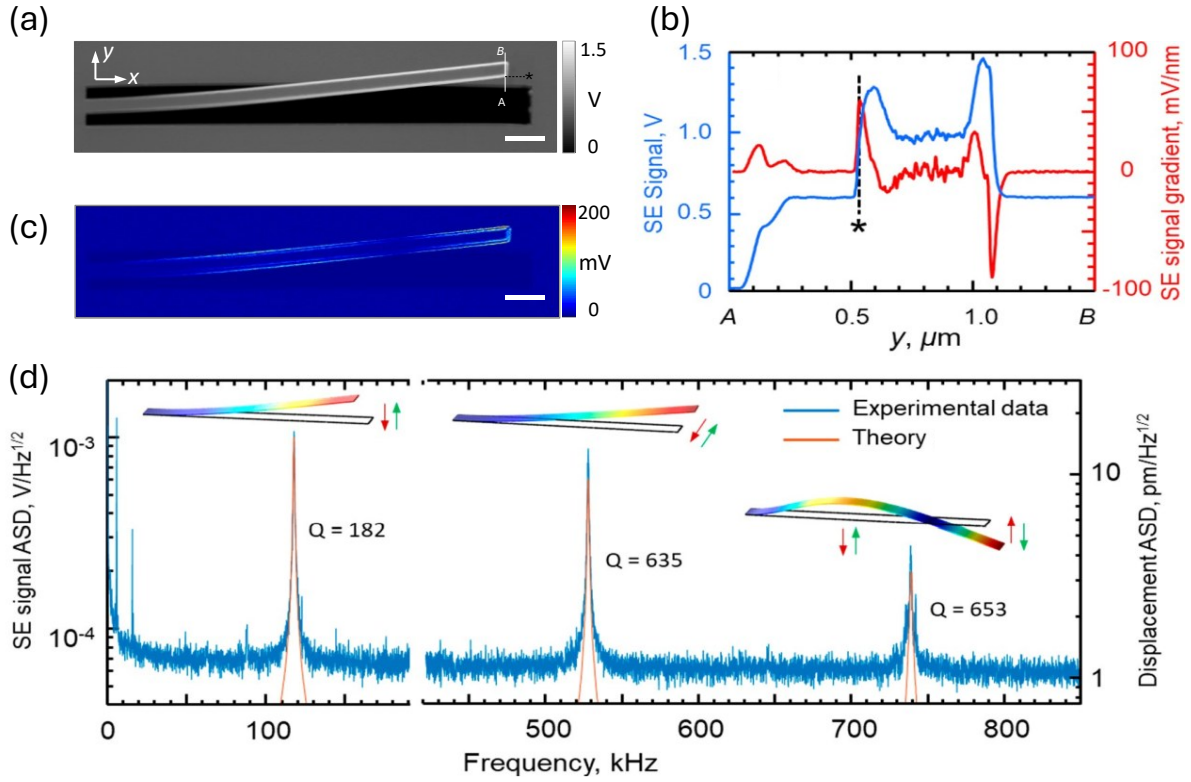

Figure 1.4: ***Thermomechanical motion visualisation of a cantilever using secondary electron signal.*** *Static secondary electron image (DC image) of a* 100 nm *thick,* 500 nm *wide,* 22 μm *long gold-coated silicon nitride cantilever. (b) Line scan profile along AB marked on the DC image. The DC secondary electron signal and its corresponding gradient are plotted. (c) SE signal modulation amplitude image, while the cantilever is mechanically driven at* 739.0 kHz *(second-order out-of-plane resonant frequency) by a piezoactuator. (d) Amplitude spectral density (ASD) of the secondary electron signal measured at the point * marked in a and b. The peaks correspond to the first out-of-plane oscillatory mode, the first in-plane oscillatory mode, and the second out-of-plane oscillatory mode of the cantilever (as denoted by the inset schematics), respectively. The values are calibrated to displacement amplitude spectral density (right-hand axis). The peaks match well with the theory. Respective quality factors (Q) are also indicated for each mode. The scale bar on a and c is* 2 μm. *Figures acquired from[5].*

When an electron beam interacts with a nanomechanical resonator, it not only detects motion but also exerts a force back on the resonator, known as dynamic backaction[4]. This backaction arises because the momentum and energy of the electrons couple to the resonator's vibrations. Depending on the timing of this feedback, the beam can either damp the motion, reducing thermal fluctuations (cooling) [3], or amplify the motion, enhancing vibration amplitudes[86]. Chapter 4 and 5 demonstrate on how electron beam induced charging and heating affect nanomechanical dynamics.

1.3 Thesis outlook

To summarise, the dynamics of nanomechanical structures like cantilevers and bridge beams are important. They are the building blocks of MEMS/NEMS and nanomechanical photonic reconfigurable metamaterials. The response of a nanomechanical structure to an external stimulus is often characterised by a shift in its resonance frequency and a change in mechanical motion amplitude. Hence, accurately detecting such nanomechanical motion becomes crucial. This thesis investigates the in-plane nanomechanical motion of externally driven nanomechanical structures (cantilevers and bridge beams (nanowires)) using a scanning electron microscope. The thesis addresses three questions: One, can nanomechanical motion visualising be achieved using cathodoluminescence? Two, what happens to the nanomechanical behaviour if the nanomechanical structure gets charged by an electron beam due to poor grounding? Finally, can the nonlinear behaviour of nanomechanical structures be controlled using electron beam-induced heating?

Chapter 2 is the background and methodology, where a general analytical equation for the in-plane and out-of-plane eigen frequencies for nanomechanical cantilevers and beam bridges is provided. How stress can affect such eigenfrequencies are addressed there. Forced oscillator dynamics of a linear oscillator are also discussed in detail, as the nanomechanical structures used throughout this thesis are externally driven. Electron beam-sample interactions and different cathodoluminescence emission processes are introduced here. A detailed analysis of how to utilise the cathodoluminescence process for nanomotion detection, along with an analytical equation for the noise equivalent displacement at a unity signal-to-noise ratio, is also derived. An equation that incorporates the electron beam position and electron beam diameter is also provided. These equations are tested using numerical simulations using a gold nanoparticle. The theory was tested using a spectrometer to determine if plasmonic material was a suitable choice for establishing the technique and to guide the selection of a brighter material (gallium nitride).

Chapter 3 reports the experimental demonstration of nanomotion detection and visualisation using cathodoluminescence. The study employs three externally driven GaN/Au/Si_3N_4 nanocantilevers of differing lengths, all driven in-plane. Their mechanical motion amplitudes are detected using lock-in detection. Nanomechanical motion imaging is also demonstrated using one of the cantilevers driven at its detected in-plane mechanical resonance frequency. Its mechanical displacement amplitude image, phase image, and mode profile are also shown.

Chapter 4 addresses how electron-induced charging affects nanomechanics. Here, the secondary electron detection scheme for nanomotion detection was utilized. Two identical cantilevers made with the same materials (GaN/Au/Si_3N_4) with one of them isolated by milling of the electrically conductive layer material at its anchor point, are externally driven to move in-plane. By setting the electron beam in 'spot mode' and changing its spatial location relative to one edge of each cantilever, a shift in resonance frequency is observed. A simple mathematical model is introduced to explain such dynamics. The analytical model aligns with the experiment, and the equation connects the resonance frequency of the nanomechanical structures to charge and electron beam parameters, such as beam current and acceleration voltage. The mechanical behaviour is also tested by variation of the beam current.

Chapter 5 looks into the nonlinear dynamics of a freestanding nanowire that is externally driven in-plane. Here, how electron beam-induced heating affects nonlinear behaviour is studied, such as the bistable resonant behaviour of a Duffing oscillator. The electron-beam-induced frequency shift in such behaviour is demonstrated in two ways: One, by fixing the electron beam at different locations from the edge of the nanowire and then doing a driving frequency sweep. Two, by fixing the frequency and doing an electron beam position sweep. A key finding is that the bistable mechanical states of a nanomechanical Duffing oscillator can be controlled and switched using an electron beam.

Finally, in the last chapter, a summary of all chapters is provided, with an emphasis on the key takeaways and some future implications.

Chapter 2 Background and establishing methodology

The scientific and technological importance of nanomechanical resonating structures were discussed in Chapter 1. With low mass and fast response times (kHz to GHz frequency), they are a potential candidate for many applications[43, 87, 88]. Progress in nanofabrication techniques has reduced the dimensions of such systems, making them more susceptible to external stimuli (e.g., pressure from colliding with air molecules, temperature, etc.). The functionalities of nanomechanical resonating structures depend on their movement, and perturbing noises can compromise their performance. Cantilevers, beams, strings, and membranes are the simplest and widely used forms of such resonators. These can be easily fabricated on commercially available, free-standing membranes. An advantage of such resonators is the wealth of analytical equations that connect their mechanics to their geometrical and material properties. These analytical models can also be used to predict how such resonators respond to external stimuli.

The chapter begins by discussing the mathematics that describes the eigenfrequencies of flexural modes in resonating structures, such as cantilevers and bridges. These are the resonator structures which were used in the experimental parts of this thesis. The section concludes with an analytical expression for the resonance frequency as a function of tensile stress. Such fast-oscillating low mass ($\sim$ pg) resonating structures are susceptible to perturbation due to external stimuli that can affect their mechanics, whether they are thermally driven or externally driven. All the works presented in this thesis utilise forced oscillations of such resonators. Hence, forced oscillator dynamics and their numerical simulations are addressed in Section 2.2.1. The third part addresses the benefit of the electron beam as a probe over the optical probe. This section will discuss cathodoluminescence and various forms of cathodoluminescence emission mechanisms. Chapter 3 addresses the use of cathodoluminescence for nanomechanical motion detection; hence, from Section 2.6 onwards, a detailed description of how this technique can be achieved will be provided. Towards the end of this chapter, the reason for using a brighter material, such as gallium nitride, over a plasmonic material like gold to establish the technique is addressed. The method of material deposition is also addressed in these sections.

2.1 Mechanical eigenfrequencies of nanomechanical structures

The Euler-Bernoulli beam model is used to describe the bending of narrow mechanical beams. A mechanical beam is said to be narrow when its length is much greater than its thickness ($L/h >$ 10). This model simplifies the problem by assuming that the beam does not experience shear deformation or rotational inertia. As explained in[83, 89], if the beam is made of a linear elastic

material and has the same cross-section along its length, its motion can be described by the following differential equation,

$$\rho A \frac{\partial^2 U(x,t)}{\partial t^2} + \frac{EM\partial^4 U(x,t)}{\partial x^4} = 0 \quad 2.1$$

Where ρ denotes the material density, A the cross-sectional area, E the Young's modulus, M the geometric moment of inertia, and $U(x,t)$, the displacement function. The solution can be expressed as the product of a spatially dependent and time-dependent function.

$$U(x,t) = \sum_{n=1}^{\infty} \phi_n(x) u_{o,n} cos(\omega_n t) \quad 2.2$$

where ω_n is the eigen frequency of the structure, n indicates the vibrational mode number, u_0 is the amplitude and t is the time. The general solution to the mode shape function $\phi_n(x)$ is of the form,

$$\phi_n(x) = a_n \cos(\beta_n x) + b_n \sin(\beta_n x) + c_n \cosh(\beta_n x) + d_n \sinh(\beta_n x) \quad 2.3$$

Here β_n is the wavenumber of the nth mode (units: m^{-1}), and the first two trigonometric terms in the above equation describe standing waves in the beam. The last two hyperbolic terms indicate the influence of the clamping on the vibration. The above equation tells that the beam oscillation has a specific vibrational mode, each with a unique spatial shape. Equation 2.1 then becomes,

$$-\rho A \omega_n^2 U(x,t) + EM\beta_n^4 U(x,t) = 0 \quad 2.4$$

This gives the equation for angular eigen frequencies as a function of wavenumber,

$$\omega_n = \beta_n^2 \sqrt{\frac{EM}{\rho A}} \quad 2.5$$

When the mechanical beam is fixed at one end and the other end is free to oscillate (cantilever), the boundary conditions that describe such a system are as follows[89, 90],

$$\phi_n(0) = \frac{\partial \phi_n(0)}{\partial x} = \frac{\partial^2 \phi_n(L)}{\partial x^2} = \frac{\partial^3 \phi_n(L)}{\partial x^3} = 0 \quad 2.6$$

Similarly, for a double clamped beam, the ends are fixed, hence the boundary conditions are,

$$\phi_n(0) = \frac{\partial \phi_n(0)}{\partial x} = \phi_n(L) = \frac{\partial \phi_n(L)}{\partial x} = 0 \quad 2.7$$

With $\Lambda_n = \beta_n L$, and enforcing the boundary conditions, we can determine Λ_n as well as a_n, b_n, $c_n, and\ d_n$ for the cantilever and a double clamped beam for $n = 1,2,3, n > 3$[89]. The values are provided in Table 2.1.

Table 2.1: ***Values of the mode-dependent parameter Λ_n for cantilever and bridge***

Mode number (n)	Λ_n	
	Cantilever	Double-clamped beam (Bridge)
1	1.8751	4.7300
2	4.6941	7.8532
3	7.8548	10.9955
$n > 3$	$(n-1)\pi + \pi/2$	$n\pi + \pi/2$

For a beam with rectangular cross-section, the moment of inertia while considering the in-plane motion (along the width, W) is $M = h\frac{W^3}{12}$ and for out-of-plane motion (along the thickness, h), $M = W\frac{h^3}{12}$. Therefore, with an area $A = Wh$, the equation for the in-plane flexural mode (along the plane of the structure),

$$f_n = \frac{\omega_n}{2\pi} = \frac{\Lambda_n^2 W}{2\pi\sqrt{12}L^2}\sqrt{\frac{E}{\rho}} \qquad 2.8$$

and for out-of-plane (along the thickness direction),

$$f_n = \frac{\Lambda_n^2 h}{2\pi\sqrt{12}L^2}\sqrt{\frac{E}{\rho}} \qquad 2.9$$

The analytical formulas are verified with numerical simulations. A simple cantilever and a nanowire (double clamped beam) with rectangular cross-section is considered for that. Stress-free silicon nitride (Si_3N_4) is used as the material with length L = 25 µm, thickness h = 50 nm, width W = 200 nm, Young's modulus E = 260 GPa, density ρ = 3100 kg/m^3. The simulations were done with the finite element method (FEM) modelling using COMSOL Multiphysics. Since all the oscillations considered in this thesis are in-plane, Equation 2.8 is used to calculate the analytical mechanical in-plane eigenfrequencies for the first three modes of the cantilever (nanowire). The estimated values were 473.41 kHz (3.01 MHz), 2.96 MHz (8.30 MHz), and 8.30 MHz (16.28 MHz), respectively. The values are in good agreement with the simulated values: 473.43 kHz (3.01 MHz), 2.96 MHz (8.30 MHz), and 8.30 MHz (16.26 MHz), respectively. The simulated mode shape and its respective in-plane resonance frequencies are shown in Figure 2.1.

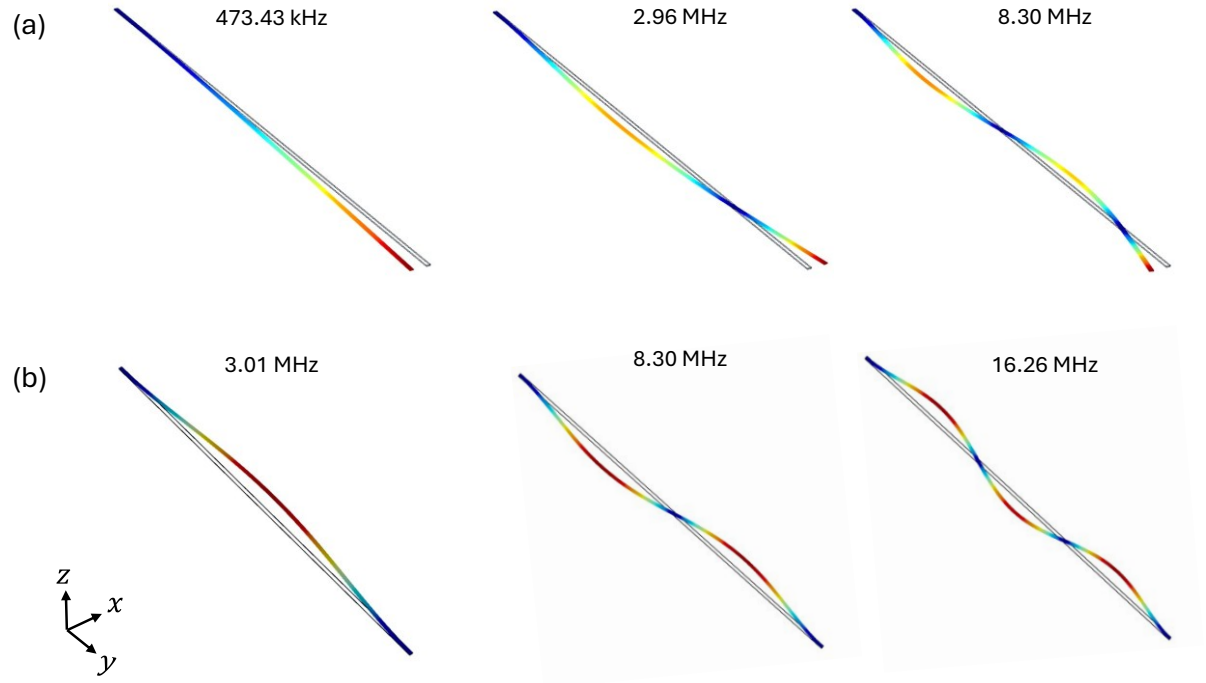

Figure 2.1: ***Simulated mode shapes and corresponding in-plane eigen frequencies of a stress-free silicon nitride nanoresonator with length*** *L* = 25 µm***, thickness*** *h* = 50 nm***, and width*** *W* = 200 nm***.*** *(a) The first three modes of a cantilever's in-plane oscillation. (b) The first three modes of a nanowire's in-plane oscillation.*

The simulation shows the position of the cantilever and the nanowire where maximum displacement is expected. Since only the first in-plane modes are considered throughout the thesis, keeping the probe (electron beam) next to the tip of a cantilever's edge and near the middle of a nanowire's edge will ensure good signal detection, as the amplitude of mechanical oscillation will be high at these locations.

The case presented above considers a stress-free mechanical beam. However, due to the design or because of fabrication procedures, the thin films and membranes used for the fabrication of such nanomechanical structures are pre-stressed. High stress is favoured in free-standing membranes as it enhances the quality factor of the resonance frequencies. In mechanical beams, increasing tensile stress (σ) will increase the resonance frequencies. Following [89], the analytical expression for the stress-dependent resonance frequency of a mechanical beam has the form,

$$f_n = \frac{\Lambda_n^2}{2\pi L^2}\sqrt{\frac{EM}{\rho A}}\sqrt{1+\frac{\sigma A L^2}{EM\lambda_n^2}} \qquad 2.10$$

The additional stress-dependent term, $\sqrt{1+\frac{\sigma AL^2}{EM\Lambda_n^2}}$ multiplied by the stress-free eigenfrequency term, $\frac{\Lambda_n^2}{2\pi L^2}\sqrt{\frac{EM}{\rho A}}$ tells that an increase in stress increases the resonance frequencies. A relevant example is tuning the strings of a guitar by adjusting their tension. Equation 2.10 shows that stress can act as a tuning parameter for nanomechanical resonance frequencies, and this idea was utilised to control the bistable response of a nanomechanical wire in Chapter 5. Figure 2.2 shows how the in-plane resonance frequency of the first mode changes as a function of stress. The same Si_3N_4 nanowire geometry used for numerical simulation in Figure 2.1b is used here.

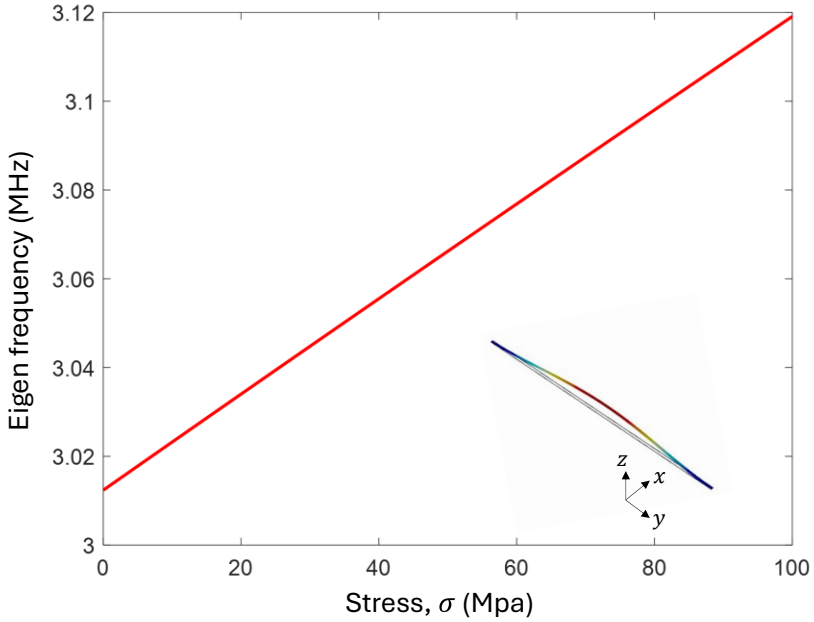

Figure 2.2: ***Fundamental in-plane resonance frequency as a function of stress of a silicon nitride nanowire****. The simulated first mode is provided as an inset.*

2.2 Dynamics of nanomechanical structures

The free vibration (eigen frequency) of mechanical resonators was discussed in Section 2.1 without considering any dissipative forces; hence, the energy remained constant. In reality, mechanical vibrations of elastic elements like beams, strings, and membranes store potential energy as deformation energy like a spring. When such elements displace from their rest position, the restoring forces cause the system to accelerate back to its original position, provided the displacement force is within the elastic limit of the element. While restoring the original position, the physical system generates kinetic energy and traverses the equilibrium position and displaces to the opposite direction. This generates a new deformation energy. The dissipative forces prevent this periodic energy conversion from sustaining itself indefinately and dampen the periodic oscillation amplitude over time. In a real vibrational system, dissipation can occur in

various ways, primarily based on the interaction with the medium surrounding the resonator, energy losses from the resonator's clamping location, and intrinsic losses within the bulk and surface of the resonator materials[89, 91-93].

When the nano resonator is in a gaseous medium, the damping is attributed to momentum transfer between gas molecules and the resonator, occurring at a rate proportional to their relative velocity. The ratio between the mean free path of the gas molecules and the physical length scale of the nanomechanical beam (Knudsen number K_n) determine what losses dominate for the damping mechanism[94]. When the $K_n < 0.01$, the gas behaves like an incompressible viscous fluid, and the energy dissipation is due to the viscous flow of the fluid around the mechanical resonator.

In all the experimental studies presented in this thesis, the nanomechanical resonators were kept in the high vacuum chamber of the SEM ($\sim 10^{-6}$ mbar). A low gas pressure means a high K_n and for samples kept at such low pressures, K_n can be way greater than 10. In such cases, the intrinsic losses contribute to the dissipation. The phonon-phonon scattering, acoustic-thermal phonon scattering (thermoelastic damping), phonon-electron scattering, and surface losses are a few such intrinsic dissipation mechanisms[89, 91-93]. There will also be damping through the anchor sites of the resonator over which the vibrational energy is radiated into the environment. Overall, the dissipation factor is,

$$\mathrm{Q}_{\mathrm{total}}^{-1} = \sum Q_i^{-1} \qquad 2.11$$

Where Q_i^{-1} is the contribution from each of the dissipation mechanisms.

2.2.1 Forced oscillator dynamics

The nanomechanical resonators used in the thesis (cantilevers and nanowires with rectangular cross-section) are under forced oscillation. Hence, their dynamics can be studied with the help of a 1D damped harmonic oscillator model under forced oscillation. Assuming the nanomechanical resonator is oscillating in the x direction, following [83, 89, 91, 95-97], the dynamics of the nanomechanical resonator $x(t)$ with an effective mass m_{eff} are described as,

$$m_{eff}\ddot{x}(t) + b\dot{x}(t) + kx(t) = F_{ext}(t) + \xi(t) \qquad 2.12$$

Where, $\ddot{x}$ is the acceleration, $\dot{x}$ is the velocity, b is the damping coefficient, k is the spring constant, and $\xi(t)$ is the Langevin random thermal force**.** If the resonator experiences any electrostatic forces, they must also be included in Equation 2.12. This is shown in Chapter 4.

Assuming an external periodic sinusoidal driving force $F_{ext}(t) = F_o \cos(\omega_d t)$, where ω_d is the driving angular frequency, F_o is the amplitude of the driving force, and considering that $F_{ext}(t) >> \xi(t)$, the effect of the thermal force $\xi(t)$ can be neglected in the following derivation. Equation 2.12 becomes,

$$\ddot{x}(t) + \gamma_m \dot{x}(t) + \omega_m^2 x(t) = \frac{F_o cos(\omega_d t)}{m_{eff}} \quad 2.13$$

Where, $\omega_m = \sqrt{k/m_{eff}}$ is the undamped angular frequency, as discussed in Section 2.1. The dissipation factor is defined as $\gamma_m = \frac{b}{m_{eff}} = 2\zeta\omega_m$, where $\zeta = b/(2\sqrt{km_{eff}})$ denotes the damping ratio. Following [89], the steady state solution is derived by assuming a complex variable for the driving force $F_{ext}(t) = F_o e^{i\omega_d t}$ and a trial solution $x(t) = A_o e^{i(\omega_d t - \varphi)}$ where A_o is the amplitude of mechanical oscillation and φ is the phase angle. Substituting the trial solution into Equation 2.13 and solving will give,

$$\left(-\omega_d^2 + \gamma_m\, i\omega_d + \omega_m^2\right) A_o e^{i(\omega_d t - \varphi)} = \frac{F_o e^{i\omega_d t}}{m_{eff}} \quad 2.14$$

Which reduces to,

$$\left(-\omega_d^2 + \gamma_m\, i\omega_d + \omega_m^2\right) A_o = \frac{F_o e^{i\varphi}}{m_{eff}} \quad 2.15$$

After expanding and separating real and imaginary parts, the amplitude as a function of driving frequency becomes,

$$A_o(\omega_d) = \frac{\frac{F_o}{m_{eff}}}{\sqrt{(\omega_m^2 - \omega_d^2)^2 + (\gamma_m \omega_d)^2}} \quad 2.16$$

And the phase,

$$\varphi(\omega_d) = arctan\left(\frac{\omega_d \gamma_m}{\omega_m^2 - \omega_d^2}\right) \quad 2.17$$

Equations 2.16 and 2.17 can be qualitatively understood from Figure 2.3, where three different γ_m are considered (units are ignored here). When ω_d nears ω_m, the amplitude of a slightly damped resonator system attains maximum amplitude and a phase shift of $\pi/2$, That is, from Equations 2.16 and 2.17, $A_o = F_o/(m_{eff}\omega_m\gamma_m)$ and $\varphi = \pi/2$. The frequency at which the highest amplitude is achieved is called the resonance frequency ω_o and is found at $\frac{\partial A_o}{\partial \omega_d} = 0$,

$$\omega_o = \sqrt{(\omega_m^2 - \gamma_m^2/2\,)} = \omega_m\sqrt{1-2\zeta^2} \qquad 2.18$$

For all the nano resonators considered in the thesis $\gamma_m \ll \omega_m$ hence, $\omega_o \approx \omega_m$. This can be seen in Figure 2.3a. As the damping rate decreases, the mechanical motion amplitude increases, and a sharp peak is observed. The slope of the corresponding phase response (Figure 2.3b) at resonance also becomes steeper with lower damping. Following [89], in the limit of a small damping rate ($\gamma_m \ll \omega_m$) the quality factor Q $\approx 1/2\zeta$ is inversely affected by damping factor ($\gamma_m \approx \omega_o/\mathrm{Q}$). Under this condition the full width half maximum (FWHM) of the resonance amplitude curve becomes approximately equal to γ_m. Quality factor is a dimensionless parameter that acts as the amplification factor of the vibration of a linear resonator at resonance. It quantifies the damping time ($\tau_d = \gamma_m^{-1} = \mathrm{Q}/\omega_o$) or how many cycles are needed for the nanomechanical resonator to lose its energy to the environment. It is also defined as,

$$\mathrm{Q} = 2\pi\left(\frac{Total\ energy\ stored\ in\ the\ system}{Energy\ lost\ per\ cylce\ of\ oscillation}\right) \qquad 2.19$$

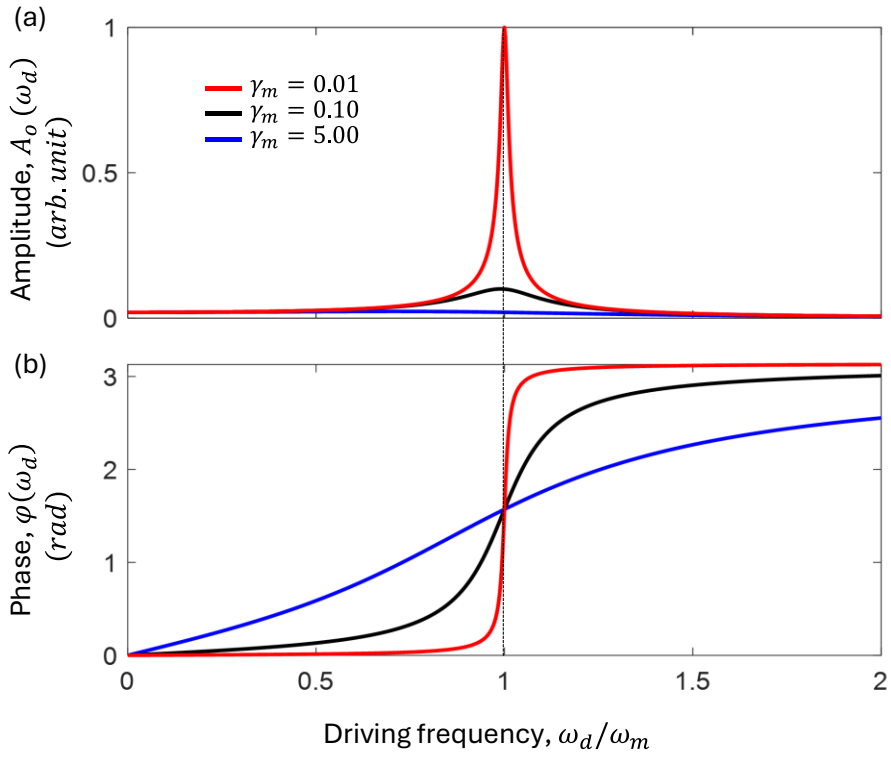

Figure 2.3: ***Mechanical motion amplitude*** *(a)* ***and phase*** *(b)* ***of mechanical oscillators as a function of driving frequency for different dissipation factors*** *(γ_m).*

In this section, instead of using the total geometrical mass m, the effective mass (m_{eff}) of the resonator was considered. This is because the displacement along the resonator is not uniform across its length, and a correction is required to capture how the displacement is along the structure. The effective mass provides this correction, allowing the amplitude of motion to remain unchanged while properly reflecting the displacement profile. For a resonator vibrating in its n^{th} mode, the effective mass can be derived from its potential energy. Following [83], if the resonator is divided into infinitesimal volume elements dV each with mass $dm = \rho\, dV$, the potential energy of each element can be expressed as,

$$\frac{1}{2}\, dm\, \omega_n^2\, \boldsymbol{U}(\boldsymbol{r},t)^2 = \frac{1}{2}\rho\, dV\, \omega_n^2\, |x_n(t)\boldsymbol{\phi}_n(\boldsymbol{r})|^2 \qquad 2.20$$

Where $x_n(t)$ is determined from mapping each mechanical mode to a damped harmonic oscillator. $\boldsymbol{\phi}_n(\boldsymbol{r})$ is the normalised three-dimensional mode shape. Volume integral over the entire structure will give,

$$\frac{1}{2}\omega_n^2|x_n(t)|^2 \int \rho\, |\, \boldsymbol{\phi}_n(\boldsymbol{r})|^2\, dV = \frac{1}{2}\omega_n^2|x_n(t)|^2 m_{eff,n} \qquad 2.21$$

Which implies that while considering one-dimensional motion of resonators with uniform cross-section, such as the ones used in this thesis, the effective mass can be determined by,

$$m_{eff,n} = \rho A \int_0^L |\, \phi_n(x)|^2\, dx \qquad 2.22$$

For ideal geometries with uniform density distribution, a mode-independent value is obtained for the mass ratio (m_{eff}/m)[83, 98]. That is for a single-material cantilever beam of uniform rectangular cross-section, m_{eff} = 0.25m, while for a single-material bridge beam m_{eff} = 0.4m. In general cases the volume integral can be numerically evaluated using methods like finite element modelling.

Having discussed the mathematics of nanomechanical resonators' motion in the preceding sections, the focus now shifts to the problem of detecting and visualising their motion. At smaller dimensions, the thermal (i.e., Brownian) motion of such objects under vacuum, which are driven "internally" by momentum transfer from the annihilation, creation, and interference of phonons *[99]*, becomes important. The thermal motions have pico-nanometric displacement amplitudes for different eigenfrequencies. Observing the variation in that displacement can be used to sense anything that influences such motion, such as temperature, acceleration, pressure, etc. Hence, accurate detection of such motions becomes important. A few of the important methods were discussed in Chapter 1, which concluded with a technique that utilises an electron beam as a probe.

2.3 Electron as a probe

Abbe's law of diffraction[100] restricts the resolution of conventional optical microscopy, because two points that are spaced less than half the free space wavelength (λ_0) cannot be resolved by a conventional optical microscope. A beam of fast electrons could be used as an alternative source since an electron has a de Broglie wavelength which is many orders smaller than a photon of the same energy (e.g., a 2 eV electron's wavelength is 0.86 nm and a photon at the same energy has a wavelength of 620 nm)[101]. Increasing the electron's energy further reduces its de Broglie wavelength. For example, an electron with an energy of 10 kV (SEM acceleration voltage used throughout this thesis) has a de Broglie wavelength of approximately 12 pm. This makes electrons a perfect source for imaging nano samples with high spatial resolution. The difference in using optical and electron-based techniques for studying a nanoscale object is shown in Figure 2.4.

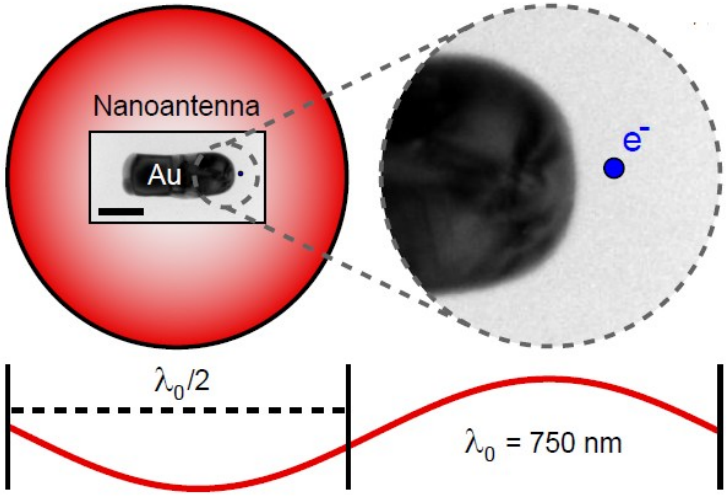

Figure 2.4: ***Difference between an optical probe and an electron probe.*** *Bright-field transmission electron micrograph of a* 125 nm *long gold rod on a* Si_3N_4 *membrane, which acts as a nanoantenna and is resonant at* λ_0 = 750 nm. *The scale bar is* 50 nm. *The overlaid red circle represents a diffraction-limited spot for* λ_0 = 750 nm *and a numerical aperture* = 1. *The small blue dot represents a* 5 nm *electron beam (to scale). The magnified image of the area enclosed by the grey dashed circle shows the higher spatial resolution of an electron beam. Image adapted from[101].*

2.3.1 Electron beam-sample interaction

When electron beams (typically 0.1 kV to 400 kV in energy/electron) interact with a sample inside an electron microscope, they can scatter off the sample elastically and inelastically[102-104]. Such a scattering process gives rise to many interaction products such as secondary electrons (SEs), backscattered electrons (BSE), X-radiation, Auger electrons (AE), cathodoluminescence (CL), transmitted electrons (for thin samples), absorbed specimen current and localised heating

(shown in Figure 2.5a). Most electrons of an incident electron beam (also referred to as the primary electron beam in this thesis) come to rest within a droplet-shaped volume known as the interaction volume. The size of the interaction volume increases with increasing acceleration voltage (V_e) and decreases with increasing atomic number (Z). The different types of interaction products typically arise from a certain depth of the material thickness when the electron beam is incident on the material (Figure 2.5b).

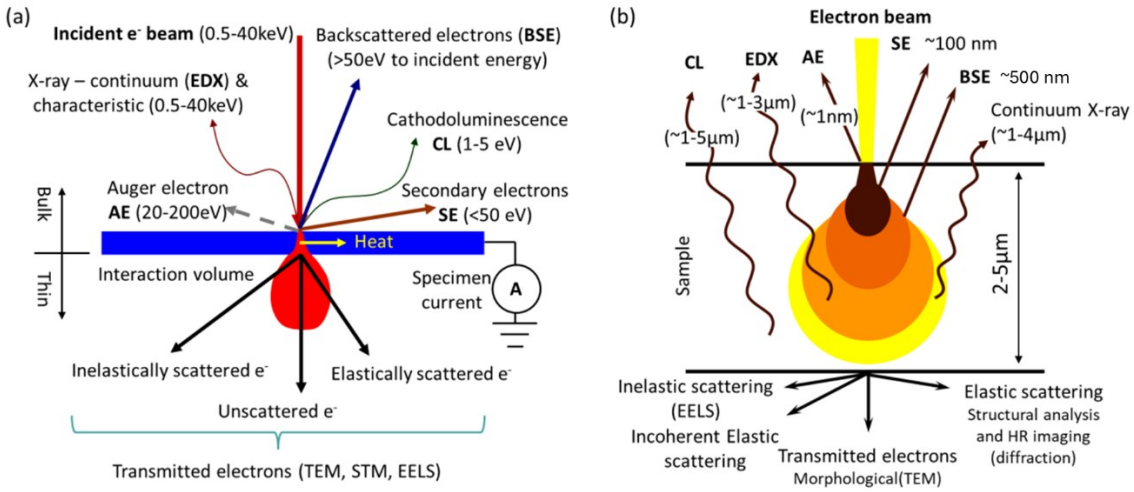

Figure 2.5: ***Electron beam-specimen interaction****.(a) Different secondary emissions resulting from electron beam interactions, along with their corresponding energy distributions. (b) Interaction volume and different parts where signals are emitted. Images are adapted from[103].*

The primary electrons inelastically collide with the atoms on the surface of the sample, and the outermost electrons are detached from the atoms. These electrons, with low kinetic energy (< 50 eV), are emitted into the vacuum as secondary electrons. Since the SE is formed at the surface of the specimen, it is used for high-resolution surface imaging in electron microscopes. Fewer SEs are emitted from a flat surface than from an oblique surface and edges because more surface is interacting with the primary electron beam in the latter cases. This is why the edges of samples imaged using an SEM look brighter. Backscattered electrons (BSE) are primary beam electrons that undergo elastic collisions with atoms in the sample and are deflected back out of the material. The higher the atomic number (Z), the greater the backscattering effect. This sensitivity to Z, along with X-ray spectra, is used in analytical SEM to identify the bulk specimen material. Due to them (BSEs) emerging from deeper locations of the sample, they have lower resolution than SE when used for imaging. X-rays are formed when an incoming electron knocks an electron off the innermost shell of an atom, and that vacancy is filled by an electron from a higher atomic orbital. They are suitable for elemental identification using wavelength-dispersive or energy-dispersive X-ray spectroscopy (WDX or EDX). Auger electrons are emitted along with the X-ray photons as a result of a secondary process. When the X-rays are emitted, some of them get reabsorbed, knocking out an electron from the upper shell. AE is used for elemental analysis of

the surface. The bombardment of primary electrons also generates light, known as cathodoluminescence (CL).

The energy of the CL photons can vary from 1 eV to 5 eV (infrared, visible, and ultraviolet light) and is generated through different processes, which are covered in Section 2.5. After utilising the primary electron beam for all the above-mentioned processes, the remaining net electron current on the specimen is conducted to earth via a high-tension circuit. If not grounded properly or if the sample is a semiconductor or an insulator, the primary electron beam can build up negative charge on the sample. This can affect the imaging process; hence, thin conductive layers are added to avoid this. Chapter 4 discusses how electron-induced charging can impact nanomechanical response. The excess energy of the electrons remaining after all the ionisation and emission processes will be converted to heat. Chapter 5 discusses how such heating can be utilised to control the bistable behaviour of nanomechanical resonators. For thin samples, the primary electrons can penetrate through them. The energy of the transmitted electrons varies depending on the type of collisions the primary electrons undergo with the sample as they propagate through it. It can be elastically scattered electrons (zero to small energy loss), inelastically scattered electrons (varying amount) or unscattered electrons (no energy loss). They are used in elemental analysis using the electron energy loss spectrum (EELS).

Recently, the secondary electron current gradient was used to study picometre movements of nanomechanical structures [5] (see Chapter 1). This led to the question of using other forms of emission signals, such as those mentioned above, for visualising nanomechanical motion. Light emission in the form of cathodoluminescence (CL) seems to be an excellent candidate.

Cathodoluminescence nanoscopy has advanced over the last few decades[105]. The emitted light from the interaction of an electron beam with a material carries much information encoded in its spatial, temporal, angular, and spectral distribution, as well as its phase and intensity. This features finds applications in determining the polarisation of the light[106], nanoscale relative-phase mapping[107], optical properties of nanostructures[108], the local density of optical states (LDOS)[109], resonant plasmonic modes of nanostructures[110], tomography[111], thermal properties of nanostructures[112] etc. Using a pulsed electron beam generated by a laser-driven photocathode[113] or through an electrostatic beam blanker[114] and a fast detector, the emission decay as a function of time can be tracked, allowing measurement of excited state lifetimes and carrier dynamics. This enables time-resolved cathodoluminescence measurements. This technique has been reported to be used in the study of exciton-carrier dynamics[115, 116] and ionisation radiation-induced excited states in DNA[117]. A hybrid measurement with continuous and pulsed electron beam, along with photon time correlation, is employed to study excitation and emission processes in a wide range of materials. The sample is

excited by a continuous electron beam, and the interval between detected photons emitted from the sample is measured using time-correlated single photon counting (TCSPC) or other correlation methods ($g^{(2)}$) to study the lifetimes of quantum emitters, such as point defects in hBN[118] and NV centres in diamond[119, 120].

Though CL shows the potential for detecting lifetime events, to the best of my knowledge, no nanomechanical motion detection technique has been demonstrated using cathodoluminescence. Emissions such as X-rays, AE, BSE, and transmitted electrons are beyond the scope of this thesis.

2.4 Electromagnetic field of an electron moving in a vacuum

An electron (a point charge) travelling in a vacuum with constant velocity does not radiate, since electron dispersion lies outside the light cone of free space [121]. Therefore, the electromagnetic (EM) fields associated with the electron decay exponentially away from its trajectory. The spatial, spectral dependence of the electric field ($\boldsymbol{E}(\boldsymbol{r_e}, \omega_e)$) and magnetic field ($\boldsymbol{H}(\boldsymbol{r_e}, \omega_e)$) (in Gaussian units) of an electron moving in a vacuum is given by[121-123],

$$\boldsymbol{E}(\boldsymbol{r}_e, \omega_e) = \frac{2e\omega_e}{v_e^2 \gamma_e \varepsilon_M} \, e^{\frac{i\omega_e z_e}{v_e}} \left[\frac{i}{\gamma_e} K_0\left(\frac{\omega_e R_e}{v_e \gamma_e}\right) \hat{\boldsymbol{z}}_e - K_1\left(\frac{\omega_e R_e}{v_e \gamma_e}\right) \widehat{\boldsymbol{R}}_e \right] \tag{2.23}$$

$$\boldsymbol{H}(\boldsymbol{r}_e, \omega_e) = \frac{2e\omega_e}{v_e^2 \gamma_e \varepsilon_M} \, e^{\frac{i\omega_e z_e}{v_e}} K_1\left(\frac{\omega_e R_e}{v_e \gamma_e}\right) \widehat{\boldsymbol{\varphi}}_e \tag{2.24}$$

Were $\gamma_e = 1/\sqrt{1 - v_e^2/c^2}$ is the Lorentz contraction factor, v_e is the electron velocity, c is the velocity of light, K_0 and K_1 are the modified Bessel functions of the second kind, ε_M is the permittivity of the medium, and $\boldsymbol{r_e}$ = ($\mathbf{R_e}$, z_e) is the position coordinate vector. The first term inside the bracket of Equation 2.23 is the field along the electron propagation direction (z_e), and the second term is along the radial direction ($\mathbf{R_e} = (x_e, y_e)$). The magnetic field along the azimuthal direction φ_e is given by Equation 2.24. The nature of these evanescent fields is studied by plotting the Bessel functions of Equations 2.23 and 2.24 with respect to their argument (ζ) (Figure 2.6). The argument itself is a multivariable term. If we fix the angular frequency (ω_e) associated with electron and electron velocity (v_e), the argument becomes directly proportional to the radial distance from the electron's trajectory (R_e), showing the radial dependence of the EM fields.

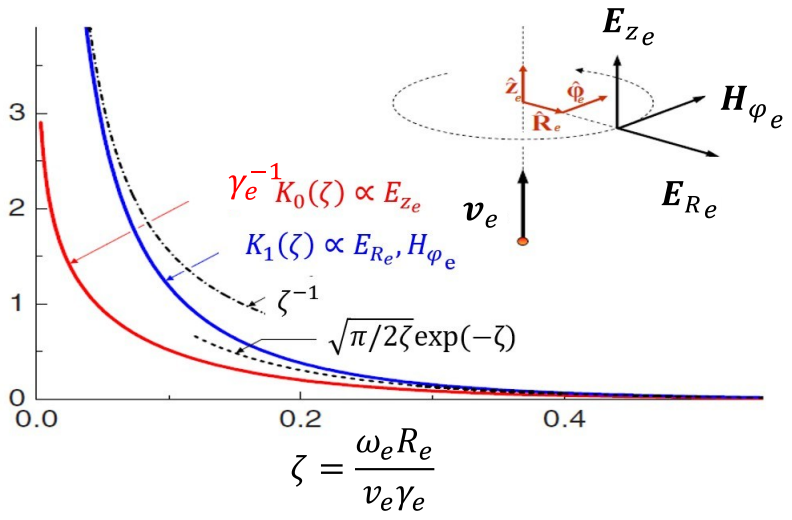

Figure 2.6: ***Evanescent character of the electromagnetic field produced by a fast electron****. Transverse-spatial direction dependence of the* $e^{i\omega_e\left(\frac{z_e}{v_e}\right)}$ *contribution to the electromagnetic field of an electron moving in a vacuum with velocity* v_e *= 0.7c (*$\gamma_e \approx 1.4$ *and kinetic energy ≈ 200* kV*) along the positive* z_e*-axis. The only nonvanishing components (*$\boldsymbol{E}_{R_e}, \boldsymbol{E}_{z_e}$ *and* $\boldsymbol{H}_{\varphi_e}$*) decay exponentially at a large distance* R_e *from the trajectory. The inset shows the orientation of these components relative to the electron velocity vector (*$\boldsymbol{v}_e$*). The small-R limit is dominated by the* $1/R_e$ *divergence of* $\boldsymbol{E}_{R_e}$ *and* $\boldsymbol{H}_{\varphi_e}$*. The figure is taken from[121].*

Figure 2.6. shows that the electric field diverges at the origin, implying that the field strengths change rapidly with distance from the trajectory. Techniques like CL rely on the interaction between the electron's field and the sample. Since the field is tightly localised around the trajectory (confined to a few nanometers to picometers) of the electron, an electron can selectively excite small regions of the sample. This localisation is the reason for the high excitation resolution of electron beam spectroscopies. The field amplitude decays with increasing distance from the trajectory. The electromagnetic field extends to a characteristic radial distance of $\sim v_e\gamma_e/\omega_e$.

2.5 Cathodoluminescence

Cathodoluminescence is far-field optical radiation resulting from the interaction of high-energy free electrons and polarisable materials. It was first observed as a glow in vacuum tubes used for cathode ray studies[124, 125]. Initially, CL was widely used in mineralogy for studying spatial compositional variations and spectroscopic properties of minerals, semiconductors, and other luminescent solids, as well as biological specimens[126-128]. The progress in photonics and plasmonics in recent decades has led to further advances in CL. Electrons moving in a vacuum can be considered an evanescent supercontinuum light source with broadband frequency components spanning the UV to infrared spectral regimes[129]. This gives CL a broadband character which is suitable to be used for studying different materials and structures. There are

several mechanisms through which light is emitted, and they are classified as coherent and in-coherent cathodoluminescence.

2.5.1 Coherent and incoherent cathodoluminescence

The electron's evanescent field makes light emission possible when an electron hits or passes near a polarisable material (e.g., gold). The field polarises the material, causing the excited modes to oscillate, possibly leading to far-field radiation[119, 130]. They can be localised on the surface of metal nanoparticles[131] and can undergo radiative decay, contributing to CL. Some plasmons can propagate on a surface, known as surface plasmon polaritons (SPP)[132]. For a coherent CL, the generated light will have a fixed phase relation with the electron's evanescent field[121]. Different types of coherent emissions exist, such as Cherenkov radiation (CR), diffraction radiation, transition radiation (TR), and plasmon generation. These emissions can interfere with each other. The CL emission probability is low in these processes $\sim 10^{-4}$ photons/electron[121, 125].

Cherenkov radiation occurs when electrons travel faster than the speed of light in a medium[133]. Diffraction radiation occurs when an electron passes near a structured surface without actually hitting it[134]. The electromagnetic field of the electron can scatter off the boundary of an object into the far field as light. It is known as Smith-Purcell radiation when an electron moves parallel to a grating or row of nanoparticles[135]. The last two types of coherent CL (TR and plasmon generation) are the most common processes when an electron bombards the metal surface.

Transition radiation is an aftereffect observed when charged particles (protons, electrons, etc.) pass through the interface between different dielectric media. The media near the interface get polarised by the moving charge, creating surface currents and charges that radiate to the far field. Another description for TR is that when a fast-charged particle approaches a metal surface, it forms an image charge, and *the sudden annihilation of its image acts like an induced dipole that produces radiation[121]*. It has a broad spectrum extending from microwave to X-ray frequencies. Since the TR resembles a time-varying dipole radiating into the far field, it has a toroidal emission pattern (Figure 2.7a). The highly localised excitations of electrons can also generate surface plasmon polaritons at the metal interface. These can scatter off to the far field in the presence of coupling structures or from the edges of materials[132, 136]. When an electron beam hits the surface of a material such as gold, it creates perturbations in the density of conduction electrons, and the effective dipole oscillation is the source of CL. The dipoles can decay by emitting into the far field as TR or by exciting surface plasmons[137, 138]. The emission spectrum from a flat gold surface when a 10 kV electron beam is bombarded onto it is given in Figure 2.16a.

Incoherent CL is dominant in semiconductor materials and is similar to photoluminescence except that it uses electrons instead of light to induce electronic excitation[139]. Having large momentum and being a supercontinuum source of evanescent light, electrons can excite multiple transitions simultaneously. In contrast to coherent CL, incoherent CL is spontaneous and without a fixed phase relation between the incoming electron's field and the photons generated field[125]. Incoherent CL emissions cannot produce interference with coherent CL[121]. The emission probability can be significantly higher in this case, as high-energy electron can have a large interaction volume and thus multiple paths for electron-hole radiative recombination. This emission from incoherent CL follows a Lambertian distribution rather than a dipole-like distribution (as in TR) when an electron bombards the surface (Figure 2.7b). Compared to coherent CL, incoherent CL is unpolarised [121, 140].

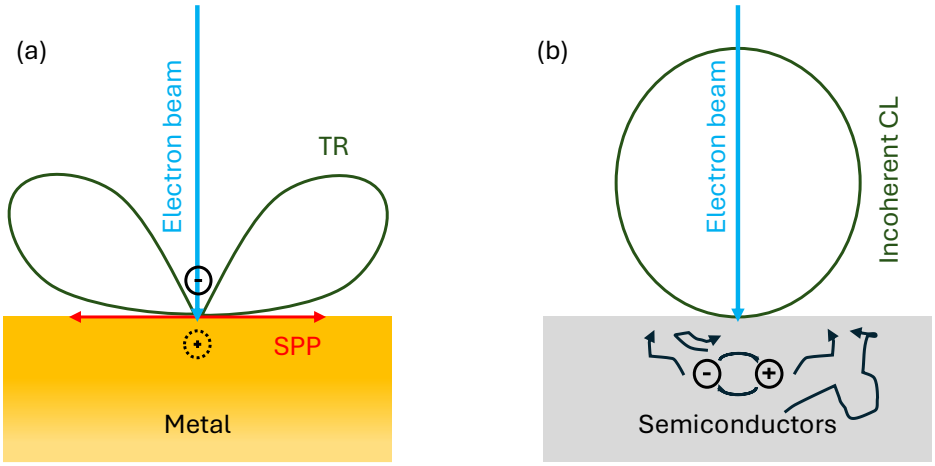

Figure 2.7: ***Coherent and incoherent CL emission patterns for a normal incidence of an electron beam****.(a) A cylindrically symmetric toroidal pattern of transition radiation (TR) emitted from a metal plate. Here, the image charge and the electron act as a dipole to produce the TR, and the incoming electrons also generate surface plasmon polaritons (SPP) that propagate along the surface of the material. (b) Incoherent emission from a semiconductor material has a Lambertian emission distribution. The electron-hole recombination emits light randomly inside the bulk of the material. Images were adapted and modified from[140].*

If an electron beam is scanned across the edge of a structure onto a flat metallic surface, the nature of the photon yield at each point of electron impact will be as shown in Figure 2.8. As the electron beam approaches the edge, we can see light due to diffraction radiation, even before the electron beam impacts on the material. This could be visualised as how a sea waves from a boat hit and scatter off a coastal wall. As the boat gets closer, the splash will be more. Similarly, photon emission increases until the electron physically collides with the material. When the electron beam is at the edge of the metal, the interaction volume is truncated and asymmetrically confined. A significant fraction of the electron energy is therefore deposited very close to the surface rather than spread into the bulk in a symmetric teardrop-shaped interaction volume (the

case when the electron beam falls on the surface). Since at the edge the material suddenly ends, the electrons in the metal cannot move beyond that boundary. This sudden “stop” forces the charges to oscillate more strongly in the confined space, which increases the local electric field and create a hotspot for plasmons that radiates into far field as light. From the moment the electrons hit the material, both surface plasmon polaritons (SPP) and transition radiations are generated. The SPP will scatter off the edge of the structure into the far-field as light, and this process continues until the electron beam is moved a few 100s of nm onto the structure[132]. After this, transition radiation dominates. This is why we observe a photon yield peak near the edge of the structure. When the electron beam irradiates a point on the surface of the material, the CL emission is not just from that point, but from a finite interaction volume around where the electrons enter the material. High-energy energy electrons penetrate the material and scatter both elastically and inelastically. The inelastic scattering will excite electrons, plasmons, or electron-hole pairs in the interaction volume. The depth and volume of the interaction region increase with high beam current, low material density and geometry. For metals like gold the surface plasmon can propagate and scatter off to far field from edges, corners or surface roughness few 100s of nanometres away from the point of origin. Along with the other CL emission process like the transition radiation the total CL signal what is detected is the CL signal averaged over the entire geometry. For an ideal rectangular geometric cross section (like the nanomechanical resonator cross section used in this thesis), we expect a symmetric CL emission yield as a function of electron beam impact location on its opposite side. For concept purposes, the emission yield from one side is shown in Figure 2.8.

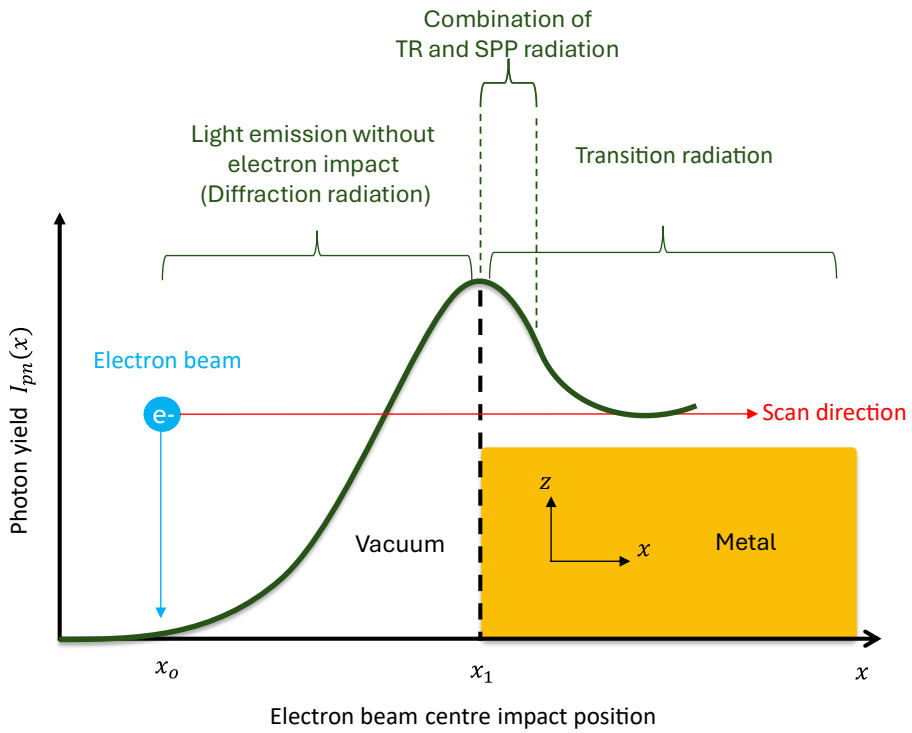

*Figure 2.8**: Expected photon yield as a function of electron beam impact position near the edge of a metallic structure kept in a vacuum.** Three regions of the emission process can be seen. The diffraction radiation due to the evanescent field of the approaching electron beam is seen until it nears the edge of the structure. When it is on the edge, transition radiation starts along with surface plasmons that scatter off the edge and couple to far-field emission. The combination of both surface plasmon polaritons scattering off the edge and transition radiations produces photons from the edge towards the middle of the material. TR dominates for electron beam impact further from edges and other scattering features, as the SPPs die out before they could be scattered. A peak in the emission rate around the edge of the structure is due to the combined contributions of all these emissions.*

If the structure displaces, and a fluctuation in this photon yield should be observed, it means that the information about the displacement is contained in the photon rate change. This can be developed to study motions of nanomechanical structures using electron-induced light emission.

2.6 Noise equivalent displacement at unitary SNR

An important aspect of this thesis is to investigate the cathodoluminescence-based noise equivalent displacement in nanomechanical systems. An analytical expression for estimating the noise equivalent displacement at a unitary signal-to-noise ratio (SNR) is derived. Figure 2.9 shows an illustration of the total photon yield ($I_{pn}(x)$) at each position as an electron beam makes a line scan across the edge (x_1) of a structure. The line scan can be performed in two ways; moving the electron beam relative to the fixed structure or moving the structure relative to a fixed electron

beam position x_o. Either approach will yield the same results. First, the former method is used to evaluate the total photon yield as a function of electron beam impact position, as shown in Figure 2.8. Due to the combined contributions from diffraction radiation, surface plasmon polaritons, and transition radiation (explained in Section 2.5.1), a peak in CL photon yield is seen at the edge of the structure when the electron beam crosses it. After that, the electron beam is fixed at a position (x_o) and the edge of the structure is displaced by a small amount 'a' in either direction relative to its initial position x_1 (Figure 2.9). When the edge of the structure displaces to the left, the electron beam is closer to the structure, and when the edge of the structure displaces in the opposite direction, the electron beam is further away from the structure.

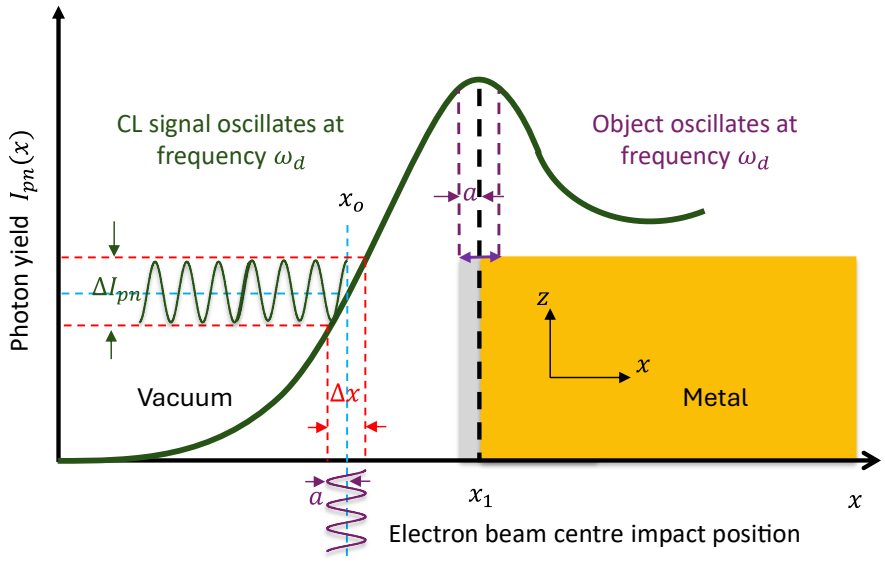

Figure 2.9: ***Illustration of the concept of detecting nanomotion by the detection of electron-induced photon emission.*** *CL photon yield ($I_{pn}(x)$) as a function of impact position from some distance away from the edge of the structure, across the edge of the structure x_1 (black dashed line) is shown. The structure oscillates with the edge displaced by a small amount 'a' back and forth about x_1. When the electron beam is kept at x_0, the slight change in the structure's edge position is equivalent to a slight change in the electron beam position Δx. This small change causes a change in the photon yield (ΔI_{pn}). The continuous oscillation of the structure at a frequency ω_d (purple wave with the amplitude corresponding to the displacement) yields a corresponding change in photon yield (green wave) at the same ω_d frequency.*

It is the same as saying that there is a slight change in the position of an electron beam about x_0, (Δx), which is equivalent to the slight change in the position of the edge of the structure about x_1. This small change (Δx) would result in a change in the total CL photon yield detected (ΔI_{pn}) around x_o. This change in the CL photon yield per small change in position i.e., $\Delta I_{pn}/\Delta x$ (slope of the curve) is the gradient of CL photon yield (∇I_{pn}) at x_o. The change in the number of photons detected in a time interval τ due to displacement of the structure by an infinitesimal distance 'a' is,

$$\Delta N_{CL} = a * (\Delta I_{pn}/\Delta x) * \tau \quad 2.25$$

In practice, the CL photon count variation can be detected by a photodetector and generate a variation in photon current or voltage that corresponds to the displacement of the structure. This is demonstrated in Chapter 3.

In the case of using secondary electrons for nanomotion detection[5], the noise equivalent displacement (NED) level in SEM is determined by the Poisson statistics of electrons incident on the secondary electron (SE) detector. The standard deviation of shot noise is $\sqrt{N_{SE}} = \sqrt{(I_{SE}/e)\tau}$ where N_{SE} is the total number of secondary electrons detected in the time interval τ, I_{SE} is the secondary electron current, and e is the charge of an electron. The total number of electrons per unit time in a given SE current is I_{SE}/e.

Following the same convention in the CL case, the NED level can be determined by the Poisson statistics of photons detected on the photodetector. The standard deviation of shot noise then would be $\sqrt{N_{CL}} = \sqrt{I_{pn}(x)\tau}$, where N_{CL} is the total number of CL photons detected by a photodetector, and here, instead of SE current (I_{SE}), the CL photon yield $I_{pn}(x)$ is considered. Substituting Equation 2.25 and rearranging for the noise equivalent detectable displacement a for unitary signal-to-noise ratio ($\Delta N_{CL}/\sqrt{N_{CL}}$ =1),

$$a = \frac{\Delta x}{\Delta I_{pn}} \sqrt{\frac{I_{pn}(x)}{\tau}} \quad 2.26$$

$$a\sqrt{\tau} = \frac{\Delta x}{\Delta I_{pn}} \sqrt{I_{pn}(x)} \quad 2.27$$

Equation 2.26 tells that the displacement that can be detected is equal to the inverse of the product of the CL photon yield gradient ($\frac{\Delta x}{\Delta I_{pn}}$) and the square root of the total photon yield per integration time. Photon yield and integration time are independent; hence, Equation 2.26 can be rewritten as Equation 2.27. Since the gradient is proportional to the photon yield, if the electron current is doubled, the gradient and the photon yield will also be doubled. This makes the benefit from the higher gradient bigger than the penalty from the higher photon yield. Therefore, at a position x_0 with a higher CL photon yield gradient, and a higher CL photon yield (as it makes the gradient bigger) would result in a smaller minimum detectable displacement with unitary signal to noise ratio.

2.7 CL emission probability as a function of electron beam position and electron beam diameter

To study the CL generated from an object of interest inside a SEM, an analytical formula for the CL emission probability as a function of electron beam position (x_o) and beam diameter (D) was to be derived. A one-dimensional cross-section of a structure with an arbitrarily shaped edge located at x = 0, represented by $f(x)$, is considered in Figure 2.10. The electron beam is assumed to be a cylindrically symmetric Gaussian beam, $G(x, y)$, at a position x_o with the full width half maxima (FWHM) considered as the diameter.

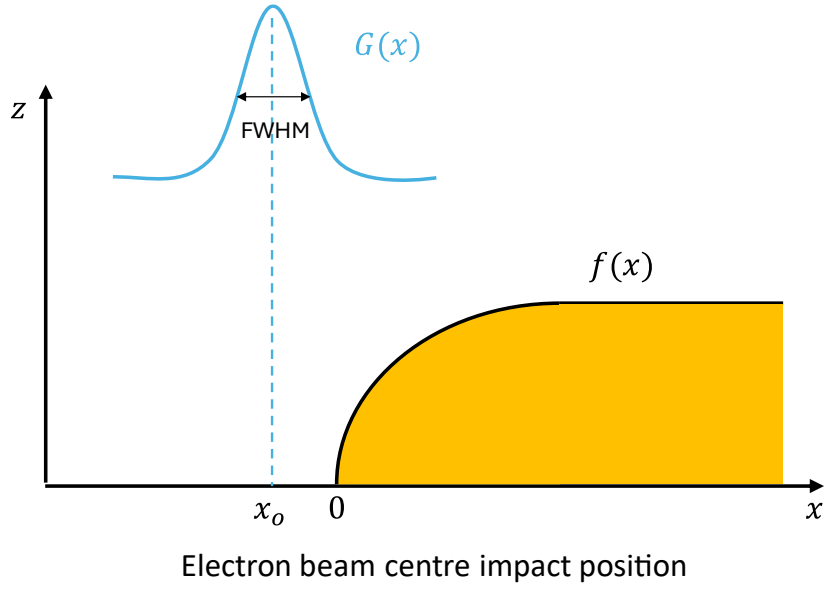

Figure 2.10: ***Electron beam near an arbitrary edge****. An $x - z$ cross-section of a structure with an arbitrary-shaped edge ($f(x)$) is considered. A one-dimensional Gaussian electron beam, $G(x)$, with FWHM, as the diameter (D) of the electron beam, is kept at a position x_o.*

The probability distribution of finding an electron at coordinates x, y,

$$G(x,y) = \frac{1}{2\pi\sigma_e^2} exp\left(-\left(\frac{(x-x_o)^2}{2\sigma_{e_x}^2} + \frac{(y-y_o)^2}{2\sigma_{e_y}^2}\right)\right) \qquad 2.28$$

Being cylindrically symmetric, the standard deviation, $\sigma_{e_x} = \sigma_{e_y} = \sigma_e$. The FWHM and standard deviation are connected as, $\sigma_e = \mathrm{FWHM}/2.355 = \mathrm{D}/2.355$.

The probability that an electron will fall on the surface (P_e) will be the integration of $G(x, y)$ over the surface area of the structure.

$$P_e = \iint G(x,y)dxdy \\ = \int_{-\infty}^{\infty}\int_{0}^{\infty} \frac{1}{2\pi\sigma_e^2} exp\left(-\left(\frac{(x-x_o)^2}{2\sigma_e^2} + \frac{(y-y_o)^2}{2\sigma_e^2}\right)\right)dxdy \quad 2.29$$

Assuming translational symmetry along the y-axis, Equation 2.29 reduces to a one-dimensional case,

$$P_e = \frac{1}{\sqrt{2\pi}\sigma_e}\int_{0}^{\infty} exp\left(-\frac{(x-x_o)^2}{2\sigma_e^2}\right)dx \quad 2.30$$

Where the probability distribution of finding an electron in the x direction is,

$$p_e = \frac{1}{\sqrt{2\pi}\sigma_e} exp\left(-\frac{(x-x_o)^2}{2\sigma_e^2}\right) \quad 2.31$$

The photons are generated even before the electrons hit the structure. A factor $\Gamma_{CL}(x)$ is introduced, which determines the CL emission probability per electron impact at a given position. This factor depends on many other parameters such as the material properties ($\varepsilon(\omega)$), the evanescent field associated with the electron (function of acceleration voltage), the geometry of the structure ($f(x)$), the slope of the structure($f'(x)$), solid angle of emission (Ω), and photon frequency range (ω). Formulating a general equation would be difficult.

In[121], the author introduces a multivariable function that gives the number of photons emitted per incoming electron as a function of solid angle of emission, and photon frequency range ω for coherent CL emission,

$$\gamma_{CL}(\Omega,\omega) = \frac{1}{4\pi^2\hbar\, k_\omega}|\boldsymbol{F}(\Omega)|^2 \quad 2.32$$

Where $\boldsymbol{F}$ is the far-field amplitude expressed in terms of boundary currents on the interface of the structure's material near the vacuum side, k_ω is the free-space light wave vector ($k_\omega = \omega/c$), and $\hbar$ is the reduced Planck's constant. $\gamma_{CL}(\Omega,\omega)$ can take different forms based on different CL emission processes[121] and incorporate all the parameters that affect photon emission. For plasmonic materials (like gold), this can be evaluated numerically.

$\Gamma_{CL}(x)$, considered in the following derivation is an integral of Equation 2.32 with respect to the photon frequency range and the solid angle. Therefore, the CL emission probability as a function of electron beam position and electron beam diameter takes a general form,

$$P_{CL}(x_o, \sigma_e) = \frac{1}{\sqrt{2\pi}\sigma_e}\int_{-\infty}^{\infty} \Gamma_{CL}(x) * exp\left(-\frac{(x-x_o)^2}{2\sigma_e^2}\right)dx \quad 2.33$$

A direct analytical formula for $\Gamma_{CL}(x)$ is difficult, so a numerical approach has been adopted.

2.8 Numerical simulations of cathodoluminescence

Metallic nanoparticle boundary element method (MNPBEM17) is a MATLAB toolkit developed by Ulrich Hohenester[141] utilising the boundary element method (BEM) to solve Maxwell's equations for a dielectric environment where abrupt interfaces separate geometries with homogeneous and isotropic dielectric functions. The BEM derives the CL radiation spectrum from the surface charges and currents calculated using Green's function developed by F.J.G. Abajo[121]. It has been widely used in the electron optics community for studying electron energy loss spectroscopy (EELS) and CL[130]. A single electron, described as a point charge, is considered in the simulation as it moves in a vacuum with a specified acceleration voltage and impact position. This makes the simulation results devoid of the electron beam diameter. The results are calculated for the full 4π collection range by default. Though the simulation tool provides the freedom of choosing any size of the metallic structure, the computational time limits the material dimensions in practice. The dielectric model (Drude model) of the materials is used[142, 143].

A square block with sharp edges, a side length of 300 nm, and a thickness of 50 nm was considered for the study. Gold, as described by the Drude model[143], was chosen as the material. The electron trajectory was set at a point 100 nm away from the edge of the structure with an acceleration voltage of 10 kV. It was programmed to scan across the structure with a step size of 1 nm, through the centre to 100 nm away from the other edge (illustrated in the inset of Figure 2.11). At each impact position (x_o), the CL emission probability was evaluated for the photon energy (wavelength) range of 1.24 eV (1000 nm) to 6.19 eV (200 nm). This photon energy (wavelength) range is chosen to match the spectral range of the available spectrometer (Figure 2.16a). The spectrum at each impact position is integrated with respect to the photon energy range and the CL emission probability as a function of the impact position $\Gamma_{CL}(x)$ is plotted in Figure 2.11.

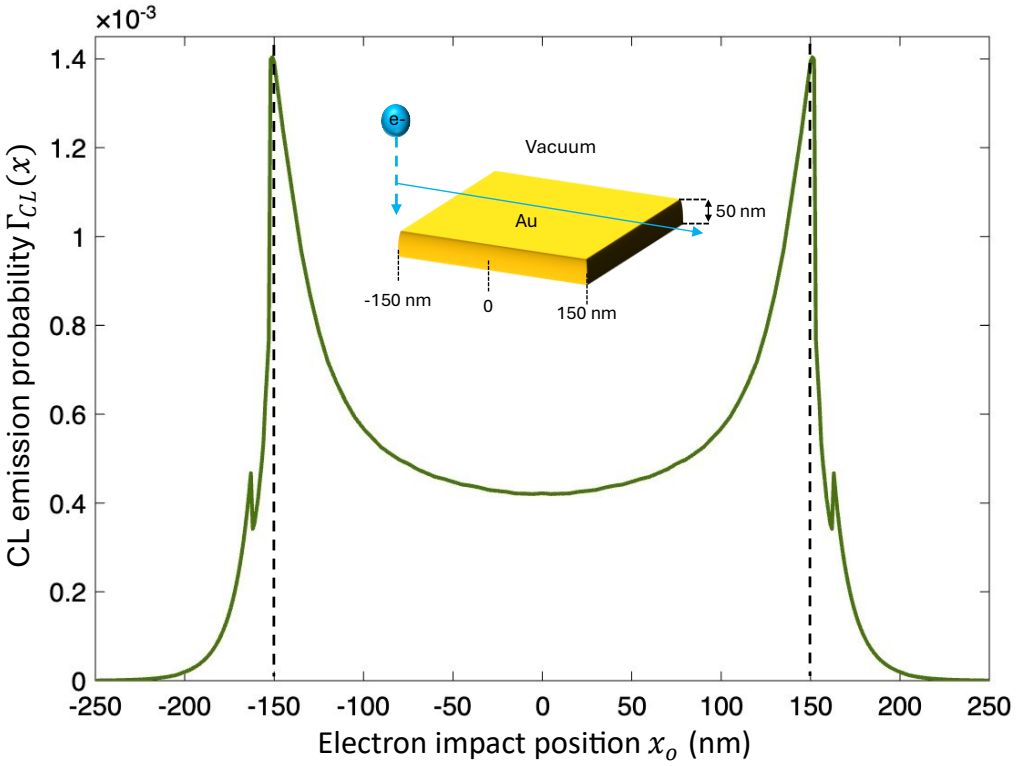

Figure 2.11: ***CL emission probability per electron as a function of impact position.*** *An illustration of electron impact during a line scan on a* 300 * 300 * 50 nm *gold (Au) structure in vacuum. The spectrum from each impact position (Figure 2.16b shows an emission spectrum from the middle of the structure) is integrated with respect to the photon energy (wavelength) range from* 1.24 eV (1000 nm) to 6.19 eV (200 nm) *to calculate the CL emission probability per electron as a function of impact position. The black dashed lines represent the edges of the structure.*

From Figure 2.11, we can see that the probability of photon emission becomes significant when the electron passes near the structure as it strongly excites edge plasmons. Far away the electron barely 'feels' the gold and very little CL photons are expected mostly due to evanescent field decay. Just near the edge ($\pm$162), a dip in CL emission probability is observed (also observed in Figure 2.14a). This is assumed to be arising because electron at that position can excite both the edge localized mode (radiating) and interior slab modes (poorly radiating and could be lost as heat). These could destructively interfere and the measured CL emission probability could drop briefly. The probability of photon emission in coherent CL is typically of the order 10^{-4} photons/electron[121, 125], which is comparable to the simulation results. This means that the light emission from plasmonic materials is poor, and to obtain a good emission, a high electron beam current should be used. The $\Gamma_{CL}(x)$ obtained from the simulation has data points spaced by 1 nm. Following Equation 2.33, $\Gamma_{CL}(x)$ was multiplied with a Gaussian electron distribution with a diameter (FWHM) and integrated to evaluate $P_{CL}(x_o, \sigma_e)$. The inset of Figure 2.12 shows electron distributions for Gaussian beams with different diameters, and Figure 2.12

shows how $P_{CL}(x_o, \sigma_e)$ varies for different electron beam diameters at an acceleration voltage of 10 kV.

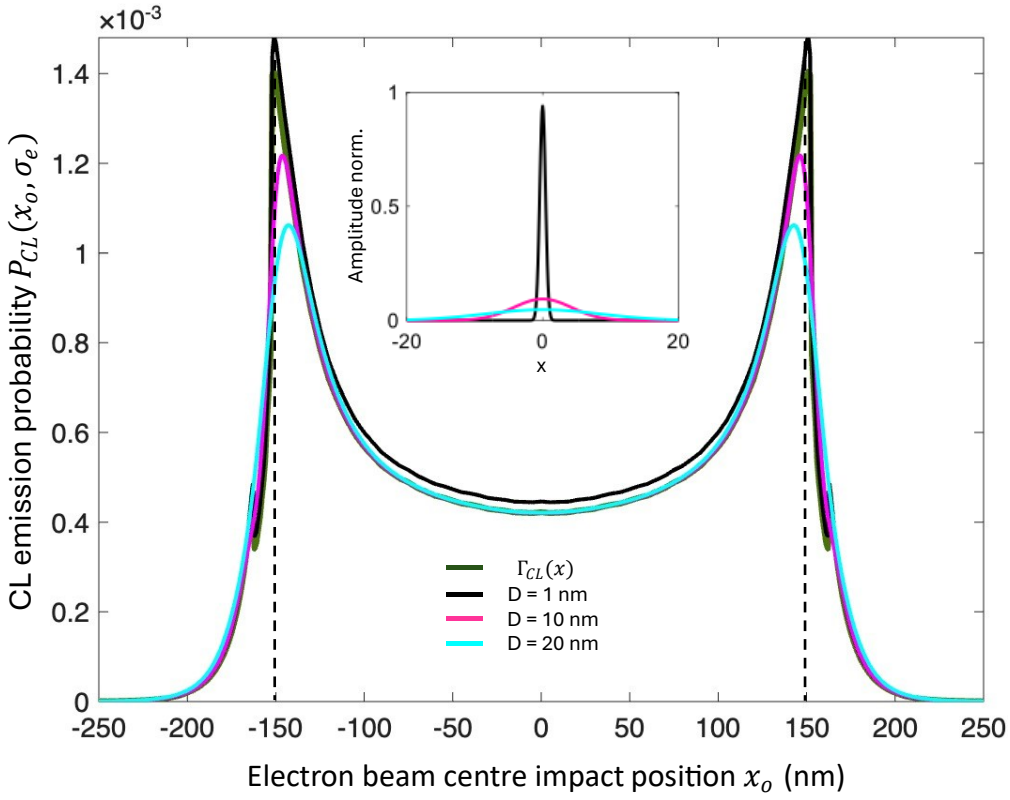

Figure 2.12: ***CL photon emission probability per electron as a function of impact position for different electron beam diameters,*** $P_{CL}(x_o, \sigma_e)$ *compared with* $\Gamma_{CL}(x)$ *evaluated for the nanostructure of Figure 2.11 at* 10 kV. *A normal distribution of Gaussian beams (representing electron beams) with different diameters* (D) *with a mean position at zero is shown in the inset. The black dashed lines represent the edges of the structure.*

As illustrated in Figure 2.12, there is a shift in the CL peak positions from the edges towards the centre of the nanostructure as the electron beam size increases. The photon emission probability broadens, and the magnitude of the peak also decreases. The tail part also widens as the beam size increases. This can also be expected in the real experiment. When the beam current is increased, the electron beam's spot size increases, resulting in the peak being seen away from the edge of the structure. An electron beam of 1 nm diameter does not make much difference compared to the $\Gamma_{CL}(x)$ values, except that the top of the peak is smoothed. Further calculations are based on this plot.

An experimental test (Section 2.9) was performed using a high beam current of 18 nA, due to the low emission probability of plasmonic materials. This beam current corresponds to 11.2 *10^{10} electrons per second and was multiplied with $P_{CL}(x_o, \sigma_e)$ to predict the total CL photon yield, $I_{pn}(x)$, at each electron beam centre impact position. A typical SEM beam current (fraction of a

nA to a few nA) corresponds to an order to magnitude of 10^9 electrons per second, which would result in 10^5 photons/electrons /second.

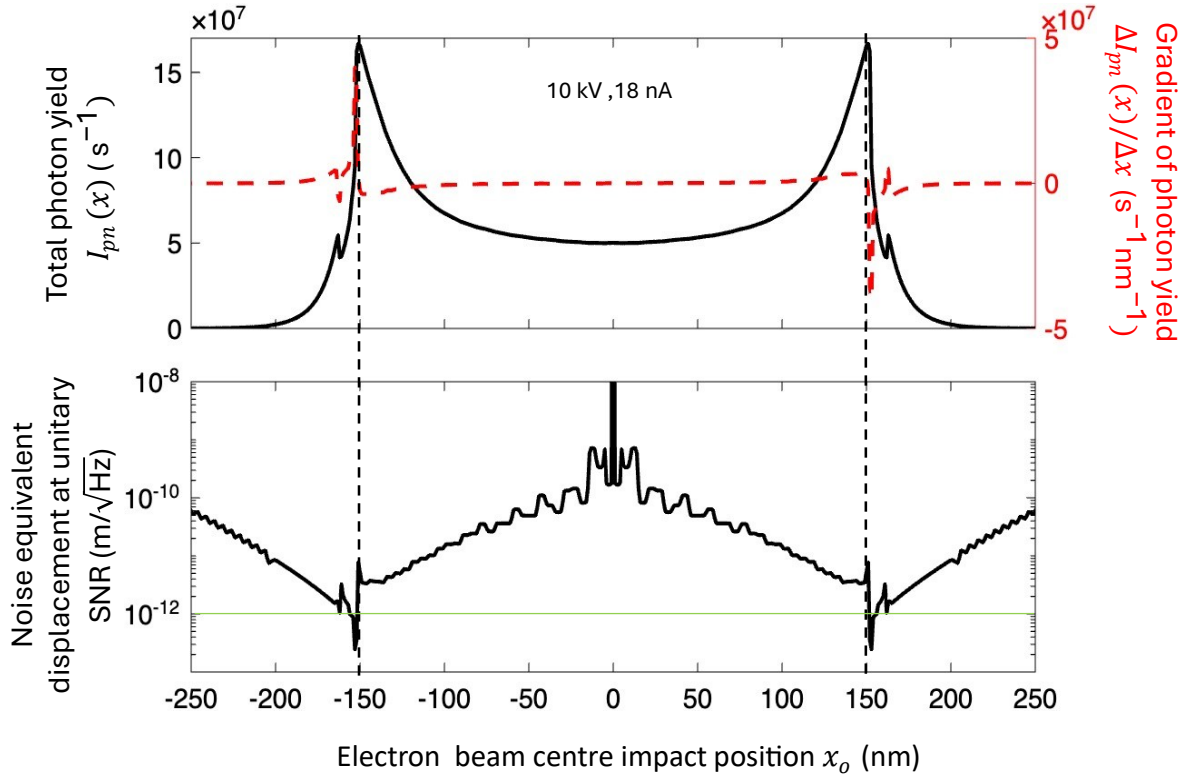

Figure 2.13: ***Estimating noise equivalent displacement.****(a) The black solid curve (red dashed curve) represents the total photon yield (gradient of photon yield) as a function of impact position for a* 10 kV,18 nA *electron beam incident on the plasmonic nanostructure of Figure 2.11. (b) Corresponding noise equivalent displacement at unitary SNR as a function of impact position. The edges of the structure are marked with a black dashed line. The green horizontal line corresponds to* 1 pm/√Hz.

Figure 2.13a shows the total photon yield ($I_{pn}(x)$) and the corresponding gradient as a function of impact position. The calculation assumes 18 nA beam current and 10 kV acceleration voltage. Plugging the values in Equation 2.26, the noise equivalent displacement at unitary signal-to-noise ratio is evaluated as a function of electron beam centre impact position (Figure 2.13b). The minimum value of displacement is observed at the position with the maximum gradient. The CL photon yield gradient at the centre is zero, which makes the detectable displacement at the centre of the particle go to infinity. It means that placing an electron beam at the centre does not help in detecting any variation of the structure's position, as there is no variation in the CL photon yield. At the particle's edge, the gradient also crosses zero, resulting in a spike in the detectable displacement (because of limited resolution in computing, the sharp spike is not seen at the edge). From the edge towards the centre of the particle, the photon yield is reducing, and the gradient is approaching zero. This causes an increase in the detectable displacement, and the

step size of the simulation results in a wavy of the curve. The sharp peaks near the centre are due to the proximity of the gradient to zero. Towards the tail ends, the photon yield and corresponding gradient approach zero. The detectable displacement values rise because there is only a small probability of photon emission (very close to zero).

Following the same approach, the total photon yield and noise equivalent displacement at unitary signal-to-noise ratio as a function of impact position for different acceleration voltages (10 kV to 20 kV in a step size of 5 kV) are calculated and shown in Figures 2.14a and b, respectively. To have a clear understanding of the detected displacement, the displacement values from the particle's edge (x_0 =150 nm) and from the point where the gradient is maximum (x_o =153 nm) are plotted against the acceleration voltages in Figure 2.14c.

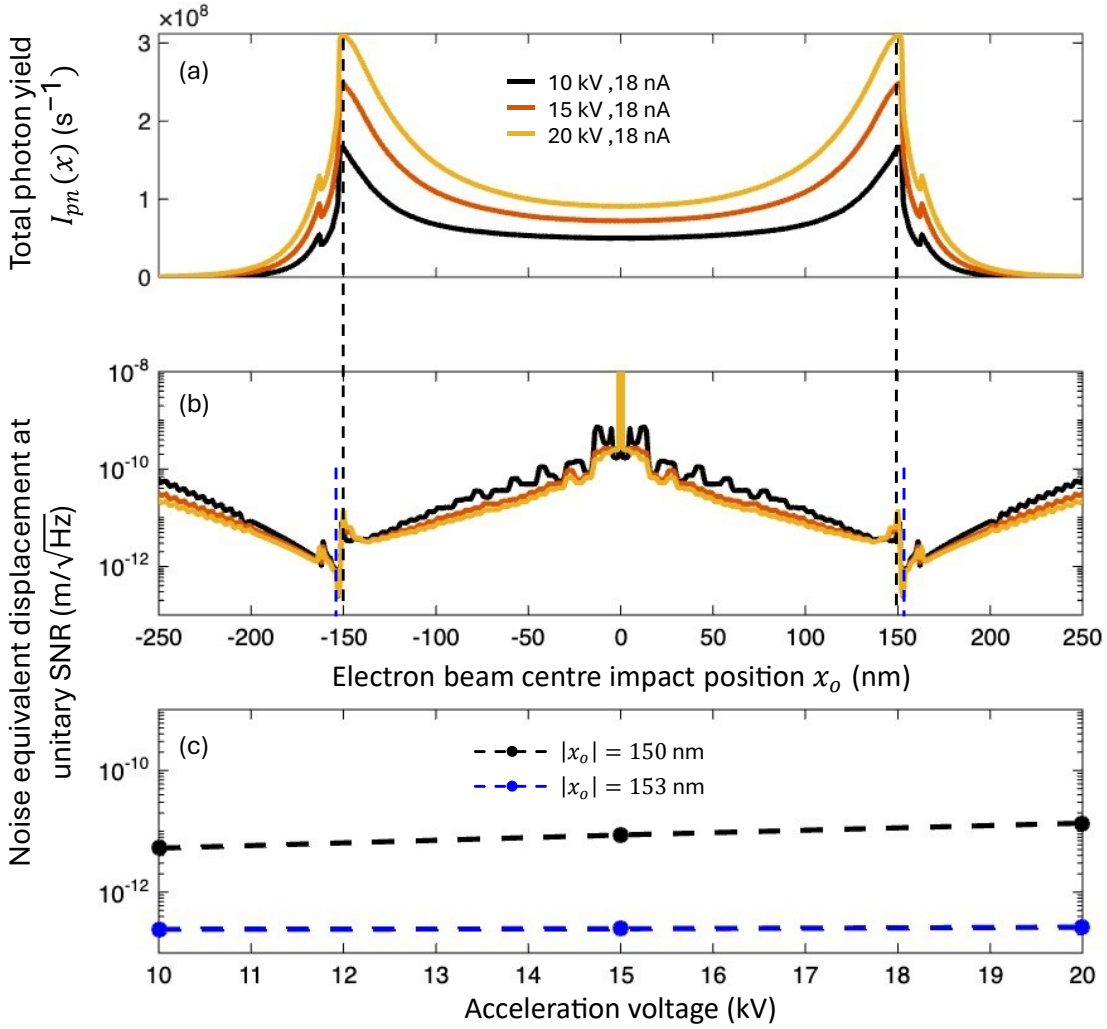

Figure 2.14: ***Noise equivalent displacement at unitary SNR for different acceleration voltages.*** *(a) Total CL photon yield for acceleration voltages from* 10 kV *to* 20 kV *in a step of* 5 kV. *(b) Corresponding noise equivalent displacement for unitary SNR. The black dashed line represents the edges of the structure. (c) Noise equivalent displacement for unitary SNR values from the edge (*x_o = 150 nm*) and at the position of maximum gradient (*x_o = 153 nm*) are plotted as a function of the acceleration voltage.*

The simulation results provide a promising noise equivalent displacement amplitude spectral density of ≤ 1 pm/$\sqrt{\text{Hz}}$ at a position, a few nm away from the edge of the structure. This demonstrates that sub-nanometre motion detection using cathodoluminescence is feasible.

2.9 Cathodoluminescence measurements on gold nanostructures

To verify if we could achieve a comparable level of noise equivalent displacement, a test was conducted by scanning the electron beam across an edge of a 50 nm silicon nitride membrane with 50 nm gold thermally coated on top of it. A focused ion beam (FIB) dual beam system was used to cut a small square area on the free-standing Au/Si_3N_4 membrane. The experiment is conducted using an SEM and a UV-visible spectrometer (Horiba). An illustration of the preliminary experimental setup is shown in Figure 2.15.

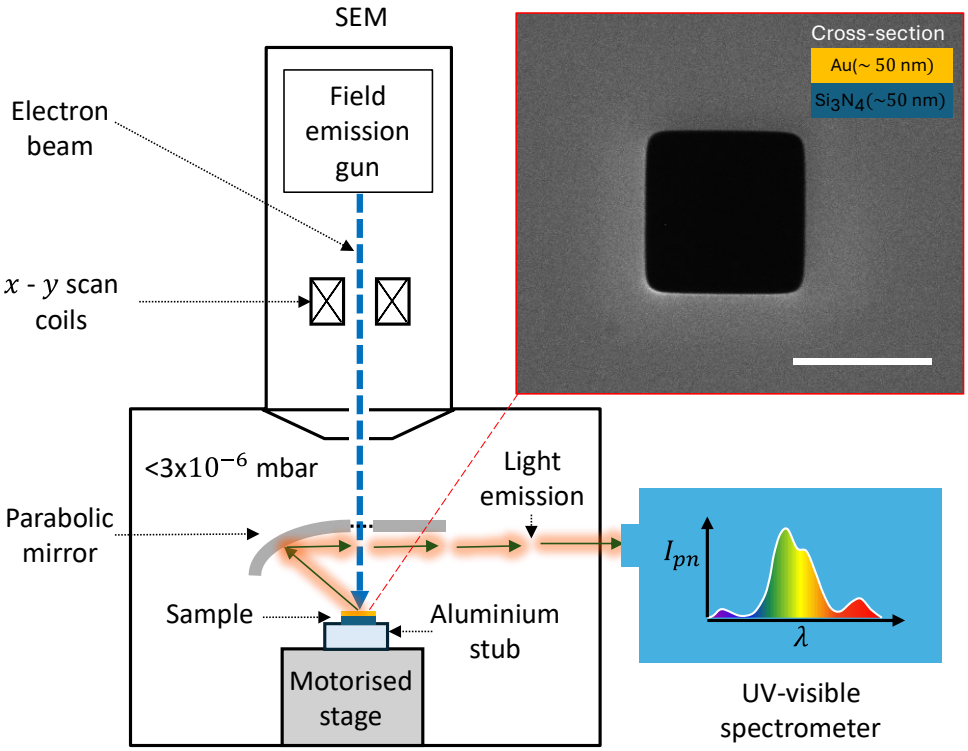

Figure 2.15: ***Illustration of the initial experimental setup.*** *A modified SEM with a light-collecting parabolic mirror is shown. The CL emission process happens inside the SEM chamber, where the sample is irradiated by the electron beam and kept at the focus of a parabolic mirror to enable CL collection. The light generated is reflected off the parabolic mirror and channelled outside into a UV-Visible spectrometer. The sample used for the test is shown. The inset shows the material's cross-section. The scale bar is* 500 nm *long.*

The sample is mounted on an aluminium stub and loaded inside the SEM chamber. The height of the stage is adjusted to keep the sample at the focus of the parabolic mirror. The acceleration

voltage was initially set to 10 kV, and the beam current used was 18 nA. The poor CL emission yield of plasmonic materials, as discussed in Section 2.5.1, was the reason to use a high beam current. The choice of selecting 18 nA as the beam current was arbitrary; it was simply the maximum current the SEM could provide during the test. The parabolic mirror position was optimised by maximising the spectral output using the spectrometer. For the optimization, a flat portion of gold on the sample was selected (inset of Figure 2.16) by adjusting the SEM stage position. The CL emission generated from the flat surface of the gold sample is reflected off the parabolic mirror. This light travels outside of the SEM through a beam tube and into the spectrometer. The light is resolved as photon counts per wavelength bin per second. The pitch and yaw of the parabolic mirror, and the stage height, are adjusted until the spectrum is maximised. The emission spectrum after optimisation is shown in Figure 2.16a. The spectrum shows a dominant peak around 517 nm wavelength, which is close to the surface plasmon resonance of gold[138, 142, 144]. The simulation results (Figure 2.16 b) show a peak at 519 nm, which is close to what we observed in the experiment. The simulation spectrum is taken from the centre of the Au nanoparticle and normalised. All experimental peaks can be identified within the gold-only simulation. The Si_3N_4 substrate was not considered for the simulation.

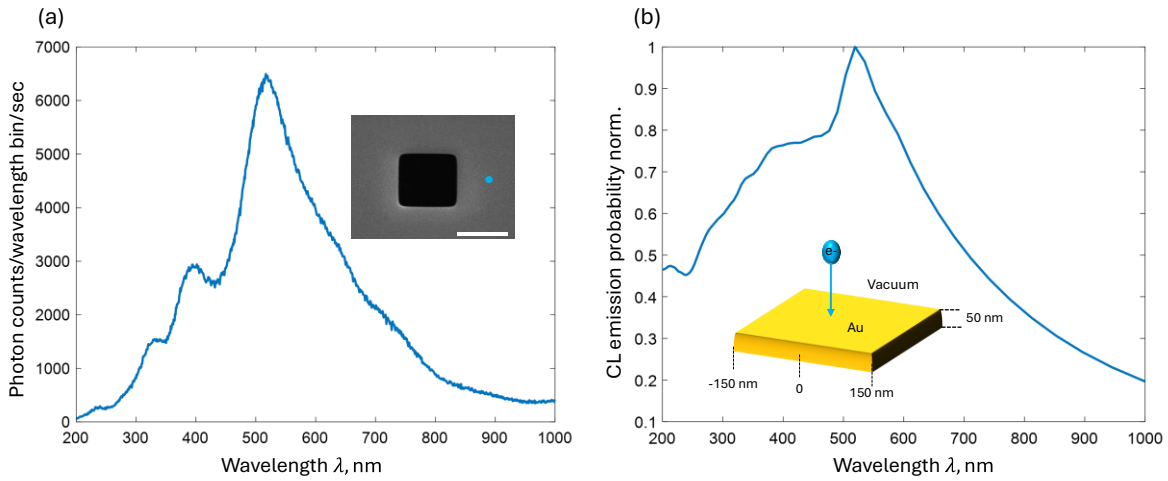

Figure 2.16: ***CL emission spectrum from a flat gold surface for an incident*** 10 kV,18 nA ***electron beam****.(a) The inset shows the position of the sample used to take the CL spectrum (blue dot). (b) Normalised CL probability from MNPBEM simulation. The spectrum is obtained from the centre of a* 300 nm * 300 nm * 50 nm *Au nanoparticle (inset).*

An important aspect of this project is to determine the extent of displacement that could be measured by the method proposed in Section 2.7. The experiment begins by looking into the photon yield at each impact position of the electron beam during a line scan. The edge of the cut was chosen for this. The selected portion was zoomed in to a level where a line scan can be performed (inset of Figure 2.17 b) using the spot mode of the SEM. When spot mode is activated,

the SEM captures and freezes an image of the set position. A spot-by-spot movement of the electron beam is then possible. The spot is set at one end and manually moved with a step of 7.4 nm throughout the line scan. At each impact position, the emission spectrum is recorded using the spectrometer. A single spectrum took around 20 to 25 seconds to measure, and a single line scan took about half an hour. Sample drift was observed due to prolong exposure to high beam current. Such high beam current can result in thermal expansion of the sample, stub or the stage to cause small movements. Other factors such as local charging of the sample by high beam current exposure and not so perfect grounding, the floor vibrations, vibrations from the vacuum pump placed next to the SEM or the instability of the old sample stage inside the SEM chamber could have also contributed to the sample drift. The edge shifted frequently and had to be readjusted. The edge of the cut was aligned with the central line of the grid lines (option available in the SEM software) overlayed on the image. After each measurement the alignment is readjusted. The same procedure has been used throughout the thesis to rectify drift. The beam current did not remain constant; instead, it fluctuated, and sometimes it dropped. After taking each spectrum, the changes were compensated for. The emission spectrum at each impact point is integrated with respect to the wavelength bin range, and the total photon yield per second is obtained. This process is repeated for all the spectra at different electron beam positions and plotted as a function of impact position for 10 kV and 15 kV acceleration voltage in Figure 2.17.

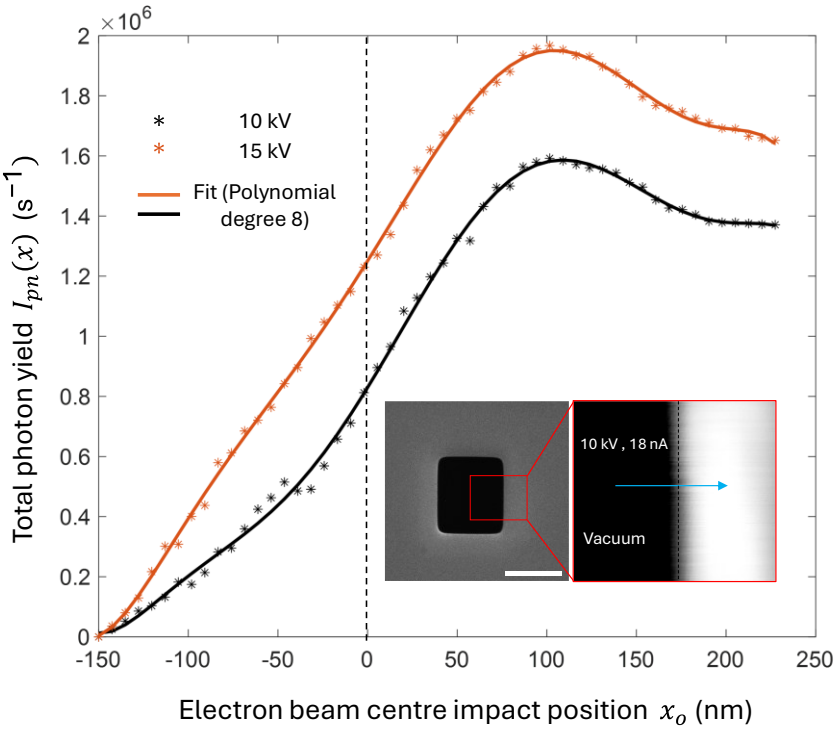

Figure 2.17: ***CL emission yield during line scan across a gold edge****. The CL photon emission yield is plotted as a function of impact position for an electron beam of* 10 kV and 15 kV *acceleration voltage with* 18 nA *beam current. The experimental data points are fitted with a polynomial of degree* 8 *(solid lines). The black dashed line denotes the edge of the cantilever. The inset shows the portion of the edge used for line scan. The scale bar is* 500 nm *long. The spot mode step size was* 7.4 nm.

Compared to the simulation, the experiment reports a total photon yield two orders of magnitude lower. There are several reasons for this: In the simulation, the photon yields are reported for the full 4π collection range. In the experiment, the parabolic mirror captures part of the light from above the sample, and it could be about one-fourth of the total photons emitted from the sample. The light reflected from the parabolic mirror would be roughly 1cm in diameter, and the completely open slit of the spectrometer is 2 mm wide. If the beam is centred on the slit, about one-fifth of the light could enter the spectrometer. Further losses due to grating efficiency and detection within the spectrometer could reduce the number of photons even more.

When an acceleration voltage of 15 kV or higher was used, sample drift became significant, making it difficult to take measurements at known positions relative to the sample edge. This may have been caused by charging and/or heating associated with the high current of energetic electrons. Going below 10 kV made the images noisy, making it difficult to identify the sample edge reliably. The image's contrast and brightness were too low and adjusting them did not improve the situation.

The experimental data showed that the photon yield is higher for a beam of higher-energy electrons, as predicted by the numerical simulation reported in Figure 2.14. Using a high acceleration voltage makes the electrons penetrate deeper and scatter over a larger volume (interaction volume). This makes more CL photons to emit from deeper and wider region hence it excites plasmons across more of the particle volume. In case of semiconductor materials (the ones used in Chapter 3, 4, and 5), the high energy electrons can excite more valence electrons into conduction bands and increase the number of radiative recombination hence more CL photons will be generated. The peak is seen shifted from the edge of the cut. This could be because a high beam current can increase the electron beam spot size. Another reason could be that the position considered here as the edge of the cut could not have been the edge. This is because the features become blurred from a zoomed-in portion of the cut while using a high beam current. The shift and broadening of the peak, observed when large beam spot sizes are used, were also noted in the numerical studies (Figure 2.12). This is one of the reasons that the photon counts are still observed even at a few hundred nanometers away from the edge. When the electron beam gets farther away from one edge of the cut, it gets closer to the opposite edge of the membrane, and hence, photons could be generated from there.

The data is subjected to human errors for a few reasons; the spot movement was manual, and frequent delays in adjusting the edge positions and beam current sometimes delay taking a spectrum. Keeping the electron beam at a position on the sample for too long will cause carbon deposition, which reduces the spectral output. The data were fitted with a polynomial of degree 8 so that the discrepancies in the data could be avoided. The gradient of the polynomial fit was taken to avoid experimental noise.

With the CL gradient evaluated, the noise equivalent displacement for a unitary signal-to-noise ratio was estimated using Equation 2.26 for 1 second integration time. The result is plotted as a function of electron beam impact position for 10 kV and 15 kV electron beams in Figure 2.18.

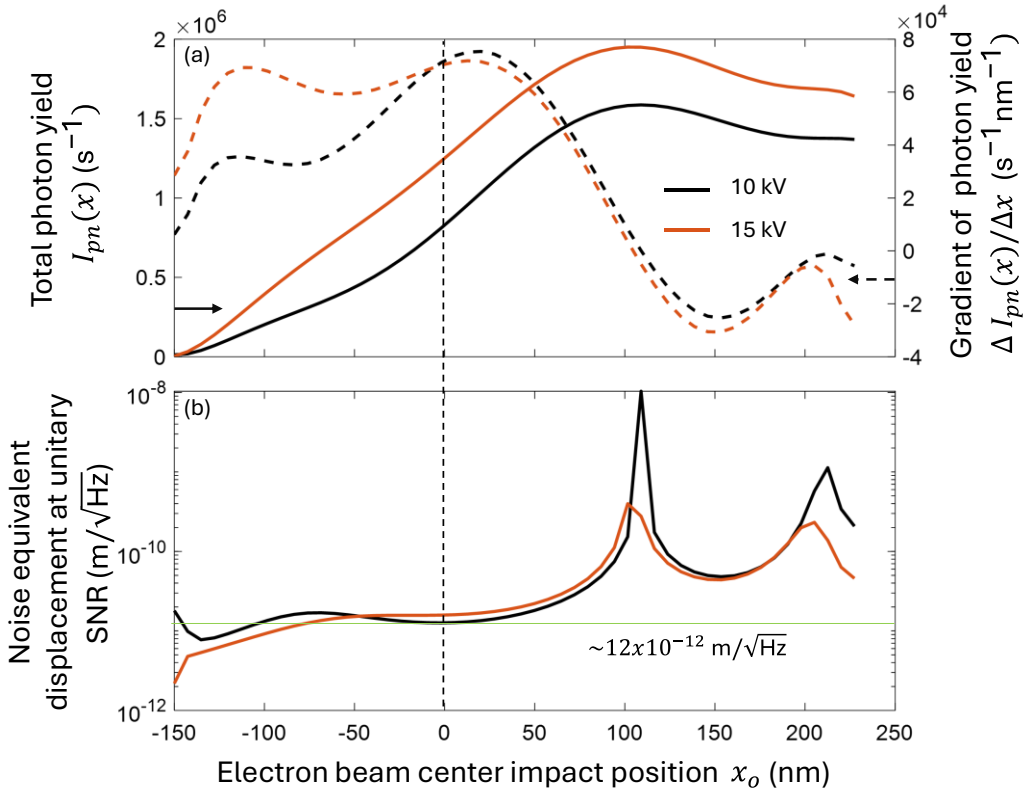

Figure 2.18: ***Experimental results for estimating the noise equivalent displacement at unitary SNR.*** *(a) Polynomial fit corresponding to the total photon yield (solid line) and its gradient (dashed line) as a function of impact position is plotted for* 10 kV *and* 15 kV *electron beams at* 18 nA. *(b) Based on the total photon yield and the gradient, the noise equivalent displacement for unitary SNR as a function of impact position is plotted. The black dashed line indicates the edge position of the cut, and the green horizontal line indicates* 12 pm/$\sqrt{\text{Hz}}$.

Similar to the simulation result presented in Figure 2.14a, b, at the edge of the cut, a 10 kV electron beam yields a smaller minimum detectable displacement than 15 kV. The results presented in Figure 2.18b are evaluated based on the gradient value from the polynomial fit. The best sensitivity is observed at the edge, where the gradient is high but not the highest. Both photon yield and gradient of photon yield matter, i.e., the optimal point is slightly shifted from the highest gradient towards a low photon yield. Sharp peaks are observed at positions where the gradient is near zero. Some distance away from the edge, there will be a photon contribution from the neighbouring gold-coated Si_3N_4 membrane; hence, only the results from near the edge of the cut were only considered to understand the method's practical efficiency. A noise equivalent displacement of ≥12 pm/$\sqrt{\text{Hz}}$ has been calculated at the edge of the cut for an 18 nA, 10 kV electron beam.

The cathodoluminescence measurements with the help of a spectrometer indicate a good displacement resolution. However, a spectrometer cannot resolve fast motion that happens in a

short interval of time (typical mechanical resonance frequencies of nanostructures vary from kHz to GHz). As discussed previously, similar to using SE current variation for displacement detection, the temporal variation in photocurrent (I_{CL}) from the photons detected by a photodetector could be used for displacement detection. The variation in secondary photon current ($\Delta I_{CL}\ (t)_{x_o}$) at a position x_0 in response to a displacement, Δx is,

$$\Delta I_{CL}(t)_{x_o} \approx \left(\frac{\partial I_{CL}(x)}{\partial x}\right)_{x_o} \times \Delta x(t) \qquad 2.34$$

This variation in photocurrent shall be observable as a peak at the nanostructure's vibrating frequency using a spectrum analyser.

2.10 Choosing the cathodoluminescence material

Though gold has been used for the initial evaluation, the poor photon yield of plasmonic materials (typically 10^{-4} photons/electron) can make establishing the technique of nanomechanical motion detection using CL difficult. Having a poor photon yield means that a higher beam current than the typical SEM operating beam current (a few hundred pA to a few nA) should be used to extract more photons from the sample. This is also necessary due to the nature of my experimental setup, i.e., the CL photons are collected using a parabolic mirror that only collects light from the top region, and the detectors are located outside the SEM chamber; this can lead to a loss of photons and a lack of focusing onto the detector. Using a high beam current comes with certain risks, such as compromising the sample integrity through electron-induced heating, carbon deposition, and charging. The samples used in this thesis are nanomechanical wires and cantilevers, so a high beam current can perturb the dynamics of the nanomechanical structure, bend the structure, and introduce significant drift. It will also reduce the SEM imaging resolution as the electron beam spot size increases with beam current, and knowing the exact location of the structure's edge is crucial for the experiment. It would be beneficial to use a material that emits more photons in response to interaction with fewer electrons.

To establish the method in my experimental setup, evaluating the signal-to-noise ratio (SNR) based on experimental data was a more suitable selection procedure for the material to be used than simulations. A test was conducted using a 50 nm gold film deposited on top of a 50 nm silicon nitride membrane, a Phosphor (ZnS:Ag) sample of a few micrometres thick, and a single-crystal gallium nitride (GaN) sample (a few micrometres thick) grown on sapphire. Figure 2.19 shows the CL emission spectra of the materials. All the samples were kept on the same substrate, and their emission spectra were evaluated using a spectrometer with all measurement conditions set to a 1 second exposure time, a 2 mm slit width, and a grating of 100 grooves/mm.

The beam currents were adjusted when each light spectrum saturated on the spectrometer, but the acceleration voltage was kept at 10 kV. While taking spectra from each sample, the height of the stage was slightly adjusted to maximise the spectrometer reading, thereby compensating for the slight thickness difference between the samples.

The characteristic peaks of gold, phosphor (ZnS:Ag), and GaN align with the respective coherent and Incoherent CL emission processes. From Figure 2.19, ZnS:Ag was the brightest sample of all three, and its total photon emission power was estimated using a power meter [ThorLabs PM160T], which was about 1.1nW/nA. This output power and the spectrum from the ZnS:Ag was used as a reference to evaluate other materials' photon emission power. The gold spectrum indicates it has 22 times fewer photons of 10% lower energy at 3000 times more current in comparison with ZnS:Ag implying that the emission from gold is about 73000 times weaker than from the ZnS:Ag. The output power can be evaluated by dividing the output power of ZnS:Ag emission by how much the gold emission is weaker, i.e, about 15 fW/nA for gold. Finally, for the Gallium nitrate sample the spectra taken show that it is approximately 300 times weaker than the ZnS:Ag, with 6 times fewer photons at 40% higher energy (violet peak) and 72 times more current.

In comparison with gold, it is 240 times better. The output power from GaN was evaluated to be 3.6 pW/nA. These data were used to estimate the signal-to-noise ratio that could be expected from the experimental setup. These are quantified in Table2.2.

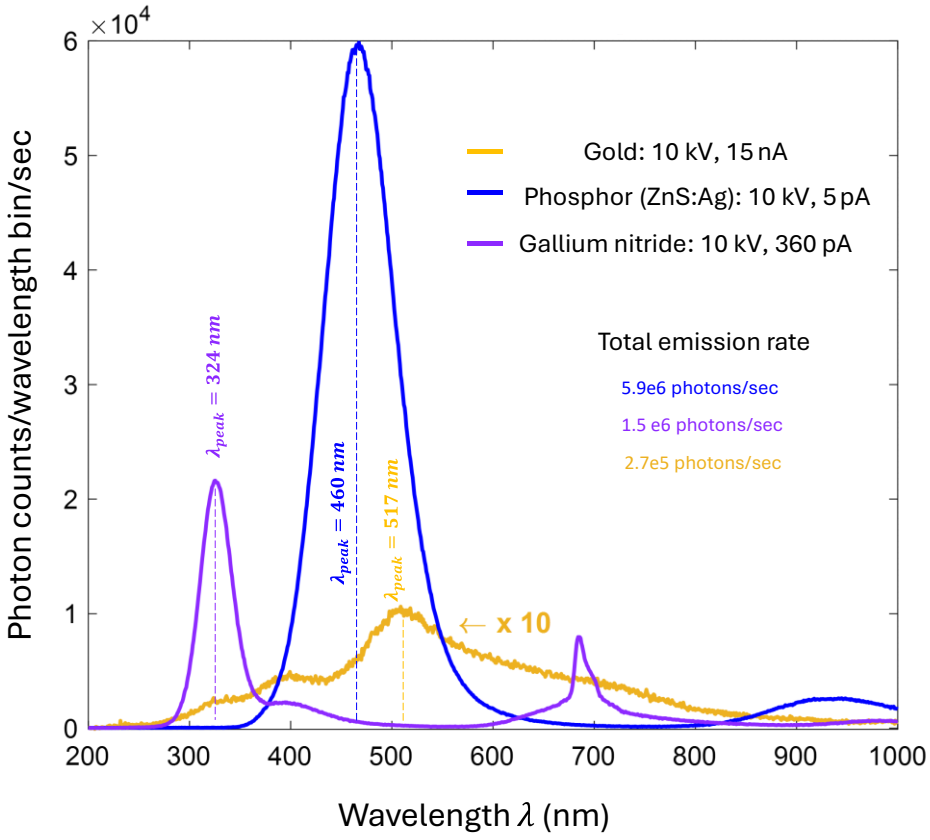

Figure 2.19: ***CL emission spectra of Au in comparison with brighter materials.*** *The CL emission spectra of phosphor (ZnS:Ag) and a single-crystal gallium nitride grown on sapphire are compared with gold thermally evaporated on a silicon nitride membrane. A beam current value less than the value required to saturate the spectrometer is used. For gold, the beam current was the maximum value that could be set at the time of the experiment. The gold spectrum is enhanced 10 times for visibility. The characteristic peak wavelength as well as the total emission rate are indicated.*

When evaluating SNR for nanomechanics, the performance of the instruments that are being used for the experiments is to be considered, where SNR can be assessed using,

$$SNR = \sqrt{\frac{T_{ZI}}{T_{1:1}}} = \frac{P_{opt}\sqrt{T_{ZI}}}{NEP} \qquad 2.35$$

Where $T_{1:1}$ is the measurement duration of the avalanche photodetector (APD) for unitary SNR, which is given by,

$$T_{1:1} = \left(\frac{NEP}{P_{opt}}\right)^2 \qquad 2.36$$

Where NEP is the noise equivalent power and P_{opt} is the output optical power evaluated at 10 nA beam current (the choice of a higher beam current here was to assess what to expect at a beam

current that can produce sufficient photons from a gold sample). The output voltage of the APD is given by,

$$V_{out} = P_{opt} * \Re_M(\lambda) * G \quad 2.37$$

Where $\Re_M(\lambda)$ is the detector's responsivity at the wavelength of interest, which in this case is 16, 21, and 8 A/W, respectively, for the peak wavelengths of 460 nm, 517 nm, and 324 nm. G is the gain, which is set to a maximum of 250 $\mathrm{k}V/\mathrm{A}$. The APD NEP is $90\ fW/\sqrt{Hz}$ (the values are taken from the operating manual).

Table 2.2: ***Quantifying the signal-to-noise ratio for nanomechanics***

Parameters	Phosphor (ZnS:Ag)	Gold (Au)	Gallium Nitride (GaN)
Output power (P_{opt})	1.1 nW/nA	15 fW/nA	3.6 pW/nA
At 10 nA (APD voltage)	11 nW (44 mV)	150 fW (0.8 μV)	36 pW (72 μV)
Measurement duration ($T_{1:1}$) for unitary SNR	67 ps	360 ms	6 μs
SNR for nanomechanics (18.6 ms measurement duration)	17000	0.23	55

To detect 1 MHz oscillation, a sampling rate greater than 2 MHz is needed, and the oscilloscope used offered maximum measurement duration (T_{ZI}) of 18.6 ms at a 3.5 MHz sampling rate. Hence, the SNRs that can be expected if different materials were used for nanomechanical motion detection are evaluated. From Table 2.2, it is evident that gold is not an ideal material for nanomechanical structures used in nanomotion detection with CL under the current setup; however, a longer measurement duration would improve its performance. The other two materials illustrate that the brighter the material (more photon yield), the better the SNR. This led me to use a brighter material-coated nanomechanical resonator instead of a gold-coated one to establish the technique.

2.10.1 Brighter material deposition

Gallium nitride was chosen as the material for making the nanomechanical resonators. It was decided because of two reasons: 1) The availability of the RF sputtering machine (AJA Orion) and a commercially available GaN sputtering target (Testbourne Ltd). 2) GaN finds a vast application in the photonics and optoelectronics community [145-148]. 50 nm of GaN was sputtered on top of a 50 nm Si_3N_4 Membrane in an argon (Ar) and nitrogen (N_2) environment with 30 minutes of sputtering time and 5 mTorr pressure. Initially, the Ar: N_2 ratio was set at 20:5 SCCM.

The CL spectrum from sputtered GaN came out to have a lower photon yield than expected. The RF-sputtered GaN is reported to have more non-radiative recombination centres, such as point defects and line defects, due to the energetic impact of the plasma, and it has lower crystalline quality than GaN grown via metal-organic chemical vapour deposition (MOCVD)[149]. In RF-sputtered GaN, the CL emission shows a prominent deep-level (yellow) band due to the defects, and a weaker near-band-edge ultraviolet emission. Later, an improvement in photon yield was observed, as the amount of N_2 was increased, i.e., Ar: N_2 was set at 15:10 SCCM then, to 10:15 SCCM, respectively. Increasing nitrogen enhances crystallinity and reduces non-radiative recombination centres, which improves the CL emission[150, 151]. Since GaN is a semiconductor material, it was getting charged inside the SEM. To avoid charging, a thin layer of Au was used. To know which combination would produce more photons and less charging, three combinations were considered: GaN/Si_3N_4/Au, GaN/Au/Si_3N_4, and Au/GaN/Si_3N_4, respectively. The latter one had only 2 nm of gold deposited on top. Initially, the Ar: N_2 ratio for GaN deposited was at 20:5 and later changed to 10:15. Figure 2.20 shows all the combinations of the materials that were made and tested for CL emissions. All the samples were kept on the same stub and each time the CL emission spectrum is taken from each sample, the stage is slightly adjusted up or down to maximize the spectrometer output. The total emission rate, which is obtained by integrating the spectrum over its wavelength range of the spectrometer (200 nm – 1000 nm), is shown in the Figure 2.20. The CL spectra were captured using the spectrometer. All measurements were performed at a 1s integration time, a 2mm slit width, and 100 g/mm grating settings, using an electron beam with an acceleration voltage of 10 kV and a beam current of 11 nA.

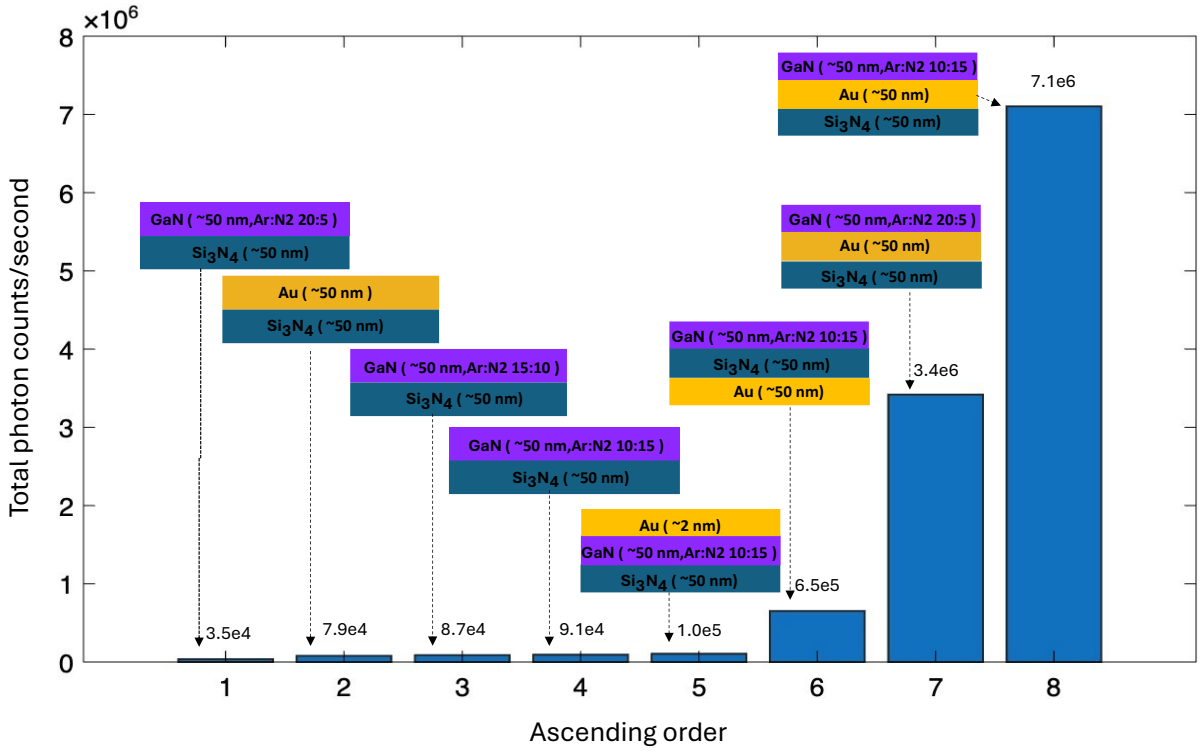

Figure 2.20: ***Total CL photon emission rate from different material combinations.*** *The combinations of materials and their thickness are illustrated.*

The data suggested that having a thin layer of Au on top of GaN can quench the emission rate, as the photons generated from the GaN will often be reflected back from the top metal layers. In the case with an Au layer in between, it maintains contact, hence avoiding charging, and the secondary electrons generated from the middle Au layer will aid in extracting more photons from the GaN layer on top. Au underneath the Si_3N_4 will create a loose contact. GaN deposited in a nitrogen-rich environment produced more photons. Hence, for making the nanomechanical resonators used in the thesis, the combination GaN-Au-Si_3N_4 is used, where GaN is sputtered in Ar: N_2=10:15 SCCM. This has a photon emission two orders of magnitude higher than from the thermally evaporated gold film on top of Si_3N_4.

2.11 Summary

In this chapter, the basic theory behind nanomechanical resonating structures were introduced. The chapter began with the general analytical expression for determining the eigenfrequency of structures such as cantilevers and nanowires (double-clamped beams) for various mechanical modes, as well as how stress can impact their eigenfrequency. From there, forced oscillator dynamics were discussed. This is important since all the nanomechanical resonators used in this thesis are externally driven using a piezoactuator. In Chapter 4, how electron-induced charging affects the nanomechanical response will be discussed in detail. There, the externally driven

damped 1D harmonic oscillator model will be modified to include a Coulomb force term. This will provide an analytical expression for the modified resonance frequency, which incorporates the electron beam parameters and a term for charge.

The forced oscillator discussed in this chapter exhibits linear motion whereas Chapter 5 examines the influence of electron beam on nanomechanical bistability. Bistability is a consequence of nonlinearity, which will be discussed in that chapter. In Chapter 5, the stress dependence of the mechanical eigen frequency is utilised for controlling the bistability.

Later the nature of the electromagnetic field associated with an electron travelling in a vacuum and different electron-matter interactions, with a major emphasis on cathodoluminescence were discussed. Here different coherent and incoherent CL emissions were addressed. A detailed explanation on how to use cathodoluminescence for detecting nanomotion and have also derived an analytical expression for noise equivalent displacement at unitary SNR were provided. Additionally, the influence of electron beam size on the method has been investigated. Numerical simulation and initial experimental results show that the poor photon yield of plasmonic materials like gold makes them a poor choice for developing this method. The choice of gallium nitride and the combination of materials used for making the nanoresonators used in this thesis were also discussed. All the nanoresonators used from now onwards in this thesis are made of GaN/Au/Si_3N_4 layers.

The next chapter (Chapter 3) demonstrates nanomechanical motion detection and imaging using cathodoluminescence with externally driven nanomechanical cantilevers, where most of the aspects discussed in this chapter are applied.

Chapter 3 Nanomechanical motion detection and visualisation through cathodoluminescence

Chapter 1 discusses why the detection and analysis of nanomechanical motion are areas of growing technological importance and scientific inquiry. Techniques involving electron microscopy have long been instrumental in imaging nanoscale structures, and recent advancements have extended their application to the study of dynamic processes[1, 5]. Time-resolved ultrafast electron microscopy, for instance, employs femtosecond laser-driven electron pulses in combination with high-speed detection systems such as streak cameras or time-correlated photon counting to investigate transient phenomena[78]. These methods, operating in pump-probe and stroboscopic configurations, provide both high spatial and temporal resolution, making them powerful tools for capturing ultrafast events in materials. However, these systems are highly specialised and often rely on complex optical setups, strict timing synchronisation, and expensive infrastructure. Other techniques utilising the secondary electron signal modulation offer a promising alternative[5]; they require direct interaction between the electron beam and the sample to generate secondary electrons. It is an inherently an invasive process that can alter or damage sensitive nanostructures. Cathodoluminescence, as discussed in Chapter 2, has shown potential for studying dynamic events [115], yet a technique for nanomechanical motion detection and imaging has not been demonstrated. Importantly, as light can be generated by electrons passing within a few nm of an object (by scattering the moving electron's evanescent field, c.f. Smith-Purcell radiation), as well as by direct impact, this approach offers the possibility of minimally perturbative measurements, i.e. involving energy exchange at the eV level of photons as opposed to the keV levels of secondary electrons, and potential means to probe/distinguish different mechanisms of free-electron interaction with nanostructures.

In Chapter 2, the theoretical considerations and experimental requirements necessary for the implementation of nanomotion detection via cathodoluminescence was outlined. In this chapter, a practical demonstration of the method by detecting the resonance frequencies of three driven nanomechanical cantilevers with varying lengths is presented. This chapter also demonstrates a hyperspectral motion visualisation using cathodoluminescence. This provides for point measurements of motion with nanometric sensitivity and oscillatory mode mapping with spatial resolution of a few nanometers.

3.1 Experimental schematics for nanomechanical motion detection and imaging using CL

The schematics for establishing nanomotion visualisation through cathodoluminescence are shown in Figure 3.1. The setup consists mainly of a modified SEM, which has a parabolic mirror inside and external scan control, a fast photodetector, and a lock-in detection and data acquisition module.

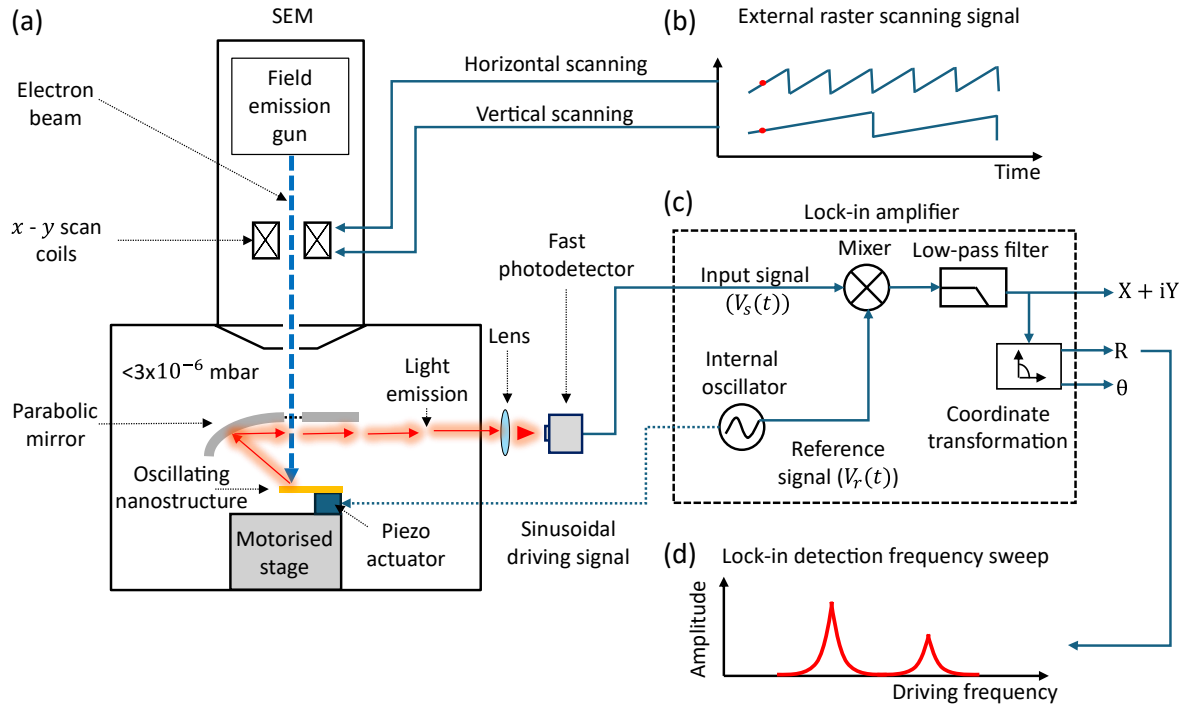

Figure 3.1: ***Schematics for nanomotion visualisation using cathodoluminescence.*** *(a) An SEM having a parabolic mirror to reflect the generated cathodoluminescence out of the high vacuum chamber to a fast photodetector with the help of a focusing lens. (b) The scan coils of the SEM are being controlled externally by a dual-channel arbitrary function generator generating sawtooth signals at different frequencies for raster scanning. (c) The photodetector output signal (the input signal for the lock-in amplifier) and the sinusoidal signal driving forced oscillations via a piezo actuator acting as a reference signal are being used to perform lock-in detection. Here the input signal ($V_s(t)$) is multiplied by the reference signal ($V_r(t)$) in the mixer. The signal from the mixer is low pass filtered, and a complex demodulated signal is generated (X (real) and Y (imaginary)) which is polar coordinate transformed to extract the amplitude (R) and phase (θ) information. (d) To determine mechanical resonances, the SEM is operated in spot mode, and the lock-in measurement as a function of driving frequency reveals peaks in the CL signal at mechanical resonance frequency(s). For imaging mode, the lock-in is then referenced to the clock frequency (internal oscillator frequency) to demodulate the output signal of the photodetector pixel by pixel while raster scanning, building CL signal amplitude and phase maps of the object's movements at the frequency of interest.*

The experiment was conducted using a CamScan3600 SEM with a field emission gun. The electron beam is controlled externally using a dual-channel arbitrary function generator (Tti TGF4242), which generates sawtooth waves: one to control the horizontal fast scanning and the other to control the vertical slow scanning. These signals can be switched to switch the direction of raster scanning. The sample was mounted on a shear piezoelectric stack (Thorlabs PL5FBP3). The sinusoidal driving voltage signal to the piezo-actuator is provided from the signal output of a Zurich Instruments UHFLI 600 MHz lock-in amplifier. The internal clock generator is used to adjust the driving frequency according to the experimental requirements. The sample is kept at the focus of the parabolic mirror inside the SEM chamber, which is under a pressure of < 3 x 10^{-6} mbar. The position of the sample can be adjusted using the motorised stage. The foci of the parabolic mirror and electron beam should be well aligned to have a good light collection efficiency. An optimal position can be achieved by adjusting the pitch and yaw of the parabolic mirror until a position is reached where maximum light is detected by either a spectrometer output (as discussed in Chapter 2) or the photodetector output. The CL that is generated is reflected off the parabolic mirror and channelled outside the SEM chamber and is focused onto an avalanche photodetector (Thorlabs APD440A2, set to maximum gain) using a plano-convex lens (focal distance of 2.5 cm). The photodetector output serves as the input signal to the lock-in amplifier, referenced to the driving frequency, to demodulate the CL signal from the photodetector and retrieve the amplitude and phase information of the motion.

For driven motion detection, the SEM is operated in 'spot mode', where the electron beam is fixed at a particular location (or at a single pixel) of the sample (near to the edge of the oscillating sample) and utilising the frequency sweep option of the lock-in amplifier, the amplitude and phase information from that location is determined.

For imaging, the data acquisition module of the Zurich Instruments UHFLI 600 MHz lock-in amplifier can be utilised, where the sample is driven at a particular frequency and the electron beam is raster scanned pixel-by-pixel to map the object's movements at the set frequency. Simultaneously, the DC component of the signal is also mapped utilising the multi-frequency option of the instrument. Based on the sampling rate and the integration time for lock-in detection, the raster scanning speed can be adjusted.

3.2 Detecting nanomechanical motion using cathodoluminescence

The detection of nanomechanical motion is demonstrated with the help of a series of nanomechanical cantilevers that are set in motion with the help of an external sinusoidal driving signal with 1.5 V_{pp} driving voltage applied to the piezo actuator that the sample is mounted on. The SEM image of the cantilevers used in this study is shown in Figure 3.2a, the lengths (L_i) of the

cantilevers are 27 µm, 25 µm, and 23 µm, respectively, for cantilevers i= 1,2,3. The width (W) was 800 nm. The overall thickness was 150 nm. The inset shows the cross-section of the nanomechanical cantilevers, providing details of the materials used to make them and their respective thicknesses. The cantilevers were made using focused ion beam milling (Chapter 4). All the cantilevers are driven to oscillate parallel to the field of view (in-plane motion) as indicated by a white double-headed arrow. The acceleration voltage of the electron beam was 10 kV, and the beam current was 3 nA. It was set to spot mode and was kept ~ 100 nm away from the edge of each resonator, as indicated by the coloured dots. The movement of the structure will create a fluctuation in the generated light, which is then used for the lock-in measurement.

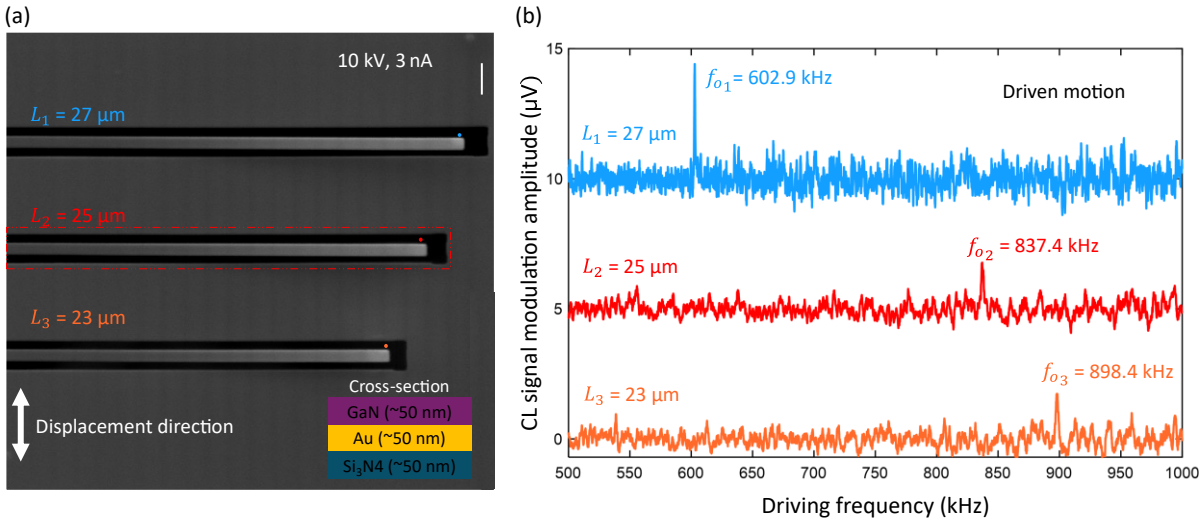

Figure 3.2: ***Nanomechanical motion detection using cathodoluminescence****.(a) The SEM image of the nanomechanical cantilevers used to demonstrate the technique. The inset shows the cross-sectional thickness and materials used. The electron beam parameters, electron beam spot mode position for each cantilever while the measurement is taken (coloured dots), and the externally driven in-plane oscillation direction (white double-headed arrow) are indicated on the image. The scale bar is* 2 µm *long. (b) Nanomechanical motion detected using the cathodoluminescence signal from each cantilever. The peaks indicate the CL signal modulation amplitude at the fundamental in-plane resonance frequency of each cantilever with respect to its base.*

Figure 3.2b shows the detected CL modulation amplitude as a function of driving frequency for each cantilever. (The background has been subtracted in order to characterize the motion of the cantilever tips relative to their driven bases.) It reveals the fundamental in-plane resonance frequency (f_{o_i}) of each cantilever. For this, the frequency sweeper option of the Zurich instrument was used, where the frequency was varied from 500 kHz to 1 MHz with 6000 data points in between. In the modulation amplitude as a function of driving frequency plot, the resonance frequency appears as a sharp peak. Each plot is offset from its neighbouring plot by 5 µV for clear visibility. The data show that as the length decreases, the resonance frequency increases (as

described by Equation 2.8). The experimentally observed f_{o_1}, f_{o_2}, and f_{o_3} matches close to the numerically evaluated in-plane resonance frequencies of 545 kHz, 745 kHz, and 814 kHz, respectively. Factors such as fabrication errors, Young's modulus values used in numerical calculations, and slight bending of the cantilevers due to prolonged exposure to the electron beam during experiments could account for the differences between simulated and experimental results. Charging of the cantilever due to the presence of electron beam can also affect resonance frequencies as demonstrated in Chapter 4.

3.2.1 Mechanical displacement amplitude and quality factor

With the mechanical resonance frequency detected, the quality factor of the cantilever is analysed. For this, the resonance frequency of the middle cantilever from Figure 3.2b ($f_{o_2} = 837.4$ kHz) was selected. The reason for selecting the middle cantilever response was that it was at an optimal and convenient position for imaging (next section). Figure 3.3 shows the calibrated mechanical displacement amplitude around the cantilever's fundamental in-plane resonance frequency with respect to the base of the cantilever. The calibration process of converting from voltages to distance will be explained in the imaging section. The driving frequency range was narrowed down to 5 kHz (835 kHz to 840 kHz), and the number of points was reduced to 4000 with an integration time of 40 ms per frequency step. The data was fitted using the amplitude response function (Equation 2.16) where the numerator (amplitude scaling factor) and the quality factor were used as fitting parameters. The value of quality factor Q was determined to be 1790.

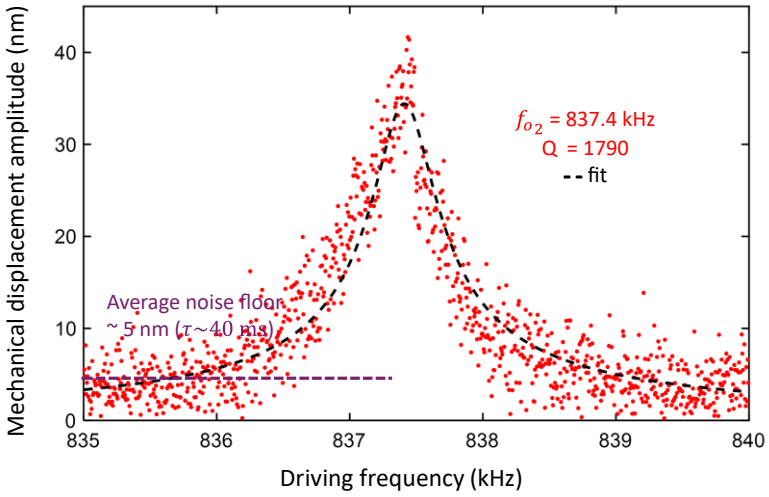

Figure 3.3: ***Mechanical displacement amplitude and quality factor****. The CL signal modulation amplitude of the middle cantilever (highlighted by the red-dotted box in Figure 3.2a) is calibrated to obtain the mechanical displacement amplitude as a function of the driving frequency. The data is fitted using Equation 2.16 with quality factor Q as the fitting parameter. The average noise floor is about* 5 nm *per* 40 ms *of acquisition time per frequency (indicated by the violet line).*

As described in Chapter 2, the motion characterization technique relies upon the gradient $\Delta I_{pn}/\Delta x$ of the photon detection rate at the sharp edges of an object, yielding a value of noise equivalent displacement (with unitary signal-to-noise ratio) $\sim \frac{\Delta x}{\Delta I_{pn}} \sqrt{\frac{I_{pn}(x)}{\tau}}$. Thus, assuming that shot noise is the dominant noise contribution, the signal-to-noise ratio improves proportionally to the square root of the integration time. If the integration time increases to 1s, that is 25 times the current integration time per frequency step,, 5 times improvement in displacement sensitivity may be expected. From Figure 3.3, the noise floor is around 5 nm according to the non-resonant part of the spectrum. A 5-fold sensitivity improvement for an integration time of 1 s implies a noise equivalent displacement amplitude spectral density of 1 nm/$\sqrt{\text{Hz}}$ under typical conditions of beam current and photon yield per electron. Each electron delivers a momentum (p_e) to the cantilever. The momentum $p_e = m_e v_e = m_e \sqrt{2e\text{V}_e/m_e}$, where m_e is the mass of an electron,v_e is the velocity of the electron (here non-relativistic velocity is considered), V_e the acceleration voltage. For an upper bound estimate, if the entire electron beam of beam current (I_e) falls on the cantilever, the maximum force the electron beam as a probe can impart is, $F_{e_{probe}} = \frac{I_e}{e} p_e = \frac{I_e}{e} \sqrt{2e\text{V}_e m_e}$. For 10 kV, 3 nA electron beam this amount to $\sim$1 pN. Considering the cantilever used in Figure 3.3, with $m_{eff} \sim 7$ pg, and $k\sim$ 2 N/m, the displacement (x_{static}) due to the force excreted by the probe on the cantilever is $x_{static} = \frac{F_{e_{probe}}}{k} = 5$ pm. This is negligible compared to the 10s of nm displacement detected.

3.3 Nanomechanical motion imaging using cathodoluminescence

The technique of detecting the motion of nanoscale objects using cathodoluminescence was demonstrated by observing their fundamental in-plane resonance frequency. With that, the next step is to image motion. Before proceeding, the photodetector output signal corresponding to the movement of the nanomechanical cantilever needs to be calibrated to its mechanical displacement amplitude.

3.3.1 Calibrating cantilever displacement to driving voltages

The following process is followed to understand how much the cantilever displaces in response to the driving voltage sent into the piezo actuator. The middle cantilever, marked by a red dot-dashed rectangular box in Figure 3.2a, was selected for this purpose. The tip was zoomed in without any external driving signal, and an SEM image was taken (Figure 3.4a). Then, at the same zoomed-in condition, the cantilever was set to oscillate at a non-resonant frequency of 200 kHz

at varying driving voltages from 0.1, 0.25, 0.5, 0.75, 1, 1.25, and 1.5 V_{pp}. At each driving voltage, an SEM image was captured. From the acquired images, a region is selected (indicated by a navy-blue box in Figure 3.4a), and the pixel values along the vertical direction in each column were averaged, which provided an averaged line scan value for each driven and static case, with the horizontal axis corresponding to the horizontal scale of the SEM image. The top and bottom limits of the line scan data are assigned by plotting a straight line that goes through the average of the last 100 points at the top and the average of the first 100 points at the bottom. Then, another straight line, 5 % less than the top line, and another line equally as far from the bottom line were set. Then the distance between the points where those latter lines intersect the line scan is calculated. This distance D shows how much the cantilever has displaced. This procedure was done for all the images. Figure 3.4b shows the case for the SEM static image shown in Figure 3.4a. The displacement to driving voltage is estimated as half the difference between the D values of the driven case and the static case.

The non-resonance driving calibration curve is shown in Figure 3.4c, where the estimated amplitude of mechanical displacement from the SEM images for each driving voltage sent to the piezo actuator is plotted. The data points are fitted using $y = a_o V_{pp}^2$, where the fit parameter a_o = 10.80 nm/V^2 is taken as the calibration factor. The SEM images taken are with respect to the laboratory frame of reference. The calibration factor is needed to convert the voltage signals to mechanical oscillation amplitudes.

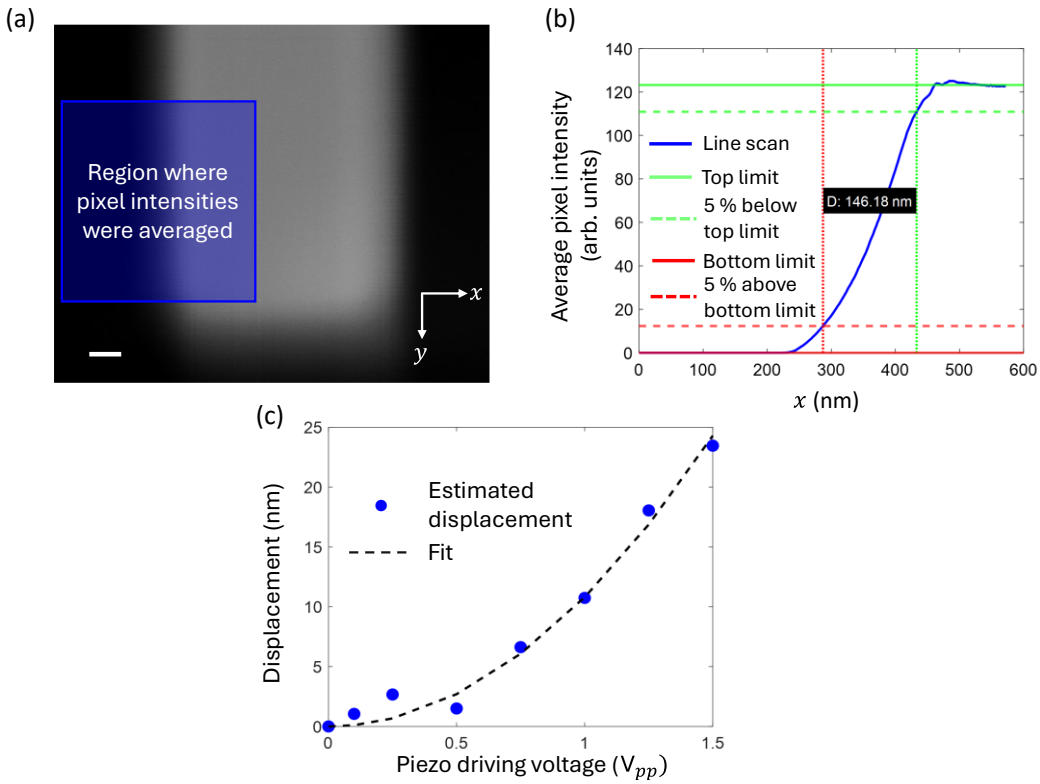

Figure 3.4: ***Calibration curve for displacement as a function of driving voltage****.(a) The SEM image of the tip of the cantilever (marked with a red-dotted box in Figure 3.2a) when not driven. The scale bar is 100 nm long. The region indicated by the navy-blue box is where the pixel intensities are averaged vertically at each horizontal position. (b) Indicates the line scan (navy-blue line) that resulted from averaging the pixels vertically at each x position in a. The top (green line) and bottom limit (red line) indicate the average grayscale value on the cantilever and the vacuum, respectively. A green dashed line, 5 % less than the top limit, and a red dashed line, which is at an equal distance above the bottom limit, are assigned. The distance between the points on the line scan where the dashed lines intersect is indicated as D. (c) The displacement of the cantilever as a function of driving voltage is indicated. These data points are fitted using a fit function* ($y = a_o V_{pp}^2$).

3.3.2 Mode mapping of driven motion using cathodoluminescence

Imaging was performed with the assistance of the data acquisition module (DAQ) of the Zurich Instruments lock-in amplifier. An external signal generator was used to set up two positive ramp signals for controlling both x and y scanning of the electron beam. For horizontal fast scan direction (y direction), the ramp frequency is set to 100 mHz and amplitude to 10 V_{pp}. For vertical slow scan (x direction), the ramp signal frequency was 1.205 mHz with an amplitude of 8 V_{pp}. The horizontal scan signal is used as the trigger for data acquisition. The total imaging time took about 14 minutes for one frame.

At the time of the experiment, the middle cantilever (indicated by a red-dashed box in Figure 3.2a) was positioned at the focal point of the parabolic mirror and the electron beam. This was the

reason to choose that cantilever for performing imaging (Figure 3.5a). The cantilever is then driven to oscillate in-plane using the piezo actuator. A sinusoidal driving frequency of 837.4 kHz (the detected resonance frequency presented in Figure 3.2b) with a driving voltage of 1.5 V_{pp} is sent to the piezo actuator from the internal oscillator output of the lock-in amplifier. The electron beam is then externally scanned across the set field of view. It spends approximately 40 ms per pixel, and the cathodoluminescence generated as a result of the interaction between the electron beam and the spatial position on the cantilever is used for lock-in detection at the driving frequency (which acts as the reference frequency). The lock-in detection of oscillation amplitude and phase information per pixel for a fixed driving frequency across the entire cantilever is collected and stitched together to form the images (Figure 3.5c, d). The phase and amplitude information are with respect to the laboratory frame of reference. Figure 3.5b shows the static CL image, i.e. the DC component of CL that is generated per electron impact position.

A few factors were considered during the imaging process: One, due to external scanning and the line-by-line construction of the image, a random drift can occur between rows of pixels, necessitating correction. Two, the oscillation amplitudes were in units of voltage (the CL signal variation amplitude), which should be calibrated to the mechanical displacement amplitude in meters.

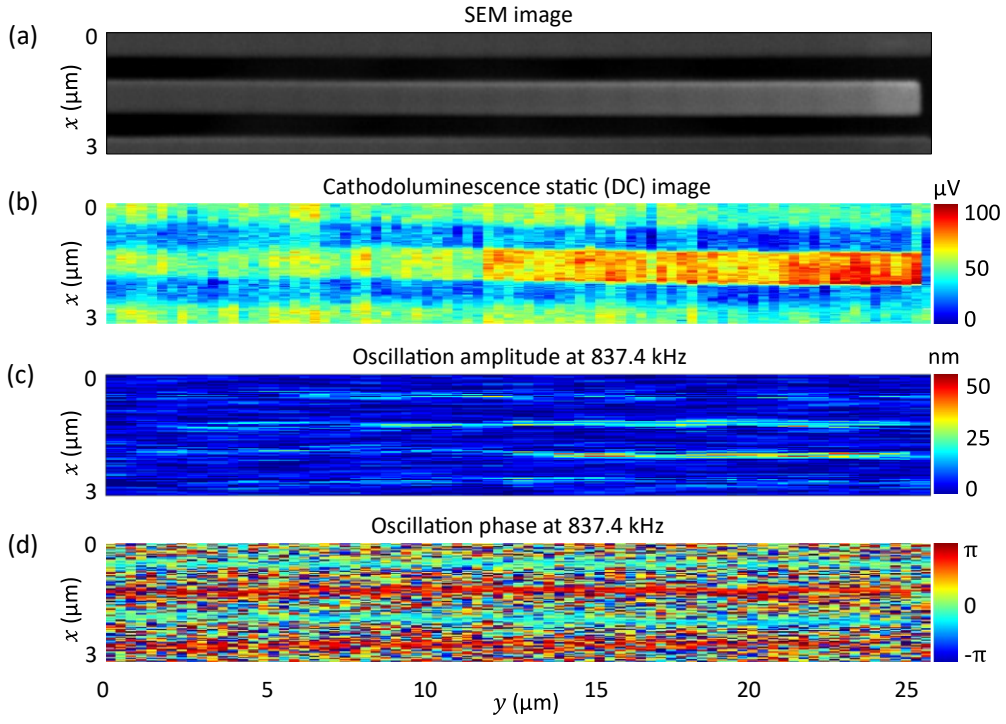

Figure 3.5: ***Mechanical mode mapping using cathodoluminescence.*** *(a) The SEM image of the cantilever that was used for imaging the driven in-plane mechanical mode. (b) Static (DC) cathodoluminescence image. (c) The calibrated in-plane mechanical motion amplitude image of the cantilever with respect to the laboratory frame of reference at a driven oscillation frequency of* 837.4 kHz. *(d) Corresponding phase image at* 837.4 kHz.

The x-drift correction in the images was performed as follows: first, the driven signal amplitude image was divided into four sections, each comprising an edge of the membrane or the edge of the cantilever. Find the x-position that has the highest average lock-in voltage reading at the driving frequency and that has the highest pixel intensity distribution. Then, identify the x-position with the highest detected voltage from oscillation in each row. Calculate the offset. Repeat this process for all rows. This will tell how much each row is shifted. This procedure was repeated for all four sections. After this, the shift values from all four sections were averaged for each row and then fitted with a polynomial (to the nearest integer). These fit values per row were used for shifting each row. Hence, the x-drift was got corrected. The same x-drift correction was applied to all images collected simultaneously during the imaging process.

To convert the measured lock-in voltages to displacement amplitudes in units of length, first, the gradient image was calculated from the DC image. With the CL signal oscillation amplitude image, the gradient of the static image and the calibration factor (discussed above), the mechanical displacement amplitude in units of length was determined as,

$$\frac{\text{CL signal oscillation amplitude (V)}}{\text{DC gradient } \left(\frac{\text{V}}{\text{m}}\right)} \times \text{Calibration factor} \qquad 3.1$$

The calibration factor was determined by considering that, according to the calibration curve for the non-resonance case (Figure 3.4c), the non-resonance part of the image (the edges of the membrane) oscillates with an amplitude of approximately 24 nm. Here, displacements are relative to the lab frame, i.e. including the motion of the driven cantilever base. In contrast, in Figure 3.3c, displacements are shown relative to the cantilever base, i.e. excluding the base motion, resulting in smaller off-resonant values.

This technique, as discussed in Chapter 2 relies upon a high photon yield (and its gradient), hence a brighter material with sufficient fluorescence will help in improving the technique's displacement sensitivity. Limitations such as poor signal-to-noise ratio while imaging can be overcome by increasing the integration time. Though increasing the integration time will increase the overall time taken for imaging. This could affect the nanomechanical behaviour as well as the structure under investigation due to prolonged impact of the electron beam. The SNR can also be improved by collecting more of the photons that are generated and using a photodetector with higher sensitivity. A limitation observed with the setup was the recurring difficulty in maintaining the parabolic mirror and electron beam in proper focus, as they frequently drifted out of alignment.

3.4 Possibility of detecting thermal motion

Establishing the technique for detecting and imaging driven motion led to the question: Is it feasible to detect sub-nm displacement? This would make thermal oscillations in nanomechanical structures accessible, as their amplitudes are typically in a few hundred picometers. A simple way to check the possibility is to drive the sample with a low driving voltage such that the mechanical displacement will be in the sub-nm range. From Figure 3.4c, a driving voltage of 100 mV_{pp} produces a displacement of approximately 1 nm. Reducing the driving voltage by a factor of four therefore implies that the cantilever is driven in the sub-nm displacement regime. Extrapolation of the fitted calibration curve yields an estimated displacement of approximately 7 pm at 25 mV_{pp}; however this value should be regarded as highly approximate. At lower driving voltages, the measured data deviate significantly from the fitted response, as expected due to intrinsic piezoelectric nonlinearity. The piezoelectric materials exhibit hysteresis and creep, which becomes increasingly pronounced at small actuation amplitudes. At such low displacements, the detected signals approach the sensitivity limit of the measurement system, where noise drift, and calibration uncertainty can dominate, leading to a reduced accuracy of displacement measurement. Nevertheless, the measurements reveal detection of the << 1 nm displacement when driving the cantilever at 200 kHz with a driving voltage of 25 mV_{pp}. The power spectral density of the signal was collected using the scope function of the Zurich Instruments lock-in amplifier. Since the scope function does not perform lock-in detection, this is similar to thermal motion detection. The bandwidth of 1.75 MHz with a higher integration time of 1.5 s was set. The number of data points was 2,636,718, and the average was set to 40, resulting in an overall measurement duration of 60 s. The result is shown in Figure 3.6, where the dominant peak at 82.8 kHz and its higher overtones are observed. This was verified to be coming from the photodetector (reason unknown). The inset shows a zoomed in region of the spectra where the driven frequency is detected. This tells that with a higher integration time thermal motion detection should be possible. It should be noted that the detection of the oscillations at 25 mV_{pp} in 60 s is better than what might be expected from the noise level of about 1 nm/$\sqrt{\text{Hz}}$ observed around 835 kHz in Section 3.2.1. The reason is apparent from Figure 3.5, the noise level at 200 kHz is significantly lower, enabling the driven motion peak to rise above the noise.

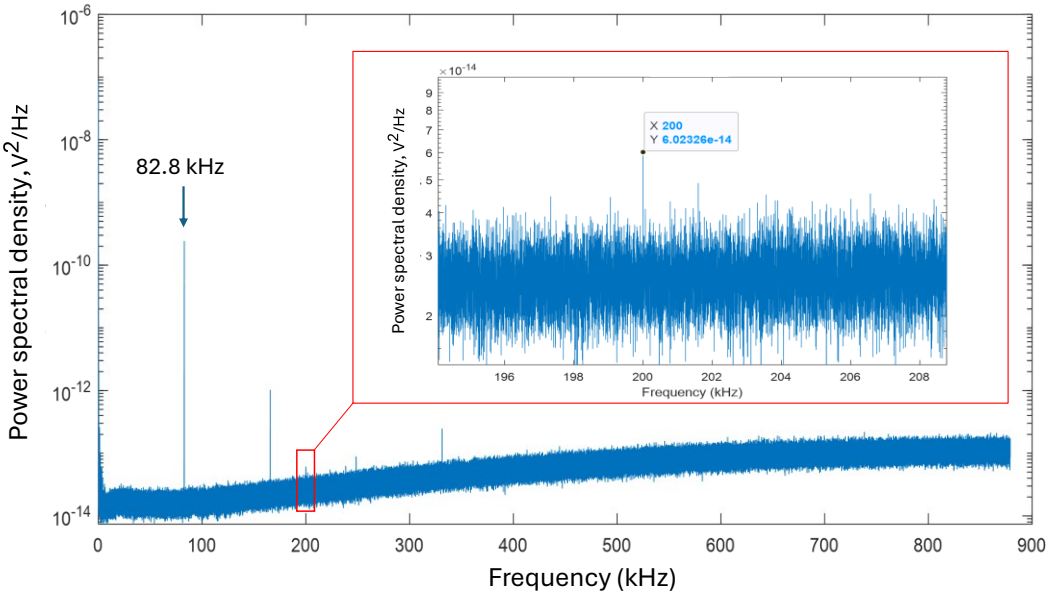

Figure 3.6: ***Detecting sub-nm motion:*** *The cantilever is driven at* 200 kHz *with* 25 $\mathrm{mV_{pp}}$*.The inset shows the driving frequency is detected.*

3.5 Summary

In summary, the motion of nano/microscale objects can be detected and mapped via cathodoluminescence, with nanometric displacement sensitivity and spatial resolution, and MHz bandwidth is demonstrated. This was demonstrated by detecting the in-plane resonance frequencies of externally driven cantilevers of varying lengths. The resonance frequencies were of 100s of kHz. The procedure for converting the detected CL signal modulation amplitude into mechanical displacement amplitude is discussed. The capability of using this technique for hyperspectral motion imaging is demonstrated by mode mapping the amplitude and phase of a driven cantilever at its detected resonance frequency as at zero (DC) frequency. The observed noise equivalent displacement amplitude spectral density is 1 $\mathrm{nm}/\sqrt{\mathrm{Hz}}$ under typical conditions of beam current and photon yield per electron at around 835 kHz and lower at lower frequencies. Indeed, driven oscillations with an amplitude << 1 nm at 200 kHz have been detected with a measurement time of one minute. Cathodoluminescence-based nanomotion detection as demonstrated here could serve as a valuable extension to time-resolved cathodoluminescence techniques.

Chapter 4 Electrostatic control of nanomechanical resonances by an electron beam

In the previous chapters electron-beam probe techniques developed to detect and image fast, small-scale motion with high motion sensitivity and spatial and temporal resolution were discussed. Scanning electron microscopy (SEM) [5, 152] and transmission electron microscopy (TEM)[78] can provide sub-nanometre displacement sensitivity with nanoscale spatial resolution. When combined with time-resolved or stroboscopic methods, they can achieve temporal resolutions of microseconds, even down to nanoseconds or femtoseconds [153]. However, electron beam-sample interaction introduces challenges, such as electron beam-induced carbon contamination [154, 155], electron-induced heating [156], and charging [157, 158]. The imbalance of incident and emitted electrons leads to either negative surface charging. Negative charging occurs when electrons from the incident beam accumulate on or within a sample, typically in non-conductive or poorly grounded materials, because the electrons cannot easily escape[158]. It introduces imaging artefacts [159, 160], distorts the beam trajectory [161], and, most importantly for this study, perturbs the mechanical behaviour of the resonator itself. The mechanical behaviour of charged micro- and nanomechanical resonators has been studied in the context of AFM-based techniques [162-164], where the accumulated charge on the surface of the sample can modify its local electrostatic environment, causing a resonance frequency shift of the probing cantilever due to electrostatic repulsion or attraction of the conductive tip. Such capacitive coupling has been used [48, 165-168] to adjust resonance frequencies by modulating an applied voltage, exploiting the associated electrostatic spring softening or stiffening effect [169, 170]. However, in focused electron beam techniques, such charging effects are usually avoided using metallic conductive coatings [171] and grounding schemes[172-174].

While steps are normally taken in electron microscopy to eliminate or at least minimise charging, this chapter examines the ways in which it can be utilized. A systematic investigation is conducted to examine how electron beam-induced charging affects the resonant behaviour of nanoscale mechanical resonators (Figure 4.1) and explore its potential for tuning mechanical resonances and detecting charged particle beams. The mechanical response of an isolated externally driven cantilever is examined using secondary electron nanomotion metrology [5] for different electron beam positions and currents. An electron-beam-induced blue shift of the resonator's mechanical resonance is observed, attributed to an electrostatic stiffening effect arising from the Coulomb interaction between the electron beam and the charge deposited on the cantilever. A simple analytical model is derived to describe the dependence of the resonant characteristics of a charged mechanical oscillator on a nearby charged particle beam.

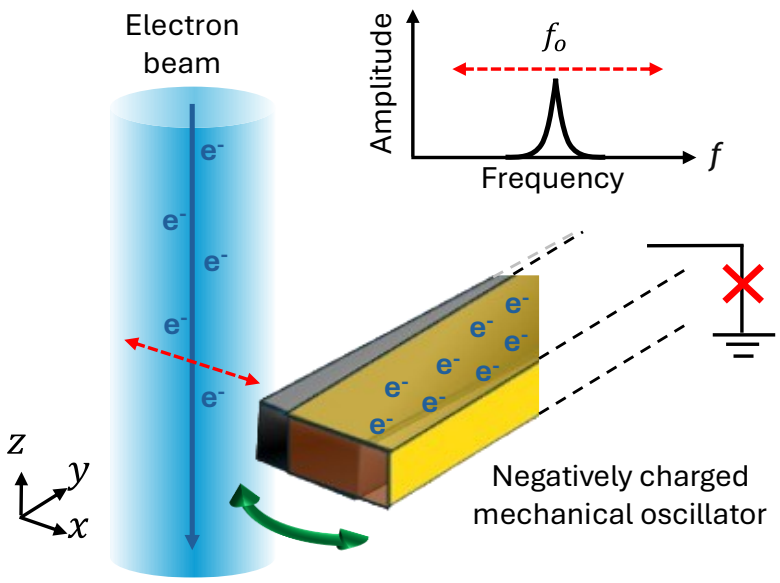

Figure 4.1: ***Illustration of the concept of charging affecting a nanomechanical resonance****. An isolated mechanical resonator will be charged by a nearby electron beam, causing a Coulomb force between the electron beam and the resonator, which stiffens the resonator. Moving the electron beam closer to (away from) the resonator will blue-shift (red-shift) its mechanical resonances.*

4.1 Experiment

The motion of cantilevers cut from a silicon nitride membrane coated with gold and gallium nitride layers, with and without patterning around their base for electrical isolation (Figure 4.2a) is studied. The silicon nitride membrane of 50 nm thickness supported by a 200-μm-thick silicon frame (NORCADA), was coated with 50 nm of gold using a BOC Edwards resistance evaporator and then 50 nm of gallium nitride (GaN) by sputtering using an AJA Orion sputtering machine. The nanomechanical cantilevers were fabricated by focused ion beam milling using a Helios Nanolab 600 SEM-FIB dual beam system. The cantilevers were designed using Design CAD Express 16, and milling was controlled using NPGS software. The magnification was fixed at 2500x, centre-to-centre distance, and line spacing were set as 10 nm. The ion beam current used was 52.9 pA, and the area dosage was 50 mC/cm^2. Then, one of the otherwise identical cantilevers was isolated by FIB milling through the electrically conductive gold layer around its base, which is supported by the membrane's silicon frame, while the other cantilever remained grounded. The sample was mounted on a piezo actuator that is used to drive in-plane oscillations of the cantilevers using a sinusoidal driving voltage of 500 mV$_{pp}$. The SEM is then operated in 'spot mode,' where the electron beam with 1.5 nA current and 10 kV acceleration voltage is positioned (blue dots in Figure 4.2a) at different distances from the edge of the structure. Cantilever motion with respect to the electron beam modulates the rate of electron impact on the cantilever and thus also the resulting rate of secondary electron generation and the output signal of the electron

microscope's secondary electron detector. The experimental setup is the same as illustrated in Figures 3.1a and c, except that instead of using the signal from the avalanche photodetector, The secondary electron signals from the Everhart-Thornley secondary electron detector is used. (Later in this chapter, both signals are used simultaneously.) For a fixed electron beam position and small amplitudes of nanomechanical oscillation, the secondary electron signal modulation is proportional to the oscillation amplitude and measured in my experiments by lock-in detection at the driving frequency. Reference measurements are taken with the electron beam positioned d = 300 nm away from the cantilever edge, a sufficient distance for a negligible influence of the electron beam on the cantilever. The fundamental in-plane resonance frequencies at 332.68 kHz for the isolated cantilever (Figure 4.2b) and 407.69 kHz for the grounded cantilever (Figure 4.2c), with similar resonance quality factors Q of 600 and 630, respectively are observed. A difference in resonance frequency and quality factor for the isolated and grounded, otherwise identical cantilevers is expected. The resonance frequency ($f_o = \frac{1}{2\pi}\sqrt{k/m_{eff}}$) is proportional to the square root of the spring constant and milling near the anchor reduces the spring constant significantly, which will lower the resonance frequency. Removing mass near the anchor produces only small change to the effective mass as it is distributed along the length of the cantilever. With materials removed near the anchor point, the clamping loss can increase, hence can lower the Q. Resonance frequencies and quality factors were determined by fitting Equation 4.10 to the experimental data. Measurements are taken at electron beam distances d from 200 nm to 20 nm from the cantilever edge in 20 nm steps. As the electron beam approaches the edge of the isolated cantilever, its resonance frequency blue-shifts significantly and continuously (Figure 4.2b). In case of the grounded cantilever, a blue shift is also detectable, but it is much smaller and seen only at smaller distances d (Figure 4.2c). For example, the blue-shift arising from positioning the electron beam 100 nm from the cantilever edge is 490 Hz for the isolated cantilever and only 30 Hz for the grounded cantilever, a difference of more than an order of magnitude. For closer proximity of the electron beam to the cantilever edge, the blue-shift continues to increase for both cantilevers, reaching 1170 and 270 Hz at d = 20 nm, respectively. The much larger frequency shift that occurs for the isolated cantilever compared to the grounded one suggests that the blue shift may be caused by charging.

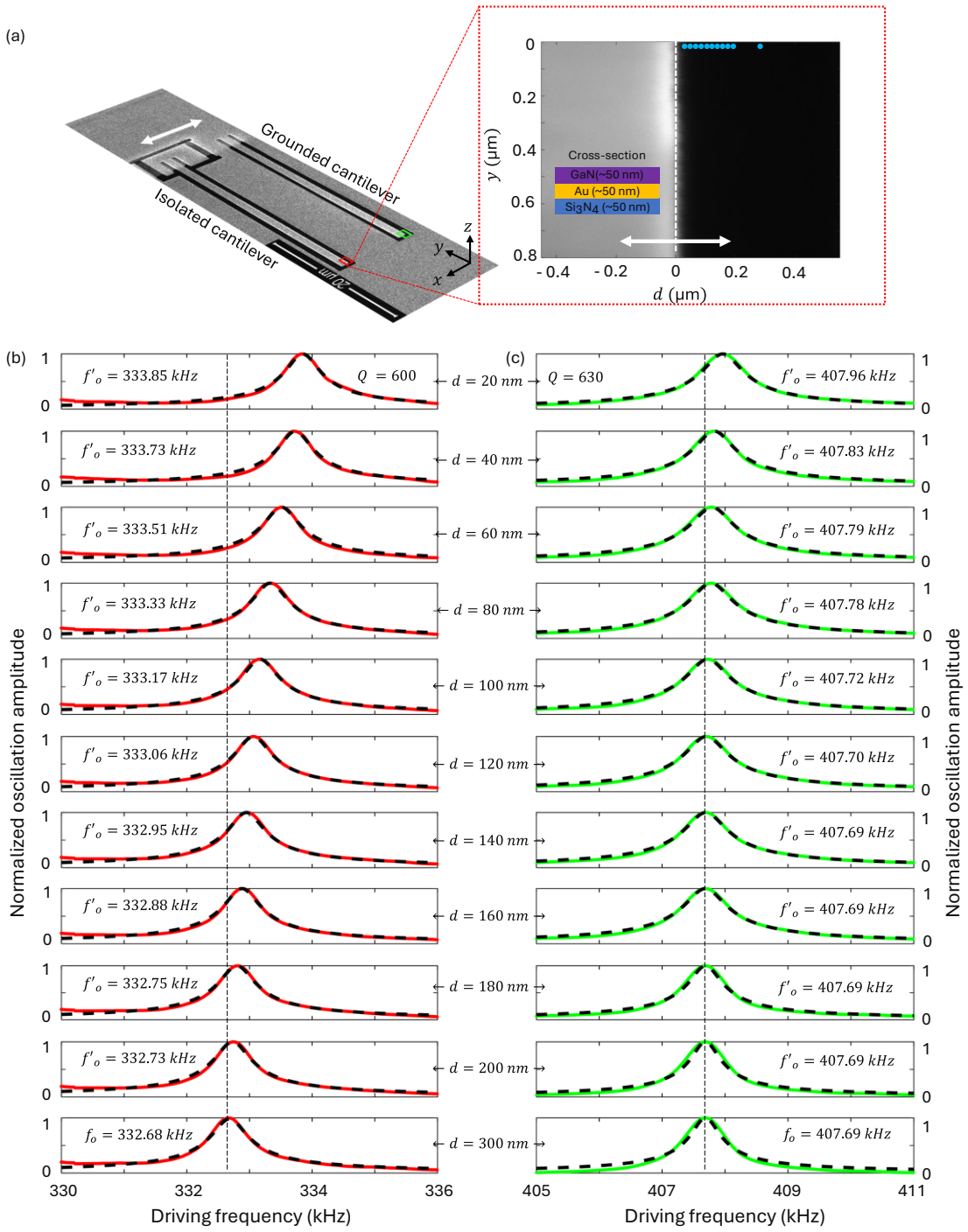

Figure 4.2: ***Mechanical resonances detected at different electron beam injection points for isolated and grounded cantilevers.*** *(a) SEM image of the cantilevers, which are nominally identical with the same layers (inset) and dimensions:* 32 μm *in length,* 800 nm *in width, and* 150 nm *in thickness. The conductive gold layer at the base of one cantilever has been milled away to isolate it electrically (red), while the other remains grounded (green). The motion of the cantilevers is probed by positioning the electron beam (blue dots) at different distances d from the edge (white line) of each cantilever near its tip, as indicated in the enlarged SEM image. Lateral oscillations (indicated by the white double-headed arrow) of the cantilevers are driven by a piezo actuator. (b & c) Oscillation amplitude as a function of driving frequency for the isolated (red) and grounded (green) cantilevers with fits (dashed) according to Equation 4.10. As the electron beam injection position approaches the cantilevers, a blue shift of their resonance frequencies (f_o) is observed, which is much larger for the isolated cantilever.*

4.2 Analytical model

Experimental evidence (Figures 4.2b and c) suggests that the resonance frequency shift is due to the charge buildup on the cantilever and its interaction with the electron beam. The observed blue-shift of the in-plane resonance implies an increase of the cantilever's effective spring constant, i.e. an additional force arising from the charge-electron beam interaction and acting against in-plane (x) displacement of the cantilever. The interaction may be understood by considering the force acting on a point charge (the charged cantilever) placed in the vicinity of a line of moving charges (the electron beam). Being essentially a line charge and line current (along z), the electron beam generates a radial electric and azimuthal magnetic field[175]. Any contributions from the magnetic Lorentz force due to charge motion (due to in-plane cantilever oscillations or charge flow along the cantilever) can be excluded as the interaction of such charge motion in the xy-plane with the magnetic field in the xy-plane can only yield a Lorentz force along z. However, the charged cantilever within the radial electric field of the electron beam will experience a Coulomb force along the direction of its in-plane oscillations (x). Indeed, stronger/weaker repulsion for cantilever displacement towards/away from the electron beam may be expected to yield a stiffening effect and thus a blue-shift of the cantilever's in-plane resonance. Here, we will evaluate how the mechanical resonance is affected by the electric force $\overrightarrow{F_e}$ on a point charge q (representing the charge on the cantilever) located in the electron beam's radial electric field $\overrightarrow{E_e}$.

Approximating the electron beam as a cylindrical wire of infinite length and infinitesimal radius carrying a positive current I_e, Gauss's Law gives the electric field outside the cylindrical charged wire as $\oint \overrightarrow{E_e} \cdot d\vec{A} = Q_{\text{enc}}/\varepsilon_0$. For a cylindrical surface of radius R and length L around the electron beam, the enclosed charge is $Q_{\text{enc}} = (dQ_{\text{enc}}/dL)L = (-I_e/v_e)L$, where v_e is the electron velocity that is determined by the acceleration voltage V_e and given by $v_e = \sqrt{(2eV_e/m_e)}$ in the non-relativistic regime that I consider here ($V_e = 10$ kV). dQ_{enc}/dL is the charge per unit length, ε_o is the permittivity of free space, e charge of an electron, and m_e mass of an electron. Since the field is cylindrically symmetric, $\overrightarrow{E_e}(2\pi RL) = -I_e L/(v_e \varepsilon_0)\hat{e}_r$, rearranging for $\overrightarrow{E_e}$,

$$\overrightarrow{E_e} = \frac{-I_e}{2\pi R v_e \varepsilon_0}\hat{e}_r \qquad 4.1$$

The electric force on a charge q in the radial electric field is

$$\overrightarrow{F_e} = q\overrightarrow{E_e} = \frac{-qI_e}{2\pi R v_e \varepsilon_0}\hat{e}_r \qquad 4.2$$

Considering the negative charge q of the cantilever, the electric force between the electron beam and the cantilever is repulsive. To determine the effect of this repulsive force on the cantilever's fundamental resonance of in-plane oscillation, I take it into account in its equation of motion. The cantilever is treated as a damped harmonic oscillator with mass m_{eff} oscillating about x_o in response to an oscillating driving force and the electric force acting on its charge q within the electric field of the electron beam at a distance $R(t) = R_0 + \Delta x(t)$ (Figure 4.3). Where R_0 is the equilibrium distance between the charge and the electron beam, and $\Delta x(t)$ is the displacement of the cantilever from its equilibrium position x_o. The cantilever's position is $x(t) = x_o + \Delta x(t)$ and without electric force x_o shall be 0.

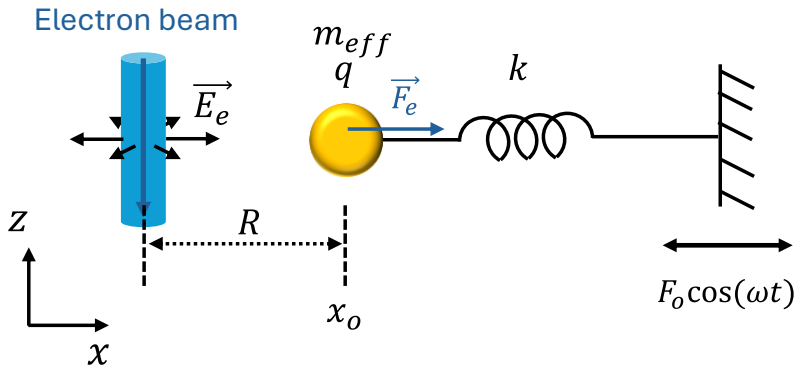

Figure 4.3: ***A simple model for understand how electron-beam-induced charging affects nanomechanics****. A charged and driven mechanical oscillator in the presence of an electron beam can be approximated as a charged mass on a spring under forced vibration within the electric field of an infinitesimally thin cylindrical wire carrying a line charge. The Coulomb electrostatic force alters the effective spring constant, leading to a change in the mechanical resonance frequency.*

The equation of motion of the driven and damped, charged oscillator experiencing a Coulomb force (F_e) is

$$m_{eff}\ddot{x} + b\dot{x} + kx = F_e + F_o cos\,(\omega t), \tag{4.3}$$

Where k is the spring constant, m_{eff} is the effective mass, b is the damping coefficient, F_o and ω are the amplitude and angular frequency of the driving force, and t is the time. Substituting Equation 4.2 in Equation 4.3,

$$m_{eff}\ddot{x} + b\dot{x} + kx = \frac{-qI_e}{2\pi\varepsilon_o v_e}\left(\frac{1}{R_o + \Delta x}\right) + F_o cos\,(\omega t) \tag{4.4}$$

If $|\Delta x| \ll R_o$, the electrostatic term can be approximated using a Taylor expansion $\frac{1}{R_o+\Delta x} = \frac{1}{R_o} - \frac{\Delta x}{R_o^2} + \frac{\Delta x^2}{R_o^3} - \cdots$. Ignoring higher orders,

$$m_{eff}\ddot{x} + b\dot{x} + kx \approx \frac{-qI_e}{2\pi\varepsilon_o v_e R_o} + \frac{qI_e}{2\pi\varepsilon_o v_e R_o^2}\Delta x + F_o cos\,(\omega t) \qquad 4.5$$

Here, $F_{eo} = \frac{-qI_e}{2\pi\varepsilon_o v_e R_o}$ is the electrostatic force acting on the oscillator at its (new) equilibrium position, i.e. it shifts the equilibrium position from 0 to $x_o \approx F_{eo}/k$. Considering this, substituting $x(t) = x_o + \Delta x(t)$ and rearranging, Equation 4.5 simplifies to the equation of motion for the displacement Δx relative to the new equilibrium position

$$\ddot{\Delta x} + \frac{b}{m_{eff}}\dot{\Delta x} + \frac{\left(k - \frac{qI_e}{2\pi\varepsilon_o v_e R_o^2}\right)}{m_{eff}}\Delta x = \frac{F_o}{m_{eff}} cos\,(\omega t) \qquad 4.6$$

Equation 4.6 has the same form as the equation of motion of a forced oscillator (Section 2.2.1) [176],

$$\ddot{x} + \gamma\dot{x} + \omega_o^2 x = \frac{F_o}{m_{eff}} cos\,(\omega t) \qquad 4.7$$

Comparing coefficients of Equation 4.6 and Equation 4.7 gives the modified natural frequency,

$$\omega_o' = 2\pi f_o' = \sqrt{\frac{\left(k - \frac{qI_e}{2\pi\varepsilon_o v_e R_o^2}\right)}{m_{eff}}} \approx \omega_o\left(1 - \frac{qI_e}{4\pi\varepsilon_o v_e R_o^2 k}\right) \qquad 4.8$$

(where the approximation holds for small relative frequency shifts), modified spring constant,

$$k' = k - \frac{qI_e}{2\pi\varepsilon_o v_e R_o^2} \qquad 4.9$$

and amplitude as a function of driving frequency,

$$A(\omega) = \frac{F_o/m_{eff}}{\sqrt{\left[{\omega_o'}^2 - \omega^2\right]^2 + \left(\frac{\omega_o'\omega}{Q}\right)^2}} \qquad 4.10$$

Equation 4.8 and Equation 4.9 imply that the electrostatic force stiffens the spring as the distance between the negative charge and the electron beam decreases, thus increasing the resonance frequency. Equation 4.10 was used to fit the experimental data.

4.3 Evaluating the charge on a cantilever

The analytical expression for the modified resonance frequency, Equation 4.8, can be used to estimate the charge q on the cantilevers in our experiments (Figure 4.2b, c)

$$q = \frac{-2\pi\varepsilon_o v_e R_o^2 k}{I_e}\left(\left(\frac{f_o'}{f_o}\right)^2 - 1\right), \qquad 4.11$$

where, for small relative frequency shifts $\left|\frac{f_o'}{f_o} - 1\right| \ll 1$ as observed here, $\left(\frac{f_o'}{f_o}\right)^2 - 1 \approx 2\left(\frac{f_o'}{f_o} - 1\right)$, implying that the accumulated charge is proportional to the relative frequency shift. Figure 4.4a shows the relative frequency shift as a function of the distance between electron beam and cantilever edge for the isolated (red) and grounded (green) cantilevers, illustrating the much larger electron-beam-induced blue-shift observed for the isolated oscillator. To estimate the charge on the conductive cantilevers, it is treated as a point charge located in the middle of the cantilever, i.e. $R_o = d + W/2$, where W is the cantilever width. The effective mass m_{eff} is calculated from the geometrical and material parameters of the cantilever, which is about 5.7 pg. The spring constant k was evaluated for both cases at the electron beam position that least affects the resonance frequency ($d = 300\ nm$), which were, $k = (2\pi f_o)^2 m_{\text{eff}} = 0.0249$ N/m for isolated cantilever and 0.0373 N/m for grounded cantilever. For 10 kV acceleration voltage, v_e is about 5.93 x 107 m/s and the beam current I_e is 1.5 nA. Figure 4.4b shows the calculated charge as a function of the distance of the electron beam from the cantilever edge. Notably, it indicates that some charging also occurs in the grounded case (green line), which may be expected as some charge will accumulate in the cantilever's non-conductive layers. From the data, a resonance shift of approximately 5% per nanocoulomb in the Isolated cantilever is observed.

The charge q estimated when the electron beam is 20 nm away from the edge of the isolated cantilever is −68 pC, which corresponds to 4 x 10^8 electrons and may be compared to the 8 x 10^{10} gold atoms on the cantilever, implying that the charge corresponds to about 1 electron for every 200 gold atoms. To assess whether the estimated charge is of a realistic order or magnitude, the corresponding potential difference between the cantilever and the surrounding membrane may be estimated. The system consists of a charged planar strip next to two grounded planes. To estimate the structure's capacitance, it was approximated as two wire pairs, each representing one side of the cantilever and the adjacent ground plane. With a gap $g \sim 500$ nm and the cantilever considered as two touching wires of same charge, with each wire having a width of $W/2$, vacuum permittivity ε_o, and length L, the capacitance[177] $C = 2\pi\varepsilon_o L/(\,arcosh(g + \frac{W}{2}/(\frac{W}{2})) \sim$ 1.23 fF, implying a potential difference of about $V = q/C \sim 54$ kV. This is within a factor of a few of the electron beam acceleration voltage (10 kV), that may be expected to be the

maximum achievable potential difference. Given the scale of approximations in both the electrostatic model used to estimate the charge and the capacitance estimation of the cantilever, agreement with respect to the order of magnitude is all that can reasonably be expected, indicating that the model captures the main physical mechanism. Better quantitative agreement may be expected from a model that takes the actual charge distribution on the cantilever into account and from a precise calculation of the capacitance of the actual sample geometry, including the irregular insulation cut around its base.

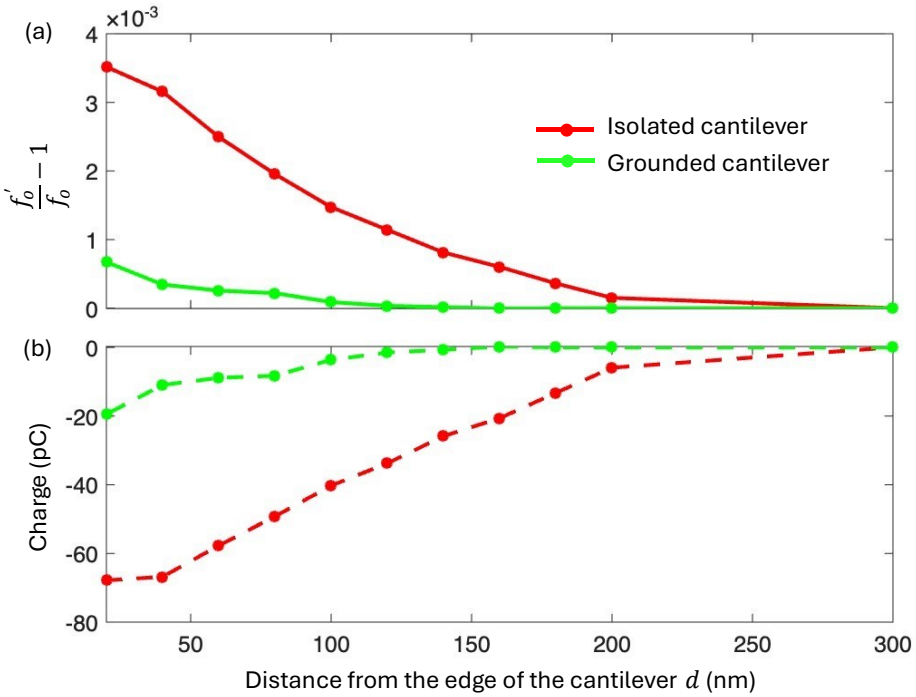

Figure 4.4: ***Relative frequency shift and charge estimation.*** *(a) Relative frequency shift as a function of distance d between the electron beam and the cantilever edge for both grounded and isolated cantilevers. (b) Charge implied by the observed frequency shift according to Equation 4.11.*

4.4 The effect of electron beam current on a cantilever's resonance

The analytical expression for the modified resonance frequency (Equation 4.8) depends on experimental parameters that can be controlled, such as the electron beam acceleration voltage, which controls v_e, beam current (I_e) and the electron beam position. This gives me control over the resonance frequency of the isolated cantilever. Here, the acceleration voltage is fixed to 10 kV and the electron beam injection position at d = 100 nm. Under these conditions, the beam current was varied from 500 pA to 3 nA in 500 pA steps. To demonstrate the simultaneous detection of mechanical motion with secondary electron beam signals and cathodoluminescence signal (as described in Chapter 3), both the signals collected at the same time for lock-in measurements are used and are presented here. The resonance frequency was

observed to increase superlinearly with the beam current (Figure 4.5). Given that the charge accumulated on the cantilever may be expected to be proportional to the electron beam current ($q \sim I_e$), a quadratic dependence of the resonance frequency shift on the electron beam current should be expected according to the approximate form of Equation 4.8. If the fact that an increased size of the electron beam for larger currents further contributes to charging is considered, the resonance should be expected to shift faster than quadratically with electron beam current, and indeed, the observed resonance shift is best fitted by $\Delta f_o \sim I_e^{3.4}$.

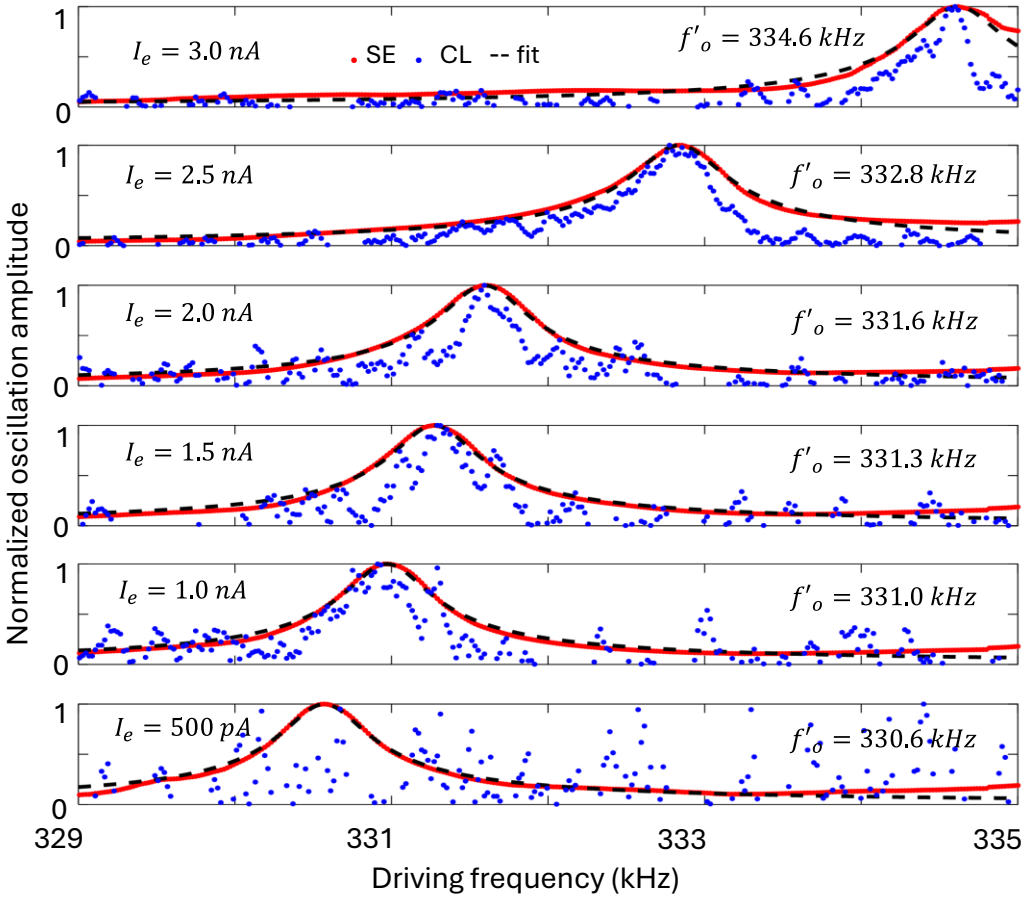

Figure 4.5: ***Beam current dependence of the resonance of an isolated cantilever simultaneously observed using the SE and CL signal.*** *Oscillation amplitude of cathodoluminescence (CL) and secondary electron (SE) signal as a function of driving frequency for the isolated cantilever for different currents (I_e) of an electron beam placed at a distance of $d = 100$ nm from the cantilever edge. The cantilever's mechanical resonance blue-shifts with increasing beam current.*

The oscillation amplitudes determined from cathodoluminescence (blue dots) reproduce those determined from secondary electron detection [red dots, with black fit according to Equation 4.10] at currents of at least 1 nA. When the beam current was reduced to 500 pA, the photon

emission was too low, and due to the limited photon collection efficiency, the signal-to-noise ratio reduced to a state where the photon signals couldn't be resolved. In case of the SE signal, the secondary electron detector is close to the sample and even the fewer SEs that are generated for the lower primary electron beam current can be detected.

The dependence of mechanical resonance frequencies on the charge of the resonator and the presence of nearby charges or charged particle beams provides an opportunity for sensing. For example, resonance shifts of a mechanical resonator with a known charge may be measured to detect nearby charges or the charge of a particle beam. Or the charge of a mechanical resonator may be determined from resonance shifts in the presence of a known nearby charged particle beam, as illustrated above.

4.5 Summary

In summary, the work shows experimentally how the in-plane resonance frequency of a charged nanomechanical resonator depends on its distance from and the current of a nearby electron beam. A blue shift of the mechanical resonance was observed and explained by an analytical model as a consequence of how the Coulomb electrostatic force modifies the effective spring constant of the resonator. The model fits the experimental data and provides an analytical estimate of the charge. For a cantilever of microscale length and nanoscale cross-section interacting with the electron beam of a scanning electron microscope, a resonance shift on the order of 5% per nanocoulomb is observed. This effect may be exploited for sensing of charges and control of mechanical resonances in nanomechanical systems as well as detection of the charge of charged particle beams.

Chapter 5 Electron-beam-controlled volatile nanomechanical bistability

Systems that can exhibit two distinct output states in response to the same input, depending on the history of previous inputs, are known as bistable. Bistability is a feature of nonlinear systems, and many systems become nonlinear upon sufficiently strong excitation. Consider a typical harmonic oscillator, a doubly-clamped nanowire. Increasing lateral displacement will stretch the nanowire increasingly rapidly, causing a stiffening effect that gives rise to a cubic nonlinearity and bistability. The bistable states correspond to different amplitudes of oscillation, and the input may be an external vibration driving its oscillation or any other physical parameter that the vibration depends on. Bistable states can serve as memory and a high-contrast transition between nanomechanical bistable states in response to small changes provides opportunities for highly sensitive detection, e.g. of forces, charges and masses [178-180]. Nanomechanical bistable states can be driven or affected by external and internal factors such as external force[181], capacitance[182], magnetic field[183], stochastic noise[184] or optomechanical coupling[185]. In analogy to optical bistability, which enables ultrafast all-optical switching [186], memory elements[187], pulse shaping and regeneration[188], logic gates[185], transistors and amplifiers[189] etc, all-mechanical bistable signal processing functionalities may also be envisaged, e.g. in the context of the emerging areas of time crystals[27] and timetronics[190]. Exploiting that optical heating can shift nanomechanical resonances[191], the concepts of optical and mechanical bistabilities have been combined to realize a mechanical bistability controlled by light, using nanowires decorated with plasmonic metamolecules[29].

Here, a particular case is demonstrated, in which an electron microscope provides a versatile environment that enables not only the passive imaging of nanomechanical structures and characterization of their motion[5], but also active control over their mechanical behaviour. This chapter reports that the bistable mechanical states of a nanowire, a fundamental and nonlinear building block of NEMS, MEMS and photonic metamaterials[25, 27, 192], may be controlled by an electron beam. As introduced above, when driven into the resonant and nonlinear regime of mechanical oscillation, a nanowire can support two different amplitudes of oscillation under identical conditions. Excitation of and switching between the bistable states may be controlled by changing the frequency of external vibration relative to the nanowire's fixed resonance frequency, or by changing the nanowire's resonance frequency relative to a fixed frequency of external vibration. The latter can be achieved with an electron beam as follows. Energy transfer

from electron impact on the nanowire raises its temperature, and the associated thermal expansion reduces the nanowire's stress, decreasing its mechanical resonance frequencies. For a nanowire that is mechanically driven into the bistable regime of oscillation, the electron-beam-induced resonance frequency changes can be used to cycle through the hysteresis loop of bistable oscillation, i.e. to switch between the bistable states of high and low amplitude oscillation, which are stable under identical conditions (Figure 5.1). This may be achieved by varying the proximity of the electron beam from the edge of the nanowire, or by modulating the electron beam current. As the electron beam can be used to control the nanowire's resonance frequency, it also provides control over the frequency of mechanical oscillation at which bistability occurs.

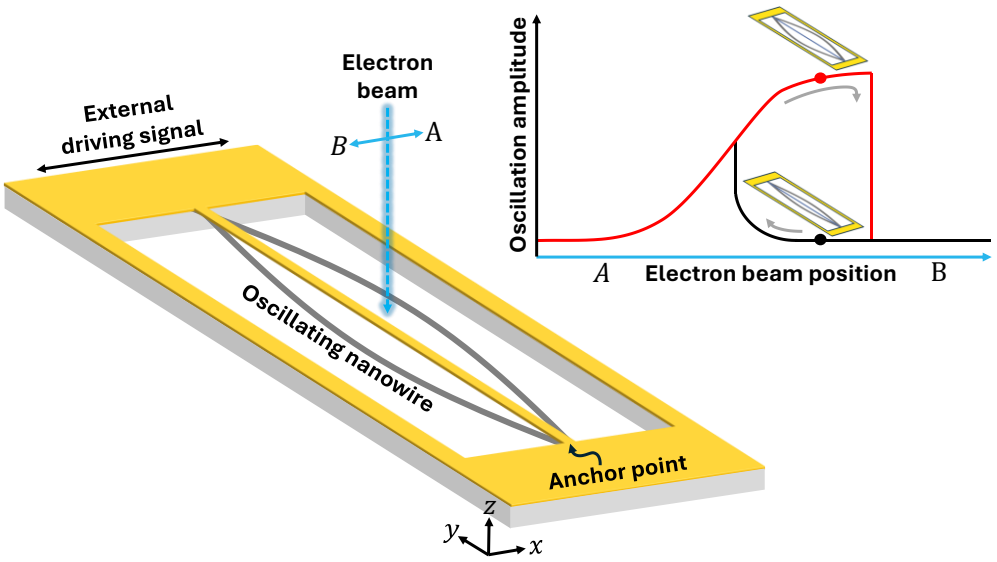

Figure 5.1: ***A free-standing nanowire is driven to its bistable regime of in-plane mechanical oscillation****. The nanowire oscillation and switching between its bistable states of oscillation may be controlled by moving an electron beam relative to the nanowire, as illustrated by the hysteresis loop. Based on the history of the electron beam position the nanowire attains a high or low amplitude of stable mechanical oscillation under identical conditions.*

Section 5.1 provides a fundamental description of nonlinearity in a nanomechanical resonator (a double-clamped beam) and progresses toward mechanical bistability. Section 5.2 provides the experimental results on detecting the nanomechanical bistability using electron beam. Once the bistability is detected, the bistability response change with respect to electron beam position is demonstrated (Section 5.3). Section 5.4 will demonstrate how an electron beam scanning across a nanowire driven into the nonlinear regime of oscillation can be used for controlled switching between bistable states.

5.1 Non-linearity and bistabilty in a nanowire

In Chapters 3 and 4, the nanomechanical resonators exhibited linear behaviour. The underlying physics of this linear resonance response was discussed in Chapter 2. In such a regime, the frequency response curve shows a characteristic Lorentzian peak at the resonance frequency. Importantly, increasing the driving amplitude does not alter the resonance frequency in the linear regime. However, reality deviates significantly from this simplified perspective, as nonlinearities often appears in such systems [89, 193].

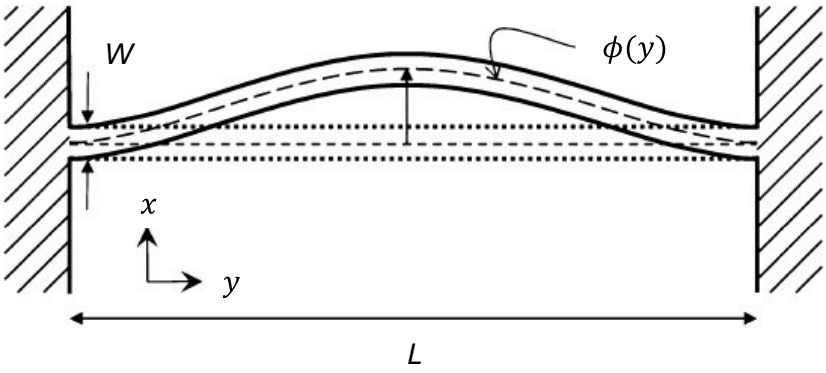

Figure 5.2: ***Schematic illustration of a displaced double clamped beam****. Width (W), length (L) and mode shape along the length (ϕ (y)) are indicated. Figure adapted from [89].*

Consider a typical example of a resonator structure that is clamped at both ends as shown in Figure 5.2. When the structure oscillates with large transverse deflections from its equilibrium position, the length of the resonator elongates, as the arc length of the deformed shape becomes slightly longer than its original, undeformed length L. This introduces additional longitudinal stress along with the initial tensile force ($N_o = \sigma A$) within the beam. Hence the total tensile force following [89] is,

$$N = N_o + EA\varepsilon = \sigma A + EA\frac{1}{2L}\int_0^L \left(\frac{\partial U(y,t)}{\partial y}\right)^2 dy \qquad 5.1$$

Where, E is the Youngs modulus, A is the crossectional area of the beam and ε is the ratio of change in length to original length (longitudinal strain) of the beam. Incorporating the total tensile force into Equation 2.1, The equation of motion can be written as,

$$\rho A\frac{\partial^2 U(y,t)}{\partial t^2} + \frac{EM\partial^4 U(y,t)}{\partial y^4} - N\frac{\partial^2 U(y,t)}{\partial y^2} = 0 \qquad 5.2$$

Adding damping b and driving force F_{ext} along with Equation 5.2,

$$\rho A\frac{\partial^2 U(y,t)}{\partial t^2}+b\frac{\partial U(y,t)}{\partial t}+\frac{EM\partial^4 U(y,t)}{\partial y^4} - \left[\sigma A+EA\frac{1}{2L}\int_0^L\left(\frac{\partial U(y,t)}{\partial y}\right)^2 dx\right]\frac{\partial^2 U(y,t)}{\partial y^2}=F_{ext}(y,t) \quad 5.3$$

The second term inside the square bracket in Equation 5.3 accounts for the nonlinearity since this differential equation is no longer a linear function of $U(y,t)$.

Assuming that the beam is oscillating in one vibrational mode $(n=1)$, $U(y,t)=y_n(t)\phi_n(y)$ (Following Equation 2.2 and dropping the subindex n in this case), with $\phi(y)$ being the mode shape along the length. For simplicity, the intrinsic tensile stress is taken to be zero. Equation 5.3 is then solved using Galerkin's method found in [89, 193], which will result in a lumped model equation that is along the displacement direction (in this case along x axis),

$$\ddot{x}(t)+\frac{b_{eff}}{m_{eff}}\dot{x}(t)+\frac{k_{eff}}{m_{eff}}x(t)+\frac{\alpha_{c_{eff}}}{m_{eff}}x^3(t)=\frac{F_{ext}(t)}{m_{eff}} \quad 5.4$$

Which simplifies to,

$$\ddot{x}(t)+\gamma\dot{x}(t)+\omega_o^2 x(t)+\alpha x^3(t)=\frac{F_{ext}(t)}{m_{eff}} \quad 5.5$$

Where $\gamma=b_{eff}/m_{eff}$ is the damping parameter, $\omega_o=\sqrt{k_{eff}/m_{eff}}$ is the resonance frequency $\alpha=\alpha_{c_{eff}}/m_{eff}$ is the coefficient of cubic nonlinearity (nonlinear stiffness) and $F_{ext}(t)=F_o\cos(\omega_d t)$.

Equation 5.5 can be solved by treating the nonlinearity as a small perturbation to the linear case; a detailed derivation is provided in [193]. Solving for amplitude of motion as a function of driving frequency (ω_d),

$$A_o(\omega_d)=\frac{\left(\frac{F_o}{2m_{eff}\omega_o}\right)^2}{\left(\frac{\omega_d-\omega_o}{\omega_o}-\frac{3}{8}\frac{\alpha}{\omega_o^2}A_o^2\right)^2+\left(\frac{1}{2Q}\right)^2} \quad 5.6$$

Equation 5.6 tells that for small amplitude of motion; the mechanical motion amplitude response follows a Lorentzian shape as described by Equation 2.16. Asymmetric resonance curves will appear as the mechanical motion amplitude increases. The amplitude at which the behaviour starts to change from linear to nonlinear is the critical amplitude A_c, which is found by imposing $\frac{d^2\omega_d}{(dA_o^2)^2}=0$. Which leads to,

$$A_c = \sqrt{\frac{8}{3\sqrt{3}}}\frac{1}{\sqrt{\mathrm{Q}}}\sqrt{\frac{m_{eff}\omega_o^2}{\alpha_{c_{eff}}}} \qquad 5.7$$

From Equation 5.7 it can be seen that, for a high-quality factor and low mass resonator, the nonlinear regime can be accessed easily. For the first mode of a double clamped beam moving in-plane, the geometric nonlinearity regime is entered at a critical amplitude value of $\approx 1.46\, W/\sqrt{\mathrm{Q}}$ [89]. In order to operate in the linear regime, the resonator amplitude of motion should be less than the critical amplitude.

The frequency at which the maximum amplitude response occurs is found by setting the derivative of the amplitude with respect to the driving frequency to zero, i.e., $\frac{dA_o(\omega_d)}{d\omega_d} = 0$, which gives,

$$\omega_{max} = \omega_o + \frac{3}{8}\left(\left(\frac{\alpha}{\omega_o}\right) A_{o\,max}^2 \quad\right) \qquad 5.8$$

If α is positive (negative), the effective stiffness increases (decrease) with amplitude of motion, which will make the resonance peaks to bend towards higher frequencies (lower frequencies). Such tilting is the typical behaviour of Duffing resonators.

Bistability is characteristic of Duffing resonators and gives rise to hysteresis in the resonator response during a frequency sweep; the final response depends on whether the sweep is performed from low to high frequency or vice versa. The resonance behavior is expected to transition from a stable to an unstable solution, which in practice corresponds to the vertical jumps in the amplitude response, and those can be calculated by imposing $\frac{d\omega_d}{dA_o^2} = 0$. This results in two distinct families of points, each corresponding to the transition associated with the direction of the frequency sweep.

5.2 Observation of bistability using an electron beam

The nanowire used here has 47 µm length (*L*), 400 nm width (*W*) and a thickness (H) of 150 nm (Figure 5.3a). It was fabricated by focused ion beam milling (FEI Helios Nanolab 600) of a 50 nm thick silicon nitride membrane supported by a 200 µm thick silicon frame (NORCADA) that was coated with a 50 nm of thermally evaporated (BOC Edwards) gold and then 50 nm of sputtered (AJA Orion) gallium nitride (GaN). The nanowire is anchored to the silicon frame at both ends. The entire sample is mounted on a shear piezoelectric stack (Thorlabs PL5FBP3) to drive in-plane displacements along x (Figure 5.3a). Piezo displacements are driven by a sinusoidal voltage with swept (or fixed) frequency from the signal output of a lock-in amplifier (Zurich Instruments UHFLI

600 MHz). The experiment was conducted using an SEM (CamScan3600). The sample is kept inside the SEM chamber in vacuum with 3 μbar pressure. Lock-in detection of the modulation of the secondary electron signal arising from nanowire motion relative to the electron beam position was used to study the nanowire's mechanical response[5, 152, 194]. The SEM is operated in 'spot mode,' where the electron beam with 1.3 nA current (I_e) and 10 kV acceleration voltage (V_e) is positioned (blue dot in Figure 5.3a) near the centre of the nanowire (along y) at a distance (d) away from its edge (along x). The secondary electron signal is collected using an Everhart-Thornley secondary electron detector and fed into the signal input channel of the lock-in amplifier for detection, using the driving signal as the reference.

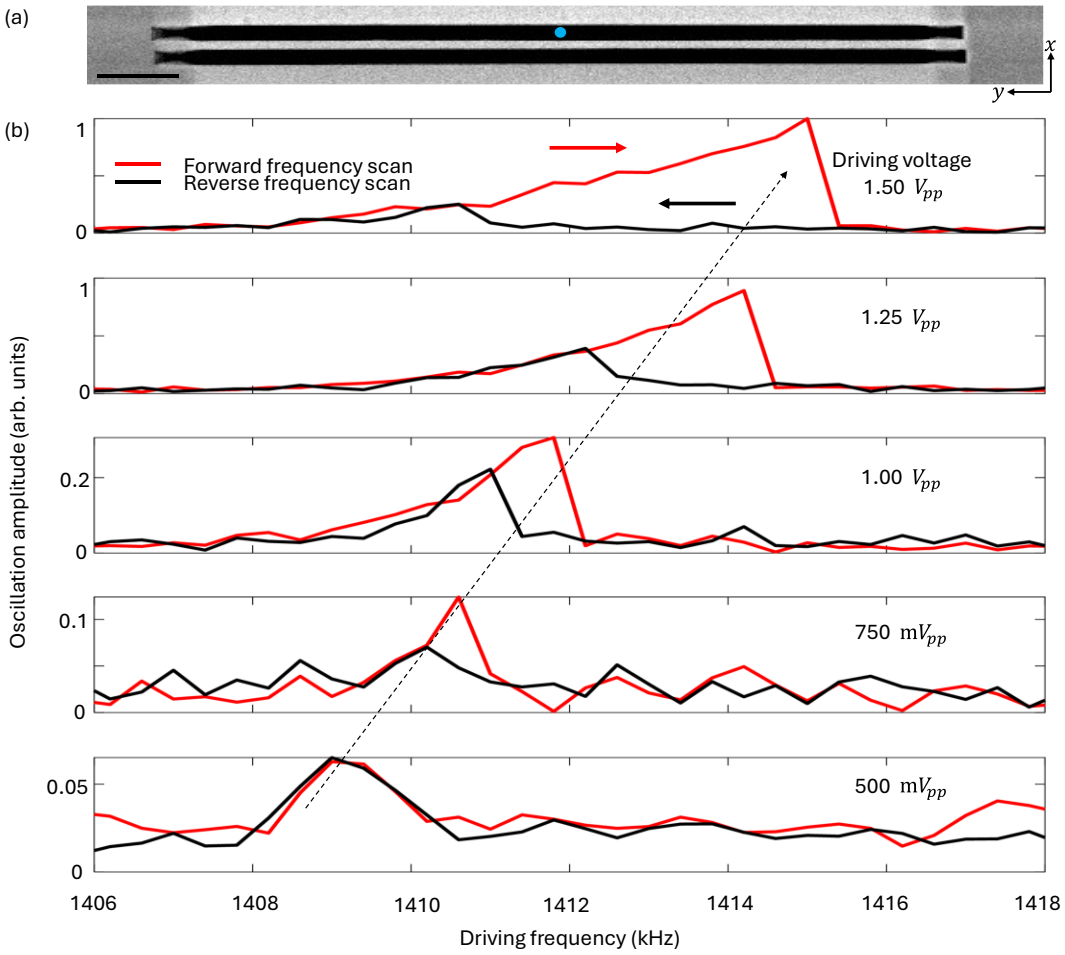

Figure 5.3: ***The nanowire and its transition from linear to non-linear oscillation.*** *(a) SEM image of the nanowire. In-plane displacement along x is driven piezoelectrically using a sinusoidal voltage and detected as modulation of secondary electron generation with a fixed electron beam impact position (blue dot) about* d = 150 nm *from the nanowire edge. The scale bar is* 5 μm *long. (b) Amplitude of nanowire oscillation as a function of increasing (red) and decreasing (black) driving frequency for different driving voltage amplitudes. The nanowire transitions from linear to non-linear and bistable oscillation with increasing driving amplitude.*

Figure 5.3b shows how the nanowire transitions from linear to nonlinear and bistable oscillation when being shaken with increasing amplitude. The oscillations are driven via the piezo using bidirectional frequency sweeps at different fixed voltage amplitudes from 500 mV_{pp} to 1.5 V_{pp}. The electron beam passes at a distance d = 150 nm from the nanowire edge and the oscillation of the nanowire's centre is monitored by detecting the resulting modulation of the secondary electron signal. To show the nanowire's amplitude of oscillation relative to its driven anchor points, the anchor point oscillations given by the average non-resonant measurement background were subtracted. The curves are normalized to the overall maximum oscillation amplitude occurring for 1.5 V_{pp}. The bidirectional frequency sweeps at a low driving voltage (500 mV_{pp}) reveal Lorentzian bell shapes at the same frequency. This characteristic resonance peak of a harmonic oscillator evolves into an asymmetric resonance peak with a sharp high frequency foldover wing[195] and hysteresis as the amplitude of flexural oscillations increases at larger driving voltages. This leads to bistability: The shape of the curve depends on the frequency sweep direction, and the non-linear resonator can have a large or small amplitude of oscillation under identical conditions depending on the history previous driving frequencies. For example, at a driving voltage amplitude of 1.5 V_{pp}, the oscillation amplitude is 18 times larger when the oscillation frequency is increased to 1414 kHz than when it is decreased to 1414 kHz.

As discussed in Section 5.1, the bistability occurs due to the nanowire's mechanical nonlinearity, also known as geometric nonlinearity, which arises from the nanowire stiffening due to being stretched by significant lateral displacement as its anchor points remain fixed. The resulting motion can be described by the nonlinear Duffing equation[89] (Equation 5.5)), $\ddot{x} + \gamma\dot{x} + \omega_o^2 x + \alpha x^3 = \frac{F_o}{m_{\text{eff}}}\cos(\omega_d t)$. Here, $\gamma, \omega_o, m_{\text{eff}}$ are the damping parameter, in-plane resonance frequency and effective mass of the nanowire. F_o is the amplitude of the external driving force that is oscillating at driving frequency ω_d. Stiffening of the nanowire due to stretching increases its spring constant at larger displacements, which is accounted for by the cubic term, where α is the nonlinear stiffness coefficient. This Duffing nonlinearity becomes significant as the in-plane displacement x approaches the nanowire's width.

5.3 Effect of the electron beam on the bistable resonance

Energy dissipated as the electron beam interacts with the nanowire by inelastic scattering of electrons increases the nanowire's temperature, leading to thermal expansion and associated changes in stress and resonance frequency. To investigate how the electron beam position relative to the nanowire affects the bistable response, the nanowire oscillation is characterized in response to increasing and decreasing driving frequencies at a fixed driving voltage of 1.5 V_{pp} for different distances d between electron beam and nanowire edge (Figure 5.4). The oscillation

amplitude signals are normalized to the maximum obtained at each electron beam location. The data show that the nanowire's resonance and associated bistable response red-shift as the electron beam is positioned closer to the nanowire edge. Such a shift may be expected to arise from electron-beam-induced heating of the nanowire, which will cause thermal expansion and an associated stress reduction, which will reduce the nanowire's natural frequency. The closer the electron beam is to the oscillating nanowire the more electrons will interact with the nanowire and the bigger temperature increase, stress reduction and red-shift. Qualitatively similar behaviour has been reported for optical heating of mechanical resonators[29]. For electron-beam-induced heating, the effect depends on the geometry, electron beam parameters and effective thermal conductivity, κ of the nanowire. The average temperature change above ambient temperature of the nanowire can be estimated as $\Delta T \approx \xi P' \mathrm{L}/(8\kappa \mathrm{WH})$[89], where P' is the amount of electron beam power falling on the nanowire and ξ being the fraction of that power absorbed by the nanowire materials that will contribute to the heat production. To provide an upper limit, It is assumed that all incident power ($P' = I_e \mathrm{V}_e$) is converted to heat ($\xi = 1$). With $\kappa \approx$ 156 $\mathrm{Wm^{-1}K^{-1}}$, the electron beam carries enough power to heat the nanowire by $\Delta T \leq 8$ K. Following [89], the cooling time is $\Theta = \mathrm{L}^2 C_v/8\kappa \approx 4.5$ μs where C_v =2.54 x $10^6\ Jm^{-3}K^{-1}$ is the effective volume heat capacity of the nanowire.

This can be compared with an estimate of the temperature increase required to explain the observed frequency shift based on bulk material parameters. The nanowire's resonance frequency according to Euler–Bernoulli beam[83, 196] theory is given by $f_o(\sigma) = 1.03\left(\frac{W}{\mathrm{L}^2}\right)\sqrt{\frac{E}{\rho}}\sqrt{1+\frac{\sigma \mathrm{L}^2}{3.4EW^2}}$, with effective density $\rho \approx 9490\ \mathrm{kg\ m^{-3}}$, effective Young's modulus $E \approx$ 205 GPa, tensile stress $\sigma = \sigma_0 - \alpha_{\mathrm{eff}} E \Delta T$, initial stress σ_0 and effective thermal expansion coefficient $\alpha_{\mathrm{eff}} \approx$ 4.1 x $10^{-6}\ \mathrm{K^{-1}}$ of the nanowire. Table 5.1 shows the materials and associated material properties that are used in this thesis[5, 29, 197, 198].

Considering a resonance frequency $f_o = 1416.2$ kHz at d = 200 nm (Figure 5.4), where the nanowire is least thermally affected by the electron beam, the initial stress σ_0 is estimated to be 84.3 MPa. The resonance shift of -4.4 kHz to 1411.8 kHz that is observed as the electron beam is moved much closer to the nanowire edge (d = 50 nm) implies a stress reduction by about 0.8 MPa and an electron-beam-induced increase of the nanowire's temperature by $\Delta T \approx 1$ K , which is consistent with the heating the electron beam can provide.

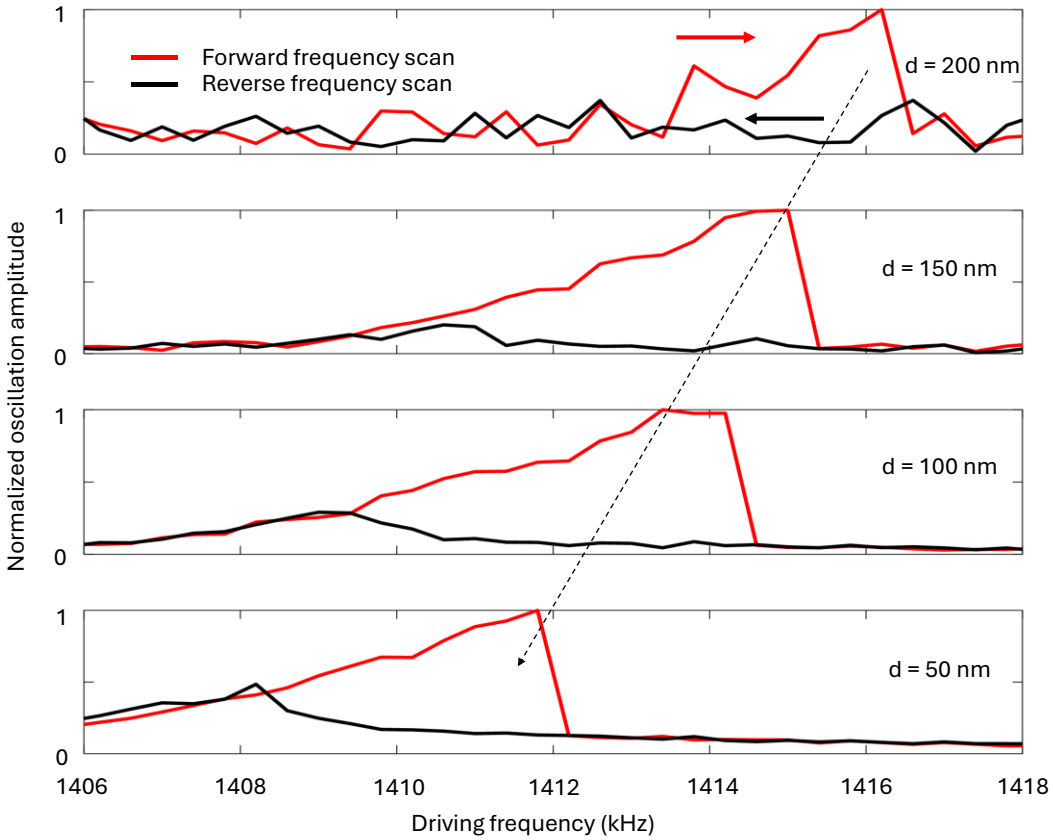

Figure 5.4: ***Effect of the electron beam position on the nanowire's bistable resonance****. Nanowire oscillation amplitude as a function of increasing and decreasing driving frequency for a fixed driving voltage (1.5 V_{pp}) and different distances d of the electron beam from the nanowire edge. The data for each distance is normalized to its own maximum. The black dashed arrow indicates a red-shift of the bistable resonance as the electron beam is positioned closer to the edge of the oscillating nanowire.*

Table 5.1: ***Materials used for making the nanomechanical resonators and their mechanical and thermal properties.***

Material	Density, ρ ($\mathrm{kg\,m^{-3}}$)	Young's modulus, E (Pa)	Thermal expansion coefficient, α ($\mathrm{K^{-1}}$)	Thermal conductivity, κ ($\mathrm{Wm^{-1}K^{-1}}$)	Volume heat capacity, C_v ($\mathrm{Jm^{-3}K^{-1}}$)
Si_3N_4	3100	$250 * 10^9$	$2.3 * 10^{-6}$	20	$2.1 * 10^6$
Au	19300	$70 * 10^9$	$14.2 * 10^{-6}$	317	$2.5 * 10^6$
GaN	6070	$296 * 10^9$	$3.2 * 10^{-6}$	130	$3 * 10^6$

5.4 Electron-beam-controlled switching between bistable states

Given that the spectral position of the bistable resonance depends on the position of the electron beam with respect to the nanowire, one may expect that switching between the bistable states can be achieved by modulating the electron beam position instead of the driving frequency. Figure 5.6 shows the nanowire's oscillation amplitude as a function of decreasing and increasing distance d between electron beam and nanowire for selected fixed driving frequencies. To achieve this, the magnification is adjusted to a field of view of 3.0 µm × 2.4 µm, which was sufficient to keep the nanowire centred while simultaneously capturing both edges of the membrane (inset of Figure 5.5a). The nanowire was then driven at a fixed frequency, for example, 1408 kHz at 1.5 V_{pp}.

Once the nanowire was driven at the chosen frequency, a triangular ramp signal with a 50:50 duty cycle, a time period of 10 s (100 mHz), and an amplitude of 10 V_{pp} was applied from an external dual-channel arbitrary signal generator to control the horizontal scan coil (x-axis) of the SEM. No signal was applied to the vertical scan coil, resulting in a bidirectional horizontal line scan across the middle of the field of view (5 s per direction). The SEM was operated in external scan mode.

During the line scan, lock-in detection was performed at the driving frequency using the secondary electron signal, while the DC signal was collected simultaneously. The acquired secondary electron signal modulation amplitudes were subsequently spliced and overlaid to reveal the hysteresis behaviour (inner peaks, Figure 5.5b). The peaks observed at the membrane edges served as alignment markers (outer peaks, Figure 5.5b). Finally, the data were overlaid with the DC signal gradient to relate the spatial positions at which bistability behaviour was observed to the edges of the nanostructure. Hysteresis is observed at both the edges of the nanowire (Figure 5.5b and c).

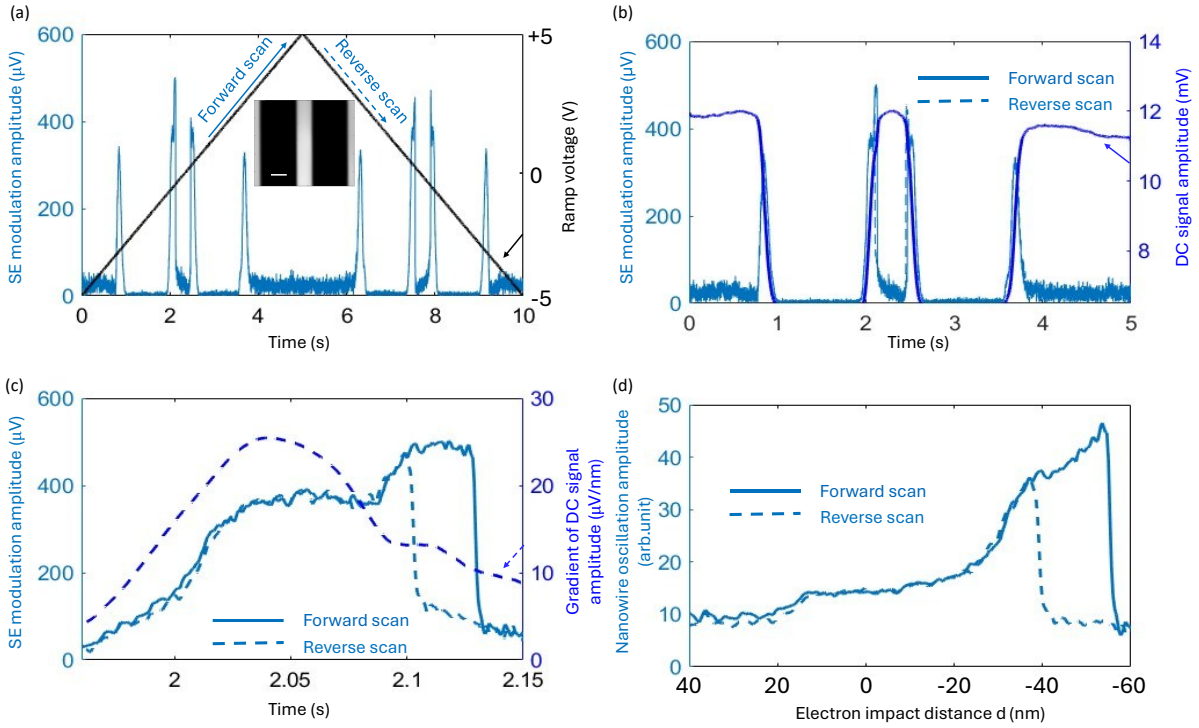

Figure 5.5: ***Experimental procedure to detect and characterize the bistability response.****(a) A triangle ramp signal of* 10 s *period is used to do a bidirectional scan across the middle of the SEM image provided as inset (scale bar is* 400 nm *long). The secondary electron signal from a lock-in measurement to a fixed driving frequency (*1408 kHz at 1.5 V_{pp}*) is collected during the bidirectional scan. (b) The bidirectional scan data are spliced and overlapped to compare both 5s directional scans. The peaks in signals from the membrane edges were used to align both scans. The data is overlayed with the DC signal (linescan). (c) Secondary electron modulation amplitude as the electron beam is scanned across one nanowire edge. The SE modulation amplitude peaks in the bistable region and also at the nanowire edge. The data is overlayed with the DC signal gradient to make sure the additional bump observed in the collected signal is due the the sensitivity of SE detection technique at positions of high DC SE signal gradient. (d) The nanowire oscillation amplitude is calculated by dividing the SE modulation amplitude by the DC SE gradient. The time scale is converted to the length scale of the SEM image, assigning the position of highest DC SE gradient to the edge of the nanowire.*

Bidirectional line scans were performed using the electron beam across the nanowire edge, identifying the edge (d = 0) as the maximum gradient of the DC secondary electron signal (which is equivalent to finding the edge on an SEM image). Since the secondary electron signal modulation *M* at the driving frequency is proportional to both the nanowire's oscillation amplitude *A** and the local gradient *G* of the DC secondary electron signal in the direction of movement[5], the nanowire's oscillation amplitude was determined as the ratio *M/G* (Figure 5.5d and Figure 5.6). Bistability is indeed observed of the nanowire's oscillation amplitude as the electron beam is moved relative to the nanowire edge, with the oscillation amplitude following the upper (lower) branch of the hysteresis loop when the electron beam moves towards (away

from) the nanowire. At lower (higher) driving frequencies, the bistability is observed for electron beam positions that are closer to (further from) the nanowire (Figure 5.6).

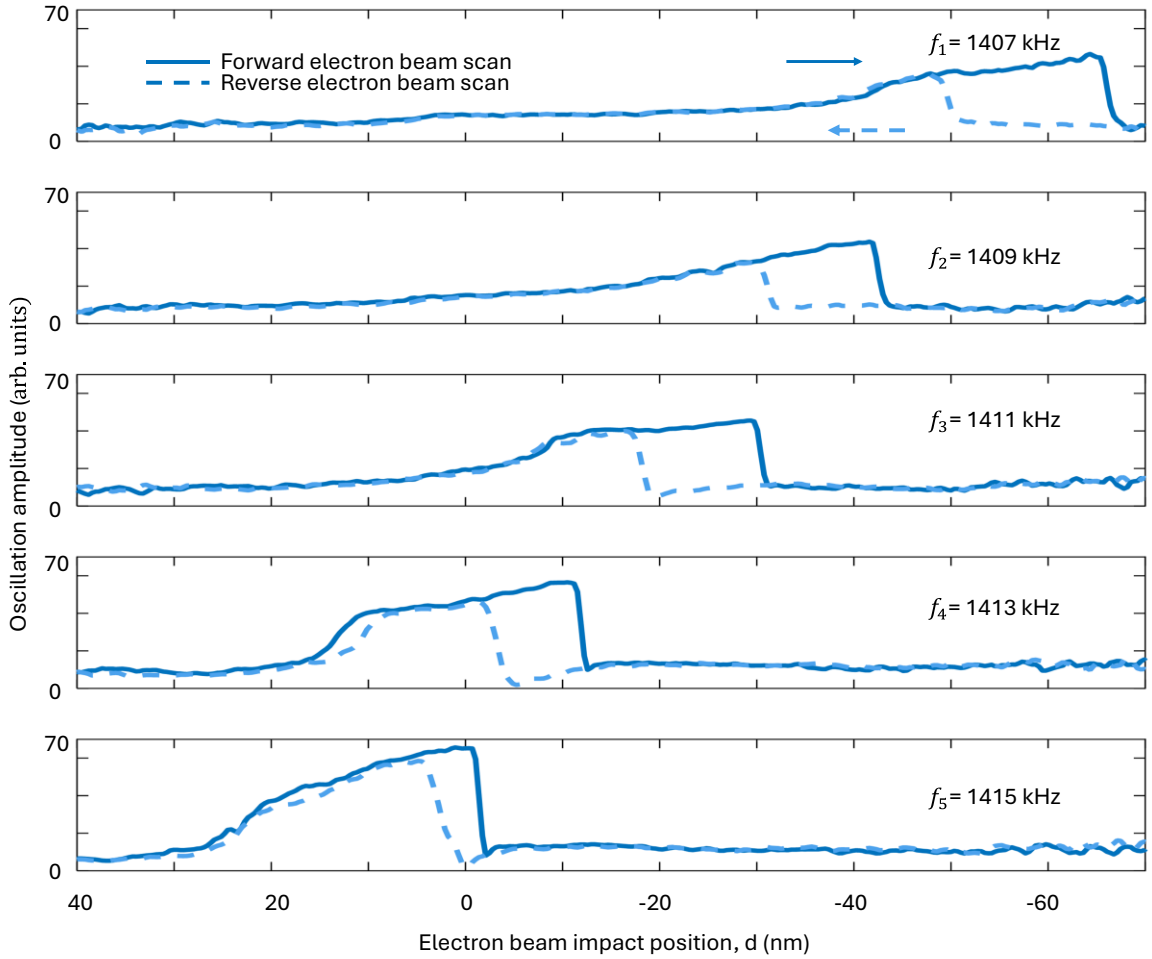

Figure 5.6: ***Switching between bistable states using an electron beam****. Nanowire oscillation amplitude as a function of decreasing (solid) and increasing (dashed) distance between electron beam and nanowire for selected driving frequencies. The nanowire edge is located at* d = 0*. A hysteresis loop can be seen, were, for the same electron beam position, the nanowire can oscillate at very different amplitudes, depending on the history of previous electron beam positions.*

The results are interpreted as follows: As illustrated by Figure 5.4 and discussed above, the nanowire's mechanical resonance frequency depends on the distance between electron beam and nanowire, as any electrons impacting on the nanowire will raise its temperature, resulting in thermal expansion that lowers its tension and thus also its natural frequency. Therefore, as the electron beam approaches (moves away from) the nanowire, heating from more (cooling from fewer) electrons impacting on the nanowire shifts its mechanical resonance to lower (higher) frequencies. In Figure 5.6, as the resonance is red-shifted (blue-shifted) past the fixed driving frequency, the oscillation amplitude follows the upper (lower) branch of the hysteresis loop.

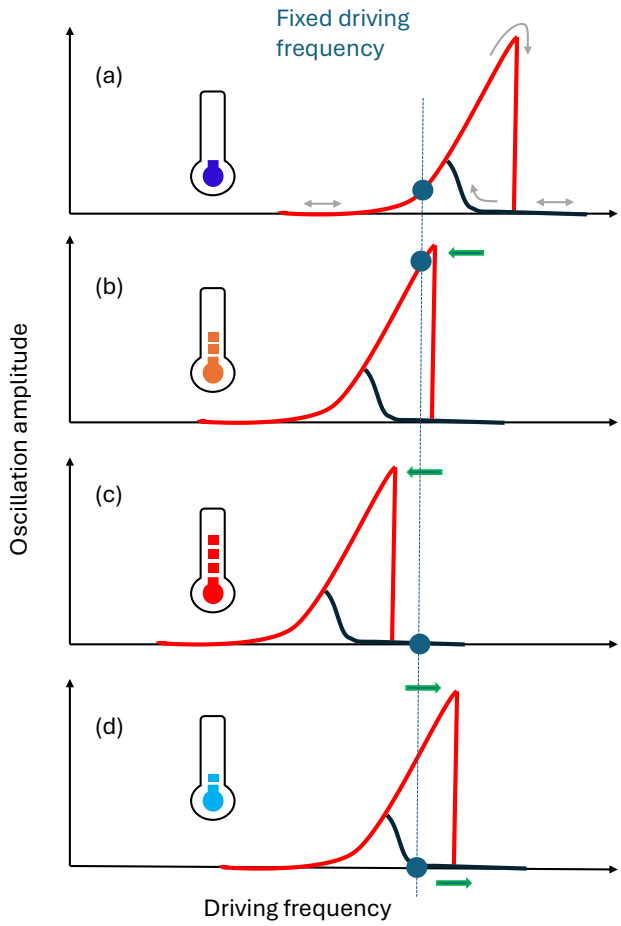

Figure 5.7: ***Mechanism of electron beam control of nanomechanical bistability****. The nanowire is driven externally by sinusoidal vibration to a highly nonlinear regime in which hysteresis of its oscillation amplitude can be observed at resonance. (a) The external driving frequency is set (blue dot) below the mechanical resonance while a distant electron beam provides little heating (thermometer). (b) By moving the electron beam closer to the nanowire, more electrons impact on and deposit energy in the nanowire, raising its temperature. Thermal expansion reduces the stress in the nanowire and the resonance shifts (green arrow) towards lower frequencies. The nanowire's oscillation amplitude follows the upper branch of the hysteresis loop. (c) With further electron-beam-induced temperature increase, the hysteresis cliff shifts beyond the fixed driving frequency: the nanowire switches to low amplitude oscillation. (d) As the electron beam moves away from the resonator, less electron beam power is deposited in the nanowire, allowing it to cool and the resonance shifts towards higher frequencies. The nanowire oscillation amplitude follows the lower branch of the hysteresis loop, returning to situation (a).*

Figure 5.7 illustrates this step-by-step, starting with the electron beam far from the nanowire that is resonant above the fixed driving frequency (low temperature, Figure 5.7a). As the electron beam approaches the nanowire (rising temperature), the resonance red-shifts leading to resonant driving of the nanowire with the oscillation amplitude following the upper branch of the hysteresis loop that is characterized by large nanowire oscillations (Figure 5.7b). As the electron beam approaches the nanowire even more (highest temperatures) the resonance red-shifts past the

driving frequency and the oscillation amplitudes drops to its low non-resonant level (Figure 5.7c). When the electron beam moves away from the nanowire (falling temperature), the resonance blue-shifts and the nanowire's oscillation amplitude follows the lower branch of the hysteresis loop (Figure 5.7d), until it the resonance frequency is above the fixed driving frequency (Figure 5.7a).

This model also explains how the fixed driving frequency controls the electron beam position at which the bistability can be observed. The bistable states can be observed when the driving frequency matches the nanonwire's resonance frequency. The lower the driving frequency, the more electron-beam-induced red-shift of the nanowire's natural frequency is required to achieve this (i.e. to go from Figure 5.7a to Figure 5.7b), and a bigger red-shift occurs when the electron beam is positioned closer to the nanowire. Therefore, at the lowest driving frequency the bistability is observed when the electron beam is closest to the nanowire or indeed positioned on the nanowire (Figure 5.6). As electron-beam-induced heating will be most sensitive to the electron beam position around the nanowire's edge, it may be expected that the nanowire's temperature and resonance frequency will most strongly depend on the electron beam position around d = 0. It follows that the hysteresis loop as a function of electron beam position should be particularly narrow near the nanowire edge and indeed, this is what is observed when driving the nanowire at 1415 kHz.

Being dependent on the power carried by the electron beam, it can be expected that the temperature increase ΔT can also be controlled by the electron beam current and acceleration voltage. Indeed, a similar red-shift of the bistable resonance can be observed when increasing the beam current (Figure 5.8), which can be explained by similar analytical arguments to those presented above, but is complicated by the effect of beam current and acceleration voltage on electron beam spot size. A wider nanowire had to be used since the narrow nanowire used throughout this chapter was experiencing large drift as the beam current was increased.

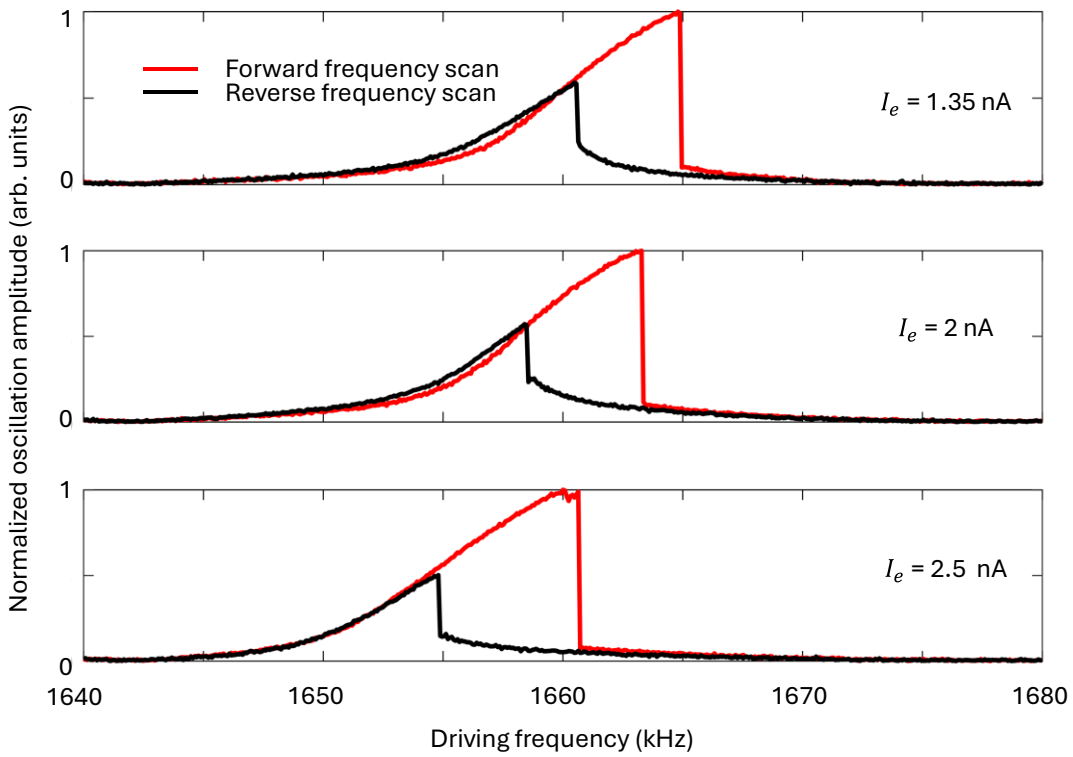

Figure 5.8: ***Effect of the electron beam currant on the nanowire's bistable resonance***. *Nanowire oscillation amplitude as a function of increasing and decreasing driving frequency for a fixed driving voltage (1.5* V_{pp}*) and different currants* I_e *of the electron beam positioned at a distance* d = 100 nm *from the edge of a different nanowire with width W* = 570 nm *and otherwise the same dimensions as in earlier figures of this chapter. The data for each currant is normalized to its own maximum.*

5.5 Summary

In conclusion, the results demonstrate how the bistable oscillation of a nonlinear nanomechanical resonator – a nanowire – can be controlled, switched and read by an electron beam. Electron-beam-induced temperature change is used to control the bistable states arising from the mechanical nonlinearity of the nanowire. Based on the incident electron beam position and the frequency of driven nanowire oscillation, the nanowire can be switched between its bistable states. These results illustrate how an electron microscope provides a versatile platform not just for characterization of nanomechanical structures, but also for their active control.

Chapter 6 Conclusion

6.1 Summary

This thesis is devoted to a series of experimental investigations aimed at detecting, visualising, and controlling driven nanomechanical dynamic responses using electron beam interaction. Fast electronics were utilized instead of the ultrafast pump-probe techniques routinely employed in electron and optical tools to achieve high temporal resolution. The thesis demonstrated nanomotion metrology and imaging using cathodoluminescence, that offers nanometer displacement sensitivity and spatial resolution combined with MHz bandwidth (Chapter 3). Complementing time-resolved cathodoluminescence techniques[115, 119, 120, 199], which rely on electron pulses and photon correlation methods, this approach offers a valuable extension for CL-based nanomotion detection and imaging. In contrast to secondary-electron-based nanomotion detection[5], detection of photons provides potential access to additional information through detection of the propagation direction, polarization and spectrum of the emitted light.

This technique is suitable for the characterisation of NEMS and MEMS devices, particularly in regimes where conventional optical interferometry is limited by diffraction. The ability to co-localize readout of motion with electron microscopy imaging enables direct mapping of vibrational modes and resonance behaviour, implying that CL-based detection could be used as a calibration and diagnostic tool for high-frequency nanomechanical systems. Beyond simple device characterization, the simultaneous interrogation of structure and mechanical response offered by the technique may also be used to study device degradation and failure, e.g. due to exposure to extreme environments or conditions, such as radiation-rich environments, large-amplitude oscillation or endurance testing[200, 201]. With the realization of on-chip electron emitters and field emitter arrays[202-205] which could realise focused electron beams, in pulsed or continuous wave from few 100s of eV to few 10s of keV and development of vacuum packaging techniques[206], the integration of CL-active nanostructures with on-chip mechanical resonators raises the possibility of localized, chip-scale sensors with CL readout. In order to establish these techniques as a robust metrological tool, however, several, challenges must be addressed, including quantitative calibration of displacement sensitivity, careful assessment of the electron-beam induced perturbations, optimization of photon collection efficiency, and evaluation of long-term stability and any damage/degradation arising from sustained electron beam exposure. Addressing these considerations will be essential for translating CL-based

nanomechanical motion detection from laboratory-scale demonstration to a broadly applicable tool in nanoscale science and engineering.

Chapter 4 and Chapter 5 present experimental evidence demonstrating how electron-beam-induced charging and heating, respectively, influence and control nanomechanical resonances. The dependence of the mechanical resonance on the velocity (acceleration voltage), beam current and position of the electron beam opens up possibilities for detecting charged particles in vacuum. In principle, such a detection scheme could be relevant for applications in particle accelerators, where non-contact, localized sensing of charged particle flux and energy is of interest[207, 208]. With the emerging research interest in reconfigurable metamaterials and photonic metamaterial continuous time-crystals[27, 68], the charging and heating-based resonance shifts offer a mechanism for electron-driven mechanical actuation and control. The results within this thesis illustrate that an electron microscope offers a versatile platform not only for characterising nanomechanical structures but also for their active control and study of their motion.

6.2 Outlook

The future work will focus on addressing the challenges faced while performing the proof-of-concept experiments reported throughout my thesis and improving the results. To begin with, all experiments were conducted with the assistance of an SEM, which encountered several technical difficulties, including precise and automated control of beam current, acceleration voltage, astigmatism, and a stepper motor-controlled x - y sample stage with manually controlled rotation, tilt, and z-stage movement. The field emission gun is controlled separately using a separate software, and then the apertures of the SEM are manually adjusted for beam current selection. Later, the SEM software is used to adjust the focus. This process will prolong the experimental time, and the experimental conditions will be affected during this time. This is why only a single acceleration voltage (10 kV) was used throughout the thesis (except for the preliminary experiment with gold in Chapter 2). Hence, a better SEM environment will significantly improve the experimental data.

Nanomechanical motion detection and visualisation using cathodoluminescence (CL) requires precise alignment of the sample at the focal point of both the parabolic mirror and the electron beam. In practice, the parabolic mirror is mechanically adjusted to achieve this alignment; however, external mechanical disturbances frequently disrupt the stability of the mirror control system. Such disturbances may arise from seemingly minor events, including the forceful opening or closing of the laboratory door, the opening of the scanning electron microscope (SEM) sample chamber, adjustments to the photodetector, or vibrations originating from the vacuum

pump. These sources of interference often lead to a loss of focus, necessitating repeated realignment during experiments. For this reason, as described in Chapter 3, imaging was restricted to a single cantilever located at the centre of the sample. A potential solution would involve integrating a piezo-controlled stage, which would allow the focal alignment of the parabolic mirror and electron beam to be fixed while enabling sample scanning at that optimised position.

Another challenge is collecting as many photons as possible from the sample onto the photodetector. In the experimental setup, the photodetector is positioned far away from the sample, and only CL light from the top surface of the sample is collected. The implementation of an improved CL setup in conjunction with a faster, more sensitive photodetector placed closer to the sample could substantially enhance the signal-to-noise ratio (SNR). Such advancements would not only improve the detection sensitivity but also extend the applicability of this approach to plasmonic materials. This, in turn, could open new avenues for nanomechanical dynamic studies employing CL in plasmonic systems.

During static cathodoluminescence imaging of the nanomechanical cantilever (Figure 3.5b), a gradual variation in the cathodoluminescence (CL) signal along the surface of the nanowire, extending over its length is observed. This spatial variation suggests that the CL intensity depends on the sample coordinate perpendicular to the imaging plane (i.e., the z direction). A systematic investigation of CL intensity as a function of out-of-plane spatial position could therefore enable simultaneous detection of both out-of-plane and in-plane motion without mechanically tilting the sample, which is commonly done in electron-based nanomechanical measurement techniques[5]. The thesis briefly discussed the potential of detecting sub-nm nanomechanical displacements using CL by increasing the integration time. Another direction to consider is improving the mechanical motion detection with the help of fast cameras and artificial intelligence. First, integrating fast cameras with CL detection would enable time-resolved imaging of scattered light. When combined with external mechanical actuation, such an approach could facilitate real-time tracking of nanomechanical motion. Incorporating artificial intelligence (AI)- based analysis could further enhance sensitivity, allowing for the detection of subtle signal fluctuations and pattern recognition in complex datasets. A similar approach was recently used in [209]. Perhaps a wavelength-selective filtering of CL emission could be employed in such a technique to isolate spectral regions of interest, thereby enabling targeted studies of specific excitations or dynamic processes.

In Chapter 4, the effect of electron beam-induced charging on nanomechanical dynamics could be further enhanced by systematically investigating the nanomechanical dynamics in relation to the acceleration voltage. Such data would provide insight into how charging phenomena might

be exploited for detecting charge particle position or velocity in charge-sensing applications. An idea is to charge a nanomechanical resonator with a known amount of charge and monitor the changes in its resonance as a charged particle passes nearby; the resulting shifts could then serve as a measure of the particle's properties, analogous to methods reported in [48]. A key limitation of the current model is that it does not account for the actual spatial distribution of charge on the material surface, nor the perturbations arising from momentum transfer to the nanowire by the electron beam[3]. Developing an improved analytical model that incorporates these factors could yield a more accurate and predictive framework for electron beam-induced charge detection using nanomechanical resonators.

In Chapter 5, the bistable response of a driven nanowire was controlled, switched and read by an electron beam. Perhaps by controlling the position of the transition point of the bistability response using electron beams, small external perturbations could snap the signal amplitude from high to low. This could enable electron beam-controlled nanomechanical bistability to underpin demonstrations of proof-of-concept sensors, signal amplifiers, volatile memory, and logic operations similar to their optical counterparts reported in [29, 61, 210, 211].

Appendix A Experimental Setup

The actual experiment setup used to conduct all the experiments presented in this thesis is shown in Figure A1a and b.

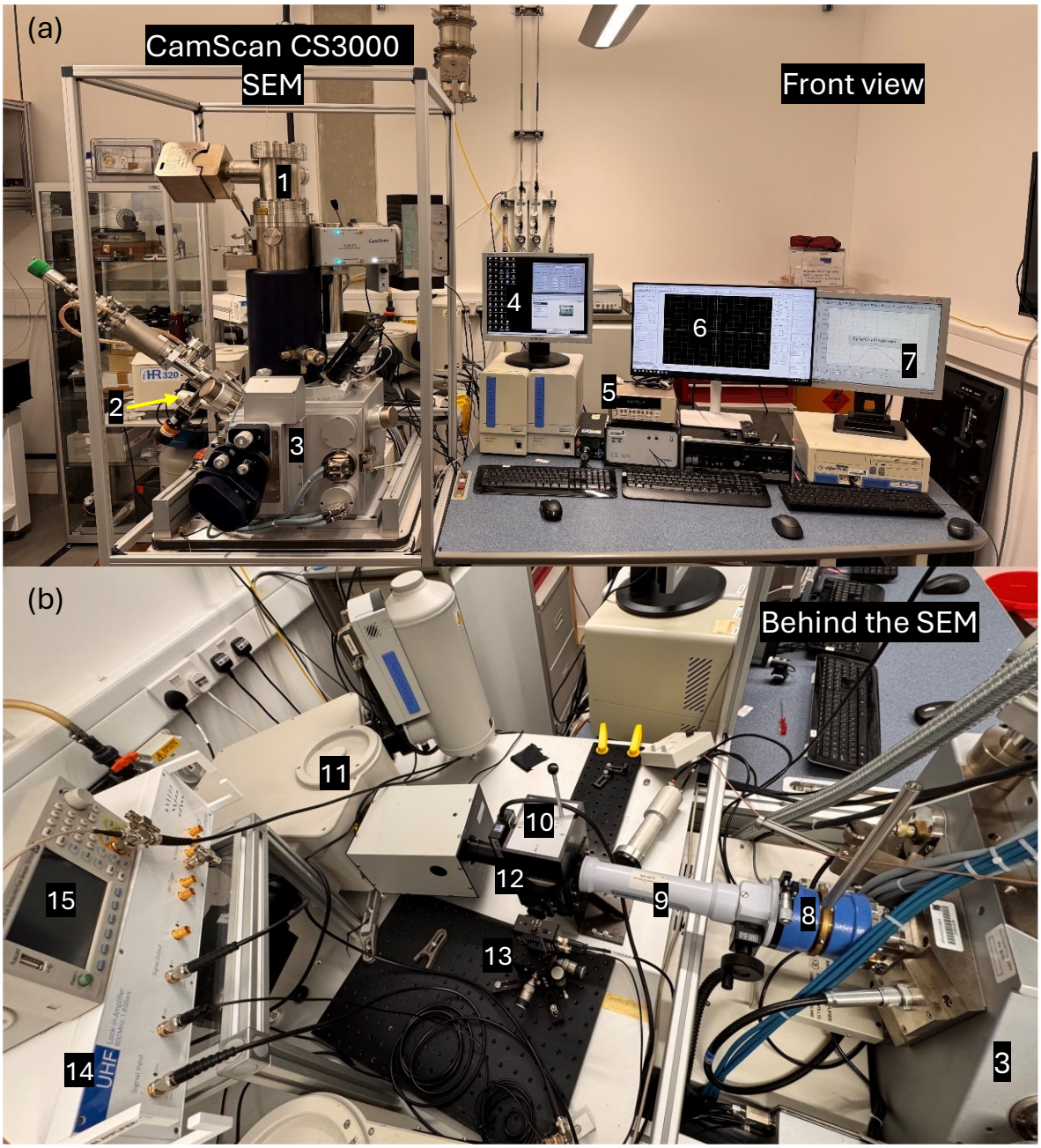

Figure A. 1: Actual experimental setup. (a) and (b) shows the front view of the scanning electron microscope and the other instruments used, kept behind the SEM. Important components are numbered. From 1 to 15, they are the field emission electron gun, Secondary electron detector, SEM sample chamber, electron gun control computer, Beam current monitoring ammeter, SEM imaging computer, Spectrometer control computer, parabolic mirror adjustment unit, beam tube, three-way switch mirror, spectrometer, lens, avalanche photodetector, Zurich Instruments UHFLI 600 MHz lock-in amplifier, and arbitrary signal-generator.

Appendix B Publications

Articles

1. **Electron-beam-controlled volatile nanomechanical bistability**
   T. Thomas, K. F. MacDonald, and E. Plum
   arXiv.org, 2509.20564 (2025)
2. **Control of nanomechanical resonances by an electron beam**
   T. Thomas, K. F. MacDonald, and E. Plum
   arXiv.org, 2509.10302 (2025)

Conference contributions

1. **Nanomotion visualization through cathodoluminescence**
   T. Thomas, E. Plum, N. I. Zheludev, and K. F. MacDonald
   CLEO/Europe-EQEC 2025, Munich, Germany, 23 - 27 June 2025
2. (poster) **Nanomotion detection using cathodoluminescence**
   T. Thomas, E. Plum, K. F. MacDonald, N. I. Zheludev
   Oxford-Southampton Exchange 2025, University of Oxford, Oxford, UK, 29 April 2025
3. (poster) **Nanomotion detection using cathodoluminescence**
   T. Thomas, E. Plum, K. F. MacDonald, N. I. Zheludev
   Research Poster Showcase, University of Southampton, Southampton, UK, 10 Dec 2024
4. (poster) **Nanomotion visualization with electrons and photons**
   T. Thomas, E. Plum, K. F. MacDonald, J. Y. Ou, N. I. Zheludev
   EBEAM2022 Summer School, Island of Porquerolles, Hyeres, France, 11 - 16 Sept, 2022

Bibliography

1. Liu, T., et al., *Ballistic dynamics of flexural thermal movements in a nanomembrane revealed with subatomic resolution*. Science Advances, 2022. **8**(33): p. eabn8007.

2. Tsioutsios, I., et al., *Real-time measurement of nanotube resonator fluctuations in an electron microscope*. Nano letters, 2017. **17**(3): p. 1748–1755.

3. Niguès, A., A. Siria, and P. Verlot, *Dynamical backaction cooling with free electrons*. Nature communications, 2015. **6**(1): p. 8104.

4. Pairis, S., et al., *Shot-noise-limited nanomechanical detection and radiation pressure backaction from an electron beam*. Physical Review Letters, 2019. **122**(8): p. 083603.

5. Liu, T., et al., *Visualization of subatomic movements in nanostructures*. Nano Letters, 2021. **21**(18): p. 7746–7752.

6. Gruber, G., et al., *Mass sensing for the advanced fabrication of nanomechanical resonators*. Nano letters, 2019. **19**(10): p. 6987–6992.

7. MacFadyen, A. and S. Woosley, *Collapsars: Gamma-ray bursts and explosions in "failed supernovae"*. The Astrophysical Journal, 1999. **524**(1): p. 262.

8. Zewail, A.H., *Femtochemistry: Atomic-scale dynamics of the chemical bond*. The Journal of Physical Chemistry A, 2000. **104**(24): p. 5660–5694.

9. Krausz, F. and M. Ivanov, *Attosecond physics*. Reviews of modern physics, 2009. **81**(1): p. 163–234.

10. Sohn, L.L., L.P. Kouwenhoven, and G. Schön, *Mesoscopic electron transport*. 2013.

11. Dantus, M., R.M. Bowman, and A.H. Zewail, *Femtosecond laser observations of molecular vibration and rotation*. Nature, 1990. **343**(6260): p. 737–739.

12. Gu, X. and R. Yang, *Phonon transport and thermal conductivity in two-dimensional materials*. Annual review of heat transfer, 2016. **19**.

13. Ishikawa, H., et al., *Direct observation of fast protein conformational switching*. Proceedings of the National Academy of Sciences, 2008. **105**(25): p. 8619–8624.

14. Marbach, S. and L. Bocquet, *Osmosis, from molecular insights to large-scale applications*. Chemical Society Reviews, 2019. **48**(11): p. 3102–3144.

15. Köhler, A., J.S. Wilson, and R.H. Friend, *Fluorescence and phosphorescence in organic materials*. Advanced Engineering Materials, 2002. **4**(7): p. 453–459.

16. Bachtold, A., J. Moser, and M. Dykman, *Mesoscopic physics of nanomechanical systems*. Reviews of Modern Physics, 2022. **94**(4): p. 045005.

17. Popov, V.N., *Carbon nanotubes: properties and application*. Materials Science and Engineering: R: Reports, 2004. **43**(3): p. 61–102.

18. Krajczewski, J., K. Kołątaj, and A. Kudelski, *Plasmonic nanoparticles in chemical analysis*. RSC advances, 2017. **7**(28): p. 17559–17576.

19. Yanagi, I., et al., *Fabrication of 3-nm-thick Si3N4 membranes for solid-state nanopores using the poly-Si sacrificial layer process*. Scientific reports, 2015. **5**(1): p. 14656.

20. Lyshevski, S.E., *MEMS and NEMS: systems, devices, and structures*. 2018: CRC press.

21. Zhu, J., et al., *Development trends and perspectives of future sensors and MEMS/NEMS*. Micromachines, 2019. **11**(1): p. 7.

22. Wei, L., et al., *The recent progress of MEMS/NEMS resonators*. Micromachines, 2021. **12**(6): p. 724.

23. Adam, T., et al., *Novel approaches in fabrication and integration of nanowire for micro/nano systems*. Critical Reviews in Analytical Chemistry, 2022. **52**(8): p. 1913–1929.

24. Koya, A.N., et al., *Plasmomechanical systems: Principles and applications*. Advanced Functional Materials, 2021. **31**(41): p. 2103706.

25. Liu, X., et al., *Progress of optomechanical micro/nano sensors: a review*. International Journal of Optomechatronics, 2021. **15**(1): p. 120–159.

26. Zheludev, N.I. and E. Plum, *Reconfigurable nanomechanical photonic metamaterials*. Nature nanotechnology, 2016. **11**(1): p. 16–22.

27. Liu, T., et al., *Photonic metamaterial analogue of a continuous time crystal*. Nature Physics, 2023. **19**(7): p. 986–991.

28. Zheng, Q., et al., *Smart actuators based on external stimulus response*. Frontiers in Chemistry, 2021. **9**: p. 650358.

29. Papas, D., et al., *Microwatt volatile optical bistability via nanomechanical nonlinearity*. Advanced Science, 2023. **10**(18): p. 2300042.

30. Kouh, T., M.S. Hanay, and K.L. Ekinci, *Nanomechanical motion transducers for miniaturized mechanical systems*. Micromachines, 2017. **8**(4): p. 108.

31. Feynman, R. *December. Plenty of Room at the Bottom*. in *APS Annual Meeting*. 1959.

32. Taniguchi, N. *On the basic concept of'nano-technology'*. in *Proc. Intl. Conf. Prod. Eng. Tokyo, Part II, 1974*. 1974. Japan Society of Precision Engineering.

33. Drexler, E., *Engines of creation: The coming era of nanotechnology*. 1987: Anchor.

34. Nathanson, H.C., et al., *The resonant gate transistor*. IEEE Transactions on Electron Devices, 1967. **14**(3): p. 117–133.

35. Angell, J.B., S.C. Terry, and P.W. Barth, *Silicon micromechanical devices*. Scientific American, 1983. **248**(4): p. 44–55.

36. Binnig, G. and H. Rohrer, *Scanning tunneling microscopy*. Surface science, 1983. **126**(1-3): p. 236–244.

37. Binnig, G., C.F. Quate, and C. Gerber, *Atomic force microscope*. Physical review letters, 1986. **56**(9): p. 930.

38. Iijima, S., *Helical microtubules of graphitic carbon*. nature, 1991. **354**(6348): p. 56–58.

39. Kroto, H.W., et al., *C60: Buckminsterfullerene*. nature, 1985. **318**(6042): p. 162–163.

40. Cleland, A.N. and M.L. Roukes, *Fabrication of high frequency nanometer scale mechanical resonators from bulk Si crystals*. Applied Physics Letters, 1996. **69**(18): p. 2653–2655.

41. Cimalla, V., et al., *Nanoelectromechanical devices for sensing applications*. Sensors and Actuators B: Chemical, 2007. **126**(1): p. 24–34.

42. Ebara, M., *Biomaterials nanoarchitectonics*. 2016: William Andrew.

43. Chaste, J., et al., *A nanomechanical mass sensor with yoctogram resolution*. Nature nanotechnology, 2012. **7**(5): p. 301–304.

44. Waggoner, P.S. and H.G. Craighead, *Micro-and nanomechanical sensors for environmental, chemical, and biological detection*. Lab on a Chip, 2007. **7**(10): p. 1238–1255.

45. Chen, Y., et al., *Nano-optomechanical resonators for sensitive pressure sensing*. ACS Applied Materials & Interfaces, 2022. **14**(34): p. 39211–39219.

46. Kanellopulos, K., et al., *Comparative analysis of nanomechanical resonators: sensitivity, response time, and practical considerations in photothermal sensing*. Microsystems & Nanoengineering, 2025. **11**(1): p. 28.

47. Ferreiro-Vila, E., et al., *Micro-Kelvin resolution at room temperature using nanomechanical thermometry*. ACS omega, 2021. **6**(36): p. 23052–23058.

48. Blick, R., et al., *Charge detection with nanomechanical resonators*. Physica E: Low-dimensional Systems and Nanostructures, 2000. **6**(1-4): p. 821–827.

49. Shi, Y., et al., *A Mobile Electric Field Sensor Device Based on Optically Levitated Nano-resonators*. Advanced Devices & Instrumentation, 2025. **6**: p. 0090.

50. Liu, W., et al., *A High-Sensitivity Resonant Magnetic Sensor Based on Graphene Nanomechanical Resonator*. Micromachines, 2022. **13**(4): p. 628.

51. Fogliano, F., et al., *Ultrasensitive nano-optomechanical force sensor operated at dilution temperatures*. Nature Communications, 2021. **12**(1): p. 4124.

52. Zheludev, N.I. and Y.S. Kivshar, *From metamaterials to metadevices*. Nature materials, 2012. **11**(11): p. 917–924.

53. Cai, W. and V. Shalaev, *Optical Metamaterials*. 2010.

54. Dorrah, A.H., et al., *Structuring total angular momentum of light along the propagation direction with polarization-controlled meta-optics*. Nature communications, 2021. **12**(1): p. 6249.

55. Ou, J.-Y., et al., *Reconfigurable photonic metamaterials*. Nano letters, 2011. **11**(5): p. 2142–2144.

56. Karvounis, A., et al., *Nano-optomechanical nonlinear dielectric metamaterials*. Applied Physics Letters, 2015. **107**(19).

57. Ou, J.-Y., et al., *Giant nonlinearity of an optically reconfigurable plasmonic metamaterial*. 2015.

58. Zhang, Q., et al., *Electrogyration in metamaterials: chirality and polarization rotatory power that depend on applied electric field*. Advanced Optical Materials, 2021. **9**(4): p. 2001826.

59. Lan, G., et al., *Non-contact optical magnetic field sensor based on metamaterial nanomechanics*. APL Photonics, 2022. **7**(3).

60. Kapfinger, S., et al., *Dynamic acousto-optic control of a strongly coupled photonic molecule*. Nature communications, 2015. **6**(1): p. 8540.

61. Nagasaki, Y., et al., *Optical bistability in shape-memory nanowire metamaterial array*. Applied Physics Letters, 2018. **113**(2).

62. Zhang, J., K.F. MacDonald, and N.I. Zheludev, *Nonlinear dielectric optomechanical metamaterials*. Light: Science & Applications, 2013. **2**(8): p. e96–e96.

63. Meng, C., et al., *Full-range birefringence control with piezoelectric MEMS-based metasurfaces*. Nature communications, 2022. **13**(1): p. 2071.

64. Han, Z., et al., *MEMS cantilever–controlled plasmonic colors for sustainable optical displays*. Science advances, 2022. **8**(16): p. eabn0889.

65. Afridi, A., et al., *Ultrathin tunable optomechanical metalens*. Nano Letters, 2023. **23**(7): p. 2496–2501.

66. Ee, H.-S. and R. Agarwal, *Tunable metasurface and flat optical zoom lens on a stretchable substrate*. Nano letters, 2016. **16**(4): p. 2818–2823.

67. Sukhov, S., et al., *Actio et reactio in optical binding*. Optics express, 2015. **23**(1): p. 247–252.

68. Liu, T., et al., *Time-translation symmetry, ergodicity, and entropy dynamics in a time crystal driven by optical interaction forces*. Newton, 2025.

69. Ou, J.-Y., et al., *An electromechanically reconfigurable plasmonic metamaterial operating in the near-infrared*. Nature nanotechnology, 2013. **8**(4): p. 252–255.

70. Valente, J., et al., *A magneto-electro-optical effect in a plasmonic nanowire material*. Nature communications, 2015. **6**(1): p. 7021.

71. Barg, A., et al., *Measuring and imaging nanomechanical motion with laser light*. Applied Physics B, 2017. **123**(1): p. 8.

72. Zhu, J., et al., *Achieving 1.2 fm/Hz1/2 displacement sensitivity with laser interferometry in two-dimensional nanomechanical resonators: pathways towards quantum-noise-limited measurement at room temperature*. Chinese Physics Letters, 2023. **40**(3): p. 038102.

73. Rothberg, S.J., et al., *An international review of laser Doppler vibrometry: Making light work of vibration measurement*. Optics and Lasers in Engineering, 2017. **99**: p. 11–22.

74. Ahn, P., et al., *Dynamic near-field optical interaction between oscillating nanomechanical structures*. Scientific reports, 2015. **5**(1): p. 10058.

75. Truitt, P.A., et al., *Efficient and sensitive capacitive readout of nanomechanical resonator arrays*. Nano letters, 2007. **7**(1): p. 120–126.

76. Toan, N.V., et al., *Design and fabrication of capacitive silicon nanomechanical resonators with selective vibration of a high-order mode*. Micromachines, 2017. **8**(10): p. 312.

77. Zewail, A.H., *Four-dimensional electron microscopy*. science, 2010. **328**(5975): p. 187–193.

78. Flannigan, D.J., et al., *Nanomechanical motions of cantilevers: Direct imaging in real space and time with 4D electron microscopy*. Nano letters, 2009. **9**(2): p. 875–881.

79. Liu, T., et al., *Detection of sub-atomic movement in nanostructures*. Nanoscale Advances, 2021. **3**(8): p. 2213–2216.

80. Molina, J., et al., *Optical transduction for vertical nanowire resonators*. Nano letters, 2020. **20**(4): p. 2359–2369.

81. Shan, S., et al., *A Comprehensive Review of Optical Metrology and Perception Technologies*. Sensors, 2025. **25**(22): p. 6811.

82. Chien, M.-H., et al., *Single-molecule optical absorption imaging by nanomechanical photothermal sensing*. Proceedings of the National Academy of Sciences, 2018. **115**(44): p. 11150–11155.

83. Hauer, B., et al., *A general procedure for thermomechanical calibration of nano/micro-mechanical resonators*. Annals of Physics, 2013. **339**: p. 181–207.

84. Buks, E. and M. Roukes, *Stiction, adhesion energy, and the Casimir effect in micromechanical systems*. Physical Review B, 2001. **63**(3): p. 033402.

85. Chardin, C., et al., *Hyperspectral Electromechanical Imaging at the Nanoscale: Dynamical Backaction, Dissipation, and Quantum Fluctuations*. Nano Letters, 2025. **25**(12): p. 4774–4780.

86. Vincent, P., et al., *Driving self-sustained vibrations of nanowires with a constant electron beam*. Physical Review B—Condensed Matter and Materials Physics, 2007. **76**(8): p. 085435.

87. Van Thourhout, D. and J. Roels, *Optomechanical device actuation through the optical gradient force*. Nature Photonics, 2010. **4**(4): p. 211–217.

88. Feng, P.X.-L., D.J. Young, and C.A. Zorman, *MEMS/NEMS devices and applications*. Springer handbook of nanotechnology, 2017: p. 395–429.

89. Schmid, S., L.G. Villanueva, and M.L. Roukes, *Fundamentals of nanomechanical resonators*. Vol. 49. 2016: Springer.

90. Bao, M., *Analysis and design principles of MEMS devices*. 2005: Elsevier.

91. Cleland, A.N., *Foundations of nanomechanics: from solid-state theory to device applications*. 2013: Springer Science & Business Media.

92. Lifshitz, R. and M.L. Roukes, *Thermoelastic damping in micro-and nanomechanical systems*. Physical review B, 2000. **61**(8): p. 5600.

93. Zener, C., *Internal friction in solids. I. Theory of internal friction in reeds*. Physical review, 1937. **52**(3): p. 230.

94. Bhiladvala, R.B. and Z.J. Wang, *Effect of fluids on the Q factor and resonance frequency of oscillating micrometer and nanometer scale beams*. Physical review E, 2004. **69**(3): p. 036307.

95. Franosch, T., et al., *Resonances arising from hydrodynamic memory in Brownian motion*. Nature, 2011. **478**(7367): p. 85–88.

96. Nørrelykke, S.F. and H. Flyvbjerg, *Harmonic oscillator in heat bath: Exact simulation of time-lapse-recorded data and exact analytical benchmark statistics*. Physical Review E—Statistical, Nonlinear, and Soft Matter Physics, 2011. **83**(4): p. 041103.

97. French, A.P., *Vibrations and waves*. 2017: CRC press.

98. Kim, J.E., *On the equivalent mass-spring parameters and assumed mode of a cantilevered beam with a tip mass*. Journal of Mechanical Science and Technology, 2017. **31**(3): p. 1073–1078.

99. Li, J., K.F. MacDonald, and N.I. Zheludev, *Optical Control of Nanomechanical Brownian Motion Eigenfrequencies in Metamaterials*. Nano Letters, 2022. **22**(11): p. 4301–4306.

100. Abbe, *The relation of aperture and power in the microscope (continued)*. Journal of the Royal Microscopical Society, 1882. **2**(4): p. 460–473.

101. Coenen, T., *Angle-resolved cathodoluminescence nanoscopy*. 2014: Universiteit van Amsterdam [Host].

102. Michler, G.H., *Compact introduction to electron microscopy*. 2023: Springer.

103. Watt, I.M., *The principles and practice of electron microscopy*. 1997: Cambridge University Press.

104. Goldstein, J.I., et al., *Scanning electron microscopy and X-ray microanalysis*. 2017: springer.

105. Dang, Z., Y. Chen, and Z. Fang, *Cathodoluminescence nanoscopy: state of the art and beyond*. ACS nano, 2023. **17**(24): p. 24431–24448.

106. Osorio, C.I., et al., *Angle-resolved cathodoluminescence imaging polarimetry*. ACS Photonics, 2016. **3**(1): p. 147–154.

107. Matsukata, T., F.J. Garcia de Abajo, and T. Sannomiya, *Chiral light emission from a sphere revealed by nanoscale relative-phase mapping*. ACS nano, 2020. **15**(2): p. 2219–2228.

108. Schilder, N.J., et al., *Phase-resolved surface plasmon scattering probed by cathodoluminescence holography*. ACS photonics, 2020. **7**(6): p. 1476–1482.

109. Kuttge, M., et al., *Local density of states, spectrum, and far-field interference of surface plasmon polaritons probed by cathodoluminescence*. Physical Review B, 2009. **79**(11): p. 113405.

110. Knight, M.W., et al., *Aluminum plasmonic nanoantennas*. Nano letters, 2012. **12**(11): p. 6000–6004.

111. Atre, A.C., et al., *Nanoscale optical tomography with cathodoluminescence spectroscopy*. Nature nanotechnology, 2015. **10**(5): p. 429–436.

112. Mauser, K.W., et al., *Employing cathodoluminescence for nanothermometry and thermal transport measurements in semiconductor nanowires*. ACS nano, 2021. **15**(7): p. 11385–11395.

113. Arbouet, A., G.M. Caruso, and F. Houdellier, *Ultrafast transmission electron microscopy: historical development, instrumentation, and applications*. Advances in imaging and electron physics, 2018. **207**: p. 1–72.

114. Gesley, M. and P. Condran, *Electron beam blanker optics*. Journal of Vacuum Science & Technology B: Microelectronics Processing and Phenomena, 1990. **8**(6): p. 1666–1672.

115. Liu, W., et al., *Exciton dynamics at a single dislocation in GaN probed by picosecond time-resolved cathodoluminescence*. Applied Physics Letters, 2016. **109**(4).

116. Spende, H., C. Margenfeld, and A. Waag, *AlGaN microfins as nonpolar UV emitters probed by time-resolved cathodoluminescence*. ACS Photonics, 2022. **9**(5): p. 1594–1604.

117. Renault, J.P., et al., *Time-resolved cathodoluminescence of DNA triggered by picosecond electron bunches*. Scientific Reports, 2020. **10**(1): p. 5071.

118. Bourrellier, R., et al., *Bright UV single photon emission at point defects in h-BN*. Nano letters, 2016. **16**(7): p. 4317–4321.

119. Kociak, M. and L.F. Zagonel, *Cathodoluminescence in the scanning transmission electron microscope*. Ultramicroscopy, 2017. **176**: p. 112–131.

120. Tizei, L. and M. Kociak, *Spatially resolved quantum nano-optics of single photons using an electron microscope*. Physical Review Letters, 2013. **110**(15): p. 153604.

121. García de Abajo, F.J., *Optical excitations in electron microscopy*. Reviews of modern physics, 2010. **82**(1): p. 209–275.

122. Brenny, B.J., A. Polman, and F.J.G. de Abajo, *Femtosecond plasmon and photon wave packets excited by a high-energy electron on a metal or dielectric surface*. Physical Review B, 2016. **94**(15): p. 155412.

123. Maciel-Escudero, C. and A. Reyes-Coronado, *Electromagnetic fields produced by a swift electron: A source of white light*. Wave Motion, 2019. **86**: p. 137–149.

124. Arabatzis, T., *Cathode rays*, in *Compendium of Quantum Physics*. 2009, Springer. p. 89–92.

125. Coenen, T. and N. Haegel, *Cathodoluminescence for the 21st century: Learning more from light*. Applied Physics Reviews, 2017. **4**(3).

126. Yacobi, B.G. and D.B. Holt, *Cathodoluminescence*, in *Cathodoluminescence Microscopy of Inorganic Solids*. 1990, Springer. p. 55–88.

127. Gucsik, A., *Cathodoluminescence and its Application in the Planetary Sciences*. Vol. 160. 2009: Springer.

128. Ozawa, L., *Cathodoluminescence and photoluminescence: theories and practical applications*. 2018: CRC Press.

129. Brenny, B.J., A. Polman, and F.J. Garcia de Abajo, *Femtosecond plasmon and photon wave packets excited by a high-energy electron on a metal or dielectric surface*. Physical Review B, 2016. **94**(15): p. 155412.

130. Polman, A., M. Kociak, and F.J. García de Abajo, *Electron-beam spectroscopy for nanophotonics*. Nature materials, 2019. **18**(11): p. 1158–1171.

131. Myroshnychenko, V., et al., *Plasmon spectroscopy and imaging of individual gold nanodecahedra: a combined optical microscopy, cathodoluminescence, and electron energy-loss spectroscopy study*. Nano letters, 2012. **12**(8): p. 4172–4180.

132. Bashevoy, M., et al., *Hyperspectral imaging of plasmonic nanostructures with nanoscale resolution*. Optics express, 2007. **15**(18): p. 11313–11320.

133. Frank, I. and I. Tamm, *Coherent visible radiation of fast electrons passing through matter*, in *Selected Papers*. 1991, Springer. p. 29–35.

134. Potylitsyn, A.P., *Transition radiation and diffraction radiation. Similarities and differences*. Nuclear Instruments and Methods in Physics Research Section B: Beam Interactions with Materials and Atoms, 1998. **145**(1-2): p. 169–179.

135. Smith, S.J. and E.M. Purcell, *Visible light from localized surface charges moving across a grating*. Physical Review, 1953. **92**(4): p. 1069.

136. Zhang, Y., et al., *Edge scattering of surface plasmons excited by scanning tunneling microscopy*. Optics express, 2013. **21**(12): p. 13938–13948.

137. Kuttge, M., et al., *Loss mechanisms of surface plasmon polaritons on gold probed by cathodoluminescence imaging spectroscopy*. Applied Physics Letters, 2008. **93**(11).

138. Amendola, V., et al., *Surface plasmon resonance in gold nanoparticles: a review*. Journal of physics: Condensed matter, 2017. **29**(20): p. 203002.

139. Mahfoud, Z., et al., *Cathodoluminescence in a scanning transmission electron microscope: A nanometer-scale counterpart of photoluminescence for the study of ii–vi quantum dots*. The Journal of Physical Chemistry Letters, 2013. **4**(23): p. 4090–4094.

140. Brenny, B., T. Coenen, and A. Polman, *Quantifying coherent and incoherent cathodoluminescence in semiconductors and metals*. Journal of Applied Physics, 2014. **115**(24).

141. Hohenester, U. and A. Trügler, *MNPBEM–A Matlab toolbox for the simulation of plasmonic nanoparticles*. Computer Physics Communications, 2012. **183**(2): p. 370–381.

142. Kolwas, K. and A. Derkachova, *Impact of the interband transitions in gold and silver on the dynamics of propagating and localized surface plasmons*. Nanomaterials, 2020. **10**(7): p. 1411.

143. Johnson, P.B. and R.-W. Christy, *Optical constants of the noble metals*. Physical review B, 1972. **6**(12): p. 4370.

144. Li, G., et al., *Holographic free-electron light source*. Nature communications, 2016. **7**(1): p. 1–6.

145. Sun, H., et al., *Elastic strain engineered nanomechanical GaN resonators with thermoelastic dissipation dilution up to 600 K*. Journal of Applied Physics, 2022. **131**(5).

146. Bayram, F., et al., *Mechanical memory operations in piezotransistive GaN microcantilevers using au nanoparticle-enhanced photoacoustic excitation*. Microsystems & nanoengineering, 2022. **8**(1): p. 8.

147. Castelletto, S. and A. Boretti, *Gallium nitride nanomaterials and color centers for quantum technologies*. ACS Applied Nano Materials, 2024. **7**(6): p. 5862–5877.

148. Zheng, Y., et al., *Integrated gallium nitride nonlinear photonics*. Laser & Photonics Reviews, 2022. **16**(1): p. 2100071.

149. Steib, F., et al., *Defect generation by nitrogen during pulsed sputter deposition of GaN*. Journal of Applied Physics, 2018. **124**(17).

150. Motomura, T., et al., *Influence of nitrogen gas flow ratio on gallium nitride film growth using high-density convergent plasma sputtering device at room temperature*. Journal of Vacuum Science & Technology A, 2021. **39**(1).

151. Maruyama, T. and H. Miyake, *Gallium nitride thin films deposited by radio-frequency magnetron sputtering*. Journal of Vacuum Science & Technology A, 2006. **24**(4): p. 1096–1099.

152. Buks, E. and M.L. Roukes, *Metastability and the Casimir effect in micromechanical systems*. Europhysics Letters, 2001. **54**(2): p. 220.

153. Feist, A., et al., *Ultrafast transmission electron microscopy using a laser-driven field emitter: Femtosecond resolution with a high coherence electron beam*. Ultramicroscopy, 2017. **176**: p. 63–73.

154. Zaitsev, S., O. Shtempluck, and E. Buks, *Effects of electron beam induced carbon deposition on the mechanical properties of a micromechanical oscillator*. Sensors and Actuators A: Physical, 2012. **179**: p. 237–241.

155. Hugenschmidt, M., et al., *Electron-beam-induced carbon contamination in STEM-in-SEM: Quantification and mitigation*. Microscopy and Microanalysis, 2023. **29**(1): p. 219–234.

156. Egerton, R.F., P. Li, and M. Malac, *Radiation damage in the TEM and SEM*. Micron, 2004. **35**(6): p. 399–409.

157. Ichinokawa, T., et al., *Charging effect of specimen in scanning electron microscopy*. Japanese Journal of Applied Physics, 1974. **13**(8): p. 1272.

158. Ding, Z., et al., *Charging effect induced by electron beam irradiation: a review*. Science and Technology of Advanced Materials, 2021. **22**(1): p. 932–971.

159. Dove, D., *Image contrasts in thin carbon films observed by shadow electron microscopy*. Journal of Applied Physics, 1964. **35**(5): p. 1652–1653.

160. Curtis, G. and R. Ferrier, *The electric charging of electron-microscope specimens*. Journal of Physics D: Applied Physics, 1969. **2**(7): p. 1035.

161. Brink, J., et al., *Evaluation of charging on macromolecules in electron cryomicroscopy*. Ultramicroscopy, 1998. **72**(1-2): p. 41–52.

162. Bunker, M.J., et al., *Direct observation of single particle electrostatic charging by atomic force microscopy*. Pharmaceutical research, 2007. **24**(6): p. 1165–1169.

163. Lin, S.-M., *Analytical solutions of the frequency shifts of several modes in dynamic force microscopy subjected to AC electrostatic force*. IEEE transactions on nanotechnology, 2007. **6**(4): p. 404–412.

164. Kocić, N., et al., *Periodic charging of individual molecules coupled to the motion of an atomic force microscopy tip*. Nano letters, 2015. **15**(7): p. 4406–4411.

165. Chen, D., et al., *An electrostatic charge sensor based on micro resonator with sensing scheme of effective stiffness perturbation*. Journal of Micromechanics and Microengineering, 2017. **27**(6): p. 065002.

166. Brueckner, K., et al., *Micro-and nano-electromechanical resonators based on SiC and group III-nitrides for sensor applications*. physica status solidi (a), 2011. **208**(2): p. 357–376.

167. Chang, J., et al., *Synthesis and bidirectional frequency tuning of cantilever-shape nano resonators using a focused ion beam*. ACS Applied Materials & Interfaces, 2013. **5**(19): p. 9684–9690.

168. Wang, X., et al., *Single-electron detection utilizing coupled nonlinear microresonators*. Microsystems & Nanoengineering, 2020. **6**(1): p. 78.

169. Kwon, J., et al., *Frequency tuning of nanowire resonator using electrostatic spring effect*. IEEE transactions on magnetics, 2009. **45**(5): p. 2332–2335.

170. Yasuda, M., et al., *Oscillation control of carbon nanotube mechanical resonator by electrostatic interaction induced retardation*. Scientific reports, 2016. **6**(1): p. 22600.

171. Kim, K.H., et al., *Charging effects on SEM/SIM contrast of metal/insulator system in various metallic coating conditions*. Materials transactions, 2010. **51**(6): p. 1080–1083.

172. Imashuku, S., S. Sakatoku, and J. Kawai, *Effect of electrical charging on scanning electron microscopy-energy dispersive X-ray spectroscopy analysis of insulating materials*. Spectrochimica Acta Part B: Atomic Spectroscopy, 2013. **86**: p. 94–98.

173. Zhang, Y., et al., *Charging of vitreous samples in cryogenic electron microscopy mitigated by graphene*. ACS nano, 2023. **17**(16): p. 15836–15846.

174. Postek, M.T. and A.E. Vladár. *Does your SEM really tell the truth? How would you know? Part 4: charging and its mitigation*. in *Scanning Microscopies 2015*. 2015. SPIE.

175. Griffiths, D.J., *Introduction to electrodynamics*. 2023: Cambridge University Press.

176. Kaajakari, V., *Practical mems*. (No Title), 2009.

177. Jackson, J.D. and R.F. Fox, *Classical electrodynamics*. 1999, American Association of Physics Teachers.

178. Tadokoro, Y., H. Tanaka, and M. Dykman, *Driven nonlinear nanomechanical resonators as digital signal detectors*. Scientific Reports, 2018. **8**(1): p. 11284.

179. Harne, R. and K. Wang, *A bifurcation-based coupled linear-bistable system for microscale mass sensing*. Journal of Sound and Vibration, 2014. **333**(8): p. 2241–2252.

180. Charlot, B., et al., *Bistable nanowire for micromechanical memory*. Journal of Micromechanics and Microengineering, 2008. **18**(4): p. 045005.

181. Kovacic, I. and M.J. Brennan, *The Duffing equation: nonlinear oscillators and their behaviour*. 2011: John Wiley & Sons.

182. Rechnitz, S., et al., *DC signature of snap-through bistability in carbon nanotube mechanical resonators*. Nano letters, 2022. **22**(18): p. 7304–7310.

183. Ghosh, A., et al., *Dynamical configurations and bistability of helical nanostructures under external torque*. Physical Review E—Statistical, Nonlinear, and Soft Matter Physics, 2012. **86**(3): p. 031401.

184. Badzey, R.L. and P. Mohanty, *Coherent signal amplification in bistable nanomechanical oscillators by stochastic resonance*. Nature, 2005. **437**(7061): p. 995–998.

185. Gibbs, H., *Optical bistability: controlling light with light*. 2012: Elsevier.

186. Barakat, J.M.H., et al., *Advances in optical bistability: Theory, devices, and emerging applications*. Results in Engineering, 2025: p. 105540.

187. Nikitin, A.A., et al., *Optical bistable SOI micro-ring resonators for memory applications*. Optics Communications, 2022. **511**: p. 127929.

188. Soljacic, M., et al. *All-optical switching using optical bistability in nonlinear photonic crystals*. in *Photonic crystal materials and devices*. 2003. SPIE.

189. Protsenko, I.E. and A.V. Uskov, *Single-photon optical bistability in a small nonlinear cavity*. Physical Review A, 2023. **108**(2): p. 023724.

190. Zheludev, N.I., *Time crystals for photonics and timetronics*. Nature Photonics, 2024. **18**(11): p. 1123–1125.

191. Papas, D., et al., *Optomechanical metamaterial nanobolometer*. APL Photonics, 2021. **6**(12).

192. Xu, B., et al., *Nanomechanical resonators: toward atomic scale*. Acs Nano, 2022. **16**(10): p. 15545–15585.

193. Lifshitz, R. and M.C. Cross, *Nonlinear dynamics of nanomechanical and micromechanical resonators*. Reviews of nonlinear dynamics and complexity, 2008. **1**(1).

194. Almog, R., et al., *High intermodulation gain in a micromechanical duffing resonator*. Applied physics letters, 2006. **88**(21).

195. Landau, L.D., E.M. Lifshit͡s, and E.M. Lifshit͡s, *Mechanics*. Vol. 1. 1960: CUP Archive.

196. Bokaian, A., *Natural frequencies of beams under tensile axial loads*. Journal of sound and vibration, 1990. **142**(3): p. 481–498.

197. Leszczynski, M., et al., *Thermal expansion of gallium nitride*. Journal of applied physics, 1994. **76**(8): p. 4909–4911.

198. Qin, H., et al., *Mechanical, thermodynamic and electronic properties of wurtzite and zinc-blende GaN crystals*. Materials, 2017. **10**(12): p. 1419.

199. Roques-Carmes, C., et al., *Free-electron–light interactions in nanophotonics*. Applied Physics Reviews, 2023. **10**(1).

200. Feldbach, E., et al., *Cathodoluminescence as a tool for monitoring radiation damage recovery in corundum*. Journal of Luminescence, 2024. **269**: p. 120490.

201. Pietryga, J.M., et al. *Probing the gamma-scintillation process in semiconductor nanomaterials using ultrafast transient cathodoluminescence*. in *Chemical, Biological, Radiological, Nuclear, and Explosives (CBRNE) Sensing XIV*. 2013. SPIE.

202. Guerrera, S. and A.I. Akinwande, *Nanofabrication of arrays of silicon field emitters with vertical silicon nanowire current limiters and self-aligned gates*. Nanotechnology, 2016. **27**(29): p. 295302.

203. Liu, F., et al., *Integrated Cherenkov radiation emitter eliminating the electron velocity threshold*. Nature Photonics, 2017. **11**(5): p. 289–292.

204. Temple, D., *Recent progress in field emitter array development for high performance applications*. Materials Science and Engineering: R: Reports, 1999. **24**(5): p. 185–239.

205. Spindt, C., et al., *Field-emitter arrays for vacuum microelectronics*. IEEE Transactions on Electron Devices, 2002. **38**(10): p. 2355–2363.

206. Lemoine, D., et al. *MEMS wafer-level vacuum packaging with transverse interconnects for CMOS integration*. in *2008 IEEE Custom Integrated Circuits Conference*. 2008. IEEE.

207. Perera, A., et al. *Towards ultra-high gradient particle acceleration in carbon nanotubes*. in *Journal of Physics: Conference Series*. 2020. IOP Publishing.

208. Lei, B., et al., *100 s $\text {TeV}/\text {m} $-level particle accelerators driven by high-density electron beams in micro structured carbon nanotube forest channel*. New Journal of Physics, 2025. **27**(8): p. 084301.

209. Liu, T., et al., *Picophotonic localization metrology beyond thermal fluctuations*. Nature Materials, 2023. **22**(7): p. 844–847.

210. Almog, R., et al., *Signal amplification in a nanomechanical Duffing resonator via stochastic resonance*. Applied physics letters, 2007. **90**(1).

211. Guerra, D.N., et al., *A noise-assisted reprogrammable nanomechanical logic gate*. Nano letters, 2010. **10**(4): p. 1168–1171.